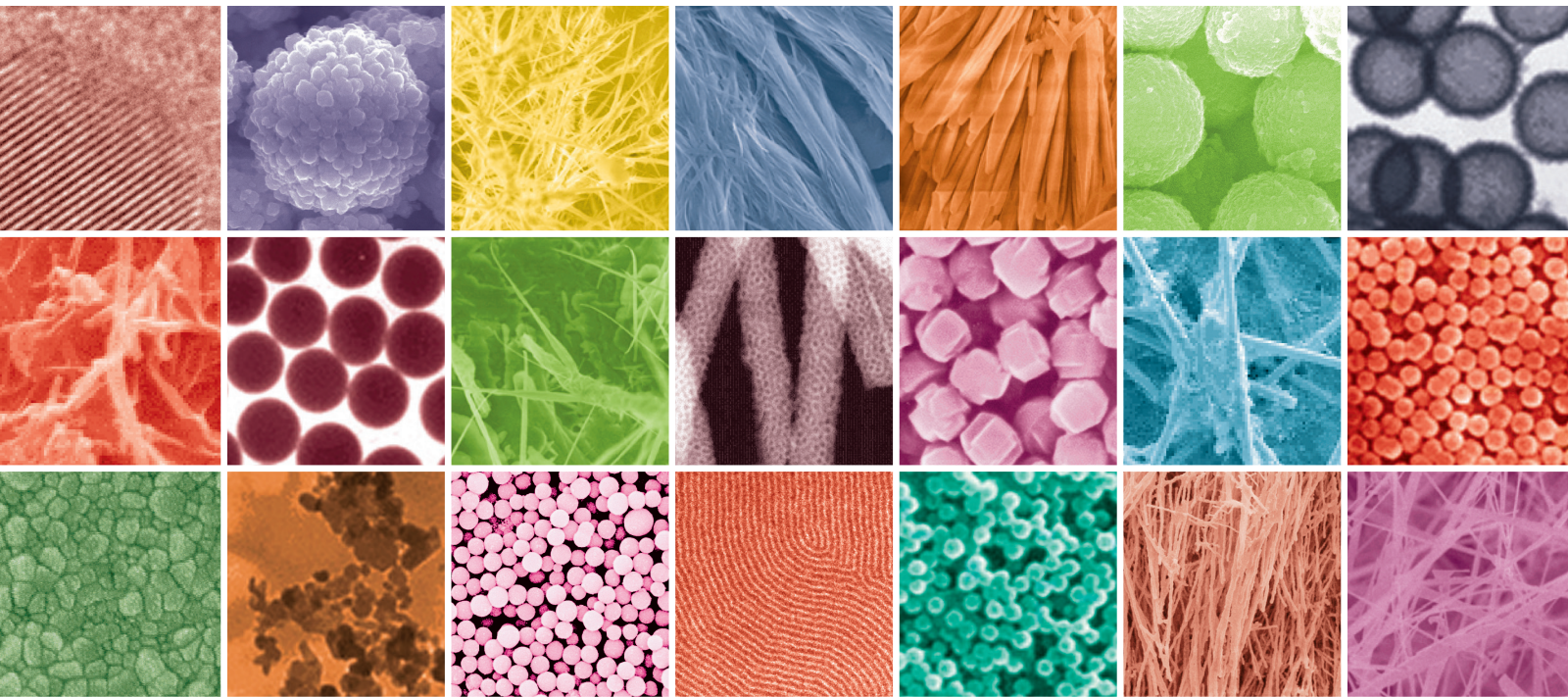


# Optical Properties of Nanoparticles and Nanocomposites

Guest Editors: Pathik Kumbhakar, Suprakash Sinha Ray,  
and Andey L. Stepanov





---

# **Optical Properties of Nanoparticles and Nanocomposites**

# **Optical Properties of Nanoparticles and Nanocomposites**

Guest Editors: Pathik Kumbhakar, Suprakas Sinha Ray,  
and Andey L. Stepanov



---

Copyright © 2014 Hindawi Publishing Corporation. All rights reserved.

This is a special issue published in "Journal of Nanomaterials." All articles are open access articles distributed under the Creative Commons Attribution License, which permits unrestricted use, distribution, and reproduction in any medium, provided the original work is properly cited.

## Editorial Board

Katerina E. Aifantis, USA  
Nageh K. Allam, USA  
Margarida Amaral, Portugal  
Xuedong Bai, China  
Lavinia Balan, France  
Enrico Bergamaschi, Italy  
Theodorian Borca-Tasciuc, USA  
C. Jeffrey Brinker, USA  
Christian Brosseau, France  
Xuebo Cao, China  
Shafiq Chowdhury, USA  
Kwang-Leong Choy, UK  
Cui ChunXiang, China  
Miguel A. Correa-Duarte, Spain  
Shadi A. Dayeh, USA  
Ali Eftekhari, USA  
Claude Estourns, France  
Alan Fuchs, USA  
Lian Gao, China  
Russell E. Gorga, USA  
Hongchen Chen Gu, China  
Mustafa O. Guler, Turkey  
John Z. Guo, USA  
Smrati Gupta, Germany  
Michael Harris, USA  
Zhongkui Hong, China  
Michael Z. Hu, USA  
David Hui, USA  
Y.-K. Jeong, Republic of Korea  
Sheng-Rui Jian, Taiwan  
Wanqin Jin, China  
Rakesh K. Joshi, UK  
Zhenhui Kang, China  
Fathallah Karimzadeh, Iran  
Alireza Khataee, Iran

Do Kyung Kim, Korea  
Alan K. T. Lau, Hong Kong  
Burtrand Lee, USA  
Jun Li, Singapore  
Benxia Li, China  
Xing-Jie Liang, China  
Shijun Liao, China  
Gong-Ru Lin, Taiwan  
Tianxi Liu, China  
Jun Liu, USA  
Songwei Lu, USA  
Daniel Lu, China  
Jue Lu, USA  
Ed Ma, USA  
Gaurav Mago, USA  
Santanu K. Maiti, India  
Sanjay R. Mathur, Germany  
Vikas Mittal, UAE  
Weihai Ni, China  
Sherine Obare, USA  
Atsuto Okamoto, Japan  
Abdelwahab Omri, Canada  
Edward A. Payzant, USA  
Kui-Qing Peng, China  
Anukorn Phuruangrat, Thailand  
Mahendra Rai, India  
Suprakas Sinha Ray, South Africa  
Ugur Serincan, Turkey  
Huaiyu Shao, Japan  
Donglu Shi, USA  
Vladimir Sivakov, Germany  
Marinella Striccoli, Italy  
Bohua Sun, South Africa  
Saikat Talapatra, USA  
Nairong Tao, China

Titipun Thongtem, Thailand  
Somchai Thongtem, Thailand  
Alexander Tolmachev, Ukraine  
Valeri P. Tolstoy, Russia  
Tsung-Yen Tsai, Taiwan  
Takuya Tsuzuki, Australia  
Raquel Verdejo, Spain  
Mat U. Wahit, Malaysia  
Zhenbo Wang, China  
Ruiping Wang, Canada  
Shiren Wang, USA  
Cheng Wang, China  
Yong Wang, USA  
Jinquan Wei, China  
Ching-Ping Wong, Hong Kong  
Xingcai Wu, China  
Guodong Xia, Hong Kong  
Ping Xiao, UK  
Zhi Li Xiao, USA  
Yangchuan Xing, USA  
Shuangxi Xing, China  
Nanping Xu, China  
Doron Yadlovker, Israel  
Yingkui Yang, China  
Khaled Youssef, USA  
Kui Yu, Canada  
William W. Yu, USA  
Haibo Zeng, China  
Tianyou Zhai, China  
Bin Zhang, China  
Renyun Zhang, Sweden  
Yanbao Zhao, China  
Lianxi Zheng, Singapore  
Chunyi Zhi, Hong Kong

## Contents

**Optical Properties of Nanoparticles and Nanocomposites**, Pathik Kumbhakar, Suprakas Sinha Ray, and Andey L. Stepanov  
Volume 2014, Article ID 181365, 2 pages

**Sensing Heavy Metals Using Mesoporous-Based Optical Chemical Sensors**, Špela Korent Urek, Nina Frančič, Matejka Turel, and Aleksandra Lobnik  
Volume 2013, Article ID 501320, 13 pages

**Optical Property Characterization of Novel Graphene-X (X=Ag, Au and Cu) Nanoparticle Hybrids**, Sumit Ranjan Sahu, Mayanglambam Manolata Devi, Puspall Mukherjee, Pratik Sen, and Krishanu Biswas  
Volume 2013, Article ID 232409, 9 pages

**Green Light Emission of Zn<sub>x</sub>Cd<sub>1-x</sub>Se Nanocrystals Synthesized by One-Pot Method**, Shu-Ru Chung, Kuan-Wen Wang, and Hong-Shuo Chen  
Volume 2013, Article ID 526862, 9 pages

**Morphology and Optical Property of ZnO Nanostructures Grown by Solvothermal Method: Effect of the Solution Pretreatment**, Wenhui Zhang, Xiahui Chen, Ning Xu, Rong Xiang, Yuan Zhu, and Zikang Tang  
Volume 2013, Article ID 986157, 4 pages

**Optical Properties and *In Vitro* Biological Studies of Oligonucleotide-Modified Quantum Dots**, Valérie A. Gérard, Mark Freeley, Eric Defrancq, Anatoly V. Fedorov, and Yurii K. Gun'ko  
Volume 2013, Article ID 463951, 10 pages

**Core-Shell Structure in Doped Inorganic Nanoparticles: Approaches for Optimizing Luminescence Properties**, Dini Xie, Hongshang Peng, Shihua Huang, and Fangtian You  
Volume 2013, Article ID 891515, 10 pages

**Luminescent Properties of Y<sub>2</sub>O<sub>3</sub>:Eu<sup>3+</sup> Nanocrystals Prepared by Molten Salt Synthesis**, Lijun Luo, Fenfen Hu, Li Xiong, Xiaofan Li, Meili Zhou, and Zhengliang Wang  
Volume 2013, Article ID 952623, 4 pages

**Effect of Calcination Temperature on Structural Properties and Photocatalytic Activity of Ceria Nanoparticles Synthesized Employing Chitosan as Template**, Angela B. Sifontes, Maibelin Rosales, Franklin J. Méndez, Olycen Oviedo, and Tamara Zoltan  
Volume 2013, Article ID 265797, 9 pages

## Editorial

# Optical Properties of Nanoparticles and Nanocomposites

Pathik Kumbhakar,<sup>1</sup> Suprakas Sinha Ray,<sup>2</sup> and Andey L. Stepanov<sup>3</sup>

<sup>1</sup> Nanoscience Laboratory, Department of Physics, National Institute of Technology (NIT), Durgapur, West Bengal 713209, India

<sup>2</sup> Council for Scientific and Industrial Research, Pretoria 0001, South Africa

<sup>3</sup> Nano-Optics and Nano-Plasmonics Group, Kazan Physical-Technical Institute, Russian Academy of Sciences, Kazan 420029, Russia

Correspondence should be addressed to Pathik Kumbhakar; nitdgpkumbhakar@yahoo.com

Received 1 April 2014; Accepted 1 April 2014; Published 13 April 2014

Copyright © 2014 Pathik Kumbhakar et al. This is an open access article distributed under the Creative Commons Attribution License, which permits unrestricted use, distribution, and reproduction in any medium, provided the original work is properly cited.

Semiconductor and metallic nanomaterials and nanocomposites possess interesting linear absorption, photoluminescence emission, and nonlinear optical properties. Nanomaterials having small particle sizes exhibit enhanced optical emission as well as nonlinear optical properties due to the quantum confinement effect. Synthesis, characterization, and measurement of optical properties of nanomaterials with different anisotropic shapes have also drawn significant attention. Recently, a lot of research focuses have been given on the preparation of polymer semiconductor and other nanocomposite materials having potential applications in different optoelectronics and photonics devices.

In this special issue, research papers covering the following topics are called for publication and a total of 8 numbers of original research papers and review articles that have been accepted got publication. The topics include techniques of synthesis, characterizations, and optical properties of semiconductor nanomaterials, nanocomposites of polymer-semiconductor and graphene-metal nanoparticles, and plasmonic properties of metal nanoparticles and nanostructures.

In the paper entitled “Sensing heavy metals using mesoporous-based optical chemical sensors,” Urek et al. have reviewed the recent advances, advantages, and limitations of mesoporous silica-based optical sensors for heavy metal detection. In the paper entitled “Optical property characterization of novel graphene-X (X = Ag, Au and Cu) nanoparticle hybrids,” authors have reported their results on investigation on synthesis, nanostructural characterizations, and optical properties, including modifications of surface plasmon resonance (SPR) properties and of graphene-metal nanocomposite with the incorporation of nanoparticles in the graphene nanosheets. Chung et al. in their paper entitled “Green light

emission of  $Zn_xCd_{1-x}Se$  nanocrystals synthesized by one-pot method” have reported a facile one-pot synthesis technique for preparation of ternary nanocrystals of  $Zn_xCd_{1-x}Se$  which show tunable photoluminescence light emission in the green wavelength region having quantum yield of 45–89%. Zhang et al. reported the synthesis of ZnO nanostructures with different morphologies, such as nanopyramids, nanosheets, and nanoparticles in their paper entitled “Morphology and optical property of ZnO nanostructures grown by solvothermal method: effect of the solution pretreatment.” They have used Raman and photoluminescence spectroscopies to examine the crystallinity and optical property of the samples.

In the paper entitled “Optical properties and *in vitro* biological studies of oligonucleotide-modified quantum dots,” Gérard et al. have reported the synthesis and characterizations of a series of new oligonucleotide-modified CdTe quantum dots (QDs); also they have performed *in vitro* test. Xie et al. have reported a review on recent advances in optimizing luminescence properties of doped nanoparticles based on core-shell structure in their paper entitled “Core-shell structure in doped inorganic nanoparticles: approaches for optimizing luminescence properties.” Luo et al. in the paper entitled “Luminescent properties of  $Y_2O_3:Eu^{3+}$  nanocrystals prepared by molten salt synthesis” have reported the synthesis, structures, morphologies, and the photoluminescent properties of  $Y_2O_3:Eu^{3+}$  phosphors. They observed tuning in particle size by using different surfactants and reported red emission under the excitation of UV light of 254 nm. The treatment of water by using the heterogeneous semiconductor photocatalysts has drawn recent attention. However, Sifontes et al. in the paper entitled “Effect of calcination temperature on structural properties and photocatalytic activity of ceria nanoparticles

*synthesized employing chitosan as template*” have reported the synthesis of ceria nanoparticles and degradation of Congo red (CR) dye under the visible light irradiation.

We are very much happy to note the research progress on the techniques of synthesis, characterization, and optical properties of nanostructured materials. Also we are very much hopeful that this special issue will provide the thoughts to the beginners and will be helpful for the potential researchers to start research work in the area of development of the nanoparticles and nanocomposite materials which are required for the future optoelectronic devices.

### **Acknowledgments**

The editors would like to thank and express their appreciations to all authors for their valued contributions and to all potential reviewers for sparing their valuable time, efforts, and constructive comments for this special issue. We are thankful to the Huda Qabeel for her help.

*Pathik Kumbhakar  
Suprakas Sinha Ray  
Andey L. Stepanov*

## Review Article

# Sensing Heavy Metals Using Mesoporous-Based Optical Chemical Sensors

Špela Korent Urek,<sup>1</sup> Nina Frančič,<sup>2</sup> Matejka Turel,<sup>1</sup> and Aleksandra Lobnik<sup>2</sup>

<sup>1</sup> Institute of Environmental Protection and Sensors, Beloruska 7, 2000 Maribor, Slovenia

<sup>2</sup> University of Maribor, Faculty of Mechanical Engineering, Centre of Sensor Technology, Smetanova 17, 2000 Maribor, Slovenia

Correspondence should be addressed to Aleksandra Lobnik; [aleksandra.lobnik@um.si](mailto:aleksandra.lobnik@um.si)

Received 10 May 2013; Revised 30 July 2013; Accepted 18 September 2013

Academic Editor: Pathik Kumbhakar

Copyright © 2013 Špela Korent Urek et al. This is an open access article distributed under the Creative Commons Attribution License, which permits unrestricted use, distribution, and reproduction in any medium, provided the original work is properly cited.

Heavy metal pollution is one of the more serious environmental problems; therefore, there is a constant demand for the development of new analytical tools for its monitoring. An optical chemical sensor represents a good alternative to classical instrumental methods. The mesoporous materials used in optical chemical sensors' fabrications have properties such as high porosity, exceptional adsorption capacity, tuneable 3D shape, geometry, and morphology, which enable improved limit of detection, response time, and selectivity properties of optical sensors. In this review, we firstly present the properties of mesoporous materials, provide a brief description of sensing mechanisms, and briefly discuss the importance of continuous monitoring. Recent advances in those mesoporous silica-based optical sensors used for heavy metal detection have been reported and their advantages and limitations also discussed. This review covers publications that have appeared since 2008.

## 1. Introduction

The monitoring of heavy metals within the environment, drinking water, food, and biological fluids has become essential due to the raising of environmental awareness and increasingly stringent regulations for pollution control. Heavy metals, by definition, are metals with densities of  $>5 \text{ g cm}^{-3}$ . They are released into the environment mainly by industrial activities. In small quantities, certain heavy metals such as iron, copper, manganese, and zinc are nutritionally essential for a healthier life. However, heavy metals such as Hg, As, Pb, and Cd are highly toxic and carcinogenic, even at the trace level [1, 2]. The toxicity and bioaccumulative properties of most heavy metals make its control a top-priority environmental task. Table 1 summarises the standards and guidelines for heavy metals in drinking water set by the World Health Organization (WHO), U.S. Environmental Protection Agency (EPA), and European Union (EU) legislation [3–5].

Standard methods for heavy metal determination cover a wide range of laboratory-based techniques such as atomic

absorption spectroscopy (AAS), inductively coupled plasma-atomic emission spectroscopy (ICP-AES), inductively coupled plasma-mass spectrometry (ICP-MS), and X-ray fluorescence spectroscopy (XFS) [6–12]. Although these methods are sensitive and selective they require time-intensive sampled pretreatment and expensive analytical instrumentation, as well as highly qualified staff. On the other hand, optical chemical sensors (OCSs) have great potential for detecting multiple heavy metals on-site. OCSs are a group of chemical sensors in which electromagnetic (EM) radiation is used to generate an analytical signal in a transduction element. The interaction of this radiation with the sample causes the change of a particular optical parameter that can be related to the concentration of the analyte [13, 14]. OCSs usually rely on the principle of an immobilised indicator (organic dye) that changes its optical properties (absorption, transmission, emission, lifetime, etc.) on binding the analyte [15–17]. When designing an OCS with the desired sensor characteristics, it is not only the selection of a suitable indicator, solid support (matrix), and immobilisation technique that is important but also the morphology and suitable functionalisation of

TABLE 1: Standards and guidelines for heavy metals in drinking water set by WHO, EPA, and EU legislation [3–5].

Metal	WHO (mg/L)	EPA (mg/L)	EU (mg/L)
Hg	0.006	0.002	0.001
Cu	2	1.3	2
Zn	—	5	—
Pb	0.010	0.015	0.01
Cr	0.05	0.1	0.05

such materials [18]. Over the years, different optical chemical sensors have been introduced based on silica mesoporous materials for the determination of mercury [19–34], copper [35–38], zinc [39–42], and other heavy metal ions [43–48].

The purpose of the presented review was to provide a general overview on the latest studies relating to mesoporous silica-based optical chemical sensors for heavy metals' determination. The papers in question mainly focused on the receptor part of the OCS and not on the development of the whole sensor system including the transducer and signal processing unit. The syntheses, properties, and other applications of mesoporous materials are already described in detail elsewhere [49–54].

## 2. Mesoporous Material

Over the past decade, mesoporous materials due to their highly porous natures combined with low absorption and emission within the visible spectra have been shown to be excellent candidates for OCSs. Mesoporous materials are a class of nanostructures with well-defined mesoscale (2–50 nm diameters) pores, surface areas up to 1000 m<sup>2</sup>/g, and large pore volumes (~1.0 mL/g). In general, these ordered mesostructured materials are formed from solution by the coassembly and cross-linking of network-forming inorganic species (typically oxides) in the presence of structure-directing agents (SDAs) [55]. The SDAs are typically surfactants or block copolymers that self-organise into mesoscale (2–50 nm) structures, according to the solution's composition and the used processing conditions [56]. Mesoporous inorganic materials can have various mesophase structures, for example: 2D-hexagonal (space group *p6mm*), biscontinuous cubic (space groups *Ia-3d*, *Pn-3m*, and *Im-3m*), cage-type cubic (space groups *Pm-3n*, *Fm-3m*, *Im-3m*, *Fd-3m*, etc.), cage-type hexagonal (space group *P6<sub>3</sub>/mmc*), lamellar (L, space group *p2*), and others (space groups *P4<sub>2</sub>/mnm*, *P4/mmm*, *c2mm*, *Pmmm*, etc.), Table 2 [52, 53, 57]. The structures of the mesoporous materials are highly dependent on the geometries of the surfactants, including the sizes and charging of the head groups, the length and saturation of the hydrophobic tail, and its molecular shape.

From amongst several families of mesoporous silica materials (MPS) already developed and used in sensor applications, it is worth mentioning the more typical MCM [19, 32, 33, 36, 39, 42, 58–65], SBA [21–28, 34, 35, 45, 48, 58, 60, 66], HOM [20, 36, 43–46, 67], HMS [29, 38].

TABLE 2: List of some typical mesoporous silica materials and their mesophase structures.

Mesophase structure	Space group	Material or researcher	Ref.
2D-hexagonal	<i>p6mm</i>	MCM-41	[32, 33, 36, 39, 42, 58–63]
		SBA-15	[22–28, 35, 45, 48, 58, 60]
		HOM-2	[43]
3D-biscontinuous cubic	<i>Ia3d</i>	MCM-48	[63]
		KIT-6	[91]
		FDU-5	[92]
	<i>Pn3m</i>	HOM-5	[93–95]
		HOM-7	[96]
		AMS-10	[97]
3D-cage-type cubic	<i>Im3m</i>	SBA-16	[98]
		<i>Pm3n</i>	SBA-1 [99–101]
		SBA-6 [100, 101]	
		HOM-9 [20, 46]	
		SBA-2 [99]	
	<i>Fm3m</i>	SBA-12 [98]	
		HOM-10 [46]	
		FDU-12 [102]	
		KIT-5 [103]	
		FDU-1 [104]	
3D-cage-type hexagonal	<i>P6<sub>3</sub>/mmc</i>	<i>Im3m</i>	SBA-16 [98]
		FDU-2 [105]	
		<i>Fd3m</i>	AMS-8 [106]
		HOM-11 [36, 44]	
		SBA-2 [99]	
Lamellar	<i>P6<sub>3</sub>/mmc</i>	SBA-12 [98]	
		SBA-7 [98]	
		HOM-3 [93, 94]	
Lamellar		MCM-50 [107, 108]	

The structures of the more studied mesoporous materials for sensor applications are presented in Figure 1.

The use of MPS as a solid support for the fabrications of OCSs has many advantages. MPS materials allow covalent immobilisation either (a) by covalently anchoring the active sensor dye during synthesis and low-temperature removal of the structure-directing agent or (b) by the grafting of indicator dyes via postsynthetic functionalisation making them even more desirable in sensor applications, since leaching is minimised in this way. The sensor properties can be significantly altered by the method chosen for indicator immobilisation [17, 46, 68]. In general, high concentrations of dye molecules often lead to significant fluorescent self-quenching resulting from intermolecular collisions, since all the molecules are completely free within the solution [68].

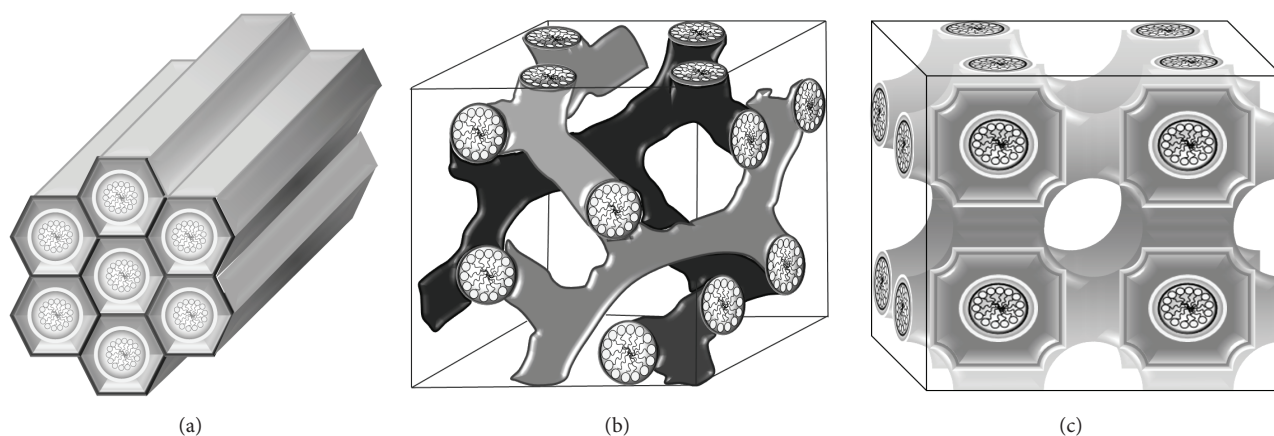


FIGURE 1: Structures of mesoporous materials. (a) 2D-hexagonal (space group  $p6mm$ ); (b) biscontinuous cubic (space groups  $Ia-3d$ ); (c) cage-type cubic (space groups  $Pm3n$ ).

Moreover, it is known that the packaging of dye molecules within a solid base will also cause self-quenching. MPS materials have abundant pore channels and surface silanol groups; therefore, dye molecules can be highly dispersed throughout the pore channels of MPSs and fixed at different locations of the pore's surface by reaction with silanol groups, which means that the mobility and rotation of the dye is restricted to a fixed area. Therefore the dye molecules are densely located in MPSs, and the generally observed self-quenching in the dye solution with high concentration can be reduced considerably [37, 40]. It has been reported that the fluorescence of the dye inside the MPS particles does not quench, although its concentration is  $\approx 230$  times higher than the maximum nonquenching concentration of the free dye in the solution [68–70]. The high concentrations of the dye immobilised in MPS improves the signal-to-noise ratio and can also affect the sensor's sensitivity and detection limit (LOD). Furthermore, the ability to control the pore size, tailor the composition of the inorganic framework and internal pore-surface or channel, can affect or improve the sensor's selectivity [26, 44, 71], since limited accessibility can help to shield the dyes from interferences. Moreover, it has also been shown that the 3D shapes and geometries of mesopores have a significant effect on LOD and response time ( $t_R$ ) (3D compared to 2D). This can be related to the fact that 3D morphologies and cage functionalities are expected to transport analyte efficiently using much more direct and easier diffusion to network sites [46, 47]. An additional benefit of mesoporous materials is also that they can be prepared in various morphological forms such as thin-films, nanoparticles, and monoliths. The exceptional adsorption capacities of mesoporous materials may serve as in-situ preconcentrators for analyte, thus improving the LOD of a MPS-based sensor [20, 36, 44, 47].

The interesting fields of usage regarding MPS materials for optical sensing have been reviewed a few times over recent years. In 2008, Melde et al. [72] reviewed how mesoporous silicas had been applied to sensing optical and electrochemical changes in relative humidity, changes in pH, metal cations, toxic industrial compounds, volatile organic compounds,

small molecular ions, nitroenergetic compounds, and biologically relevant molecules. A tutorial review published by Han et al. in 2009 [73] reported on the development of silica-based organic/inorganic hybrid nanomaterials for use within biological and environmental applications, in which the chromogenic and fluorogenic probes can selectively detect and separate specific anions and neutral organic guests, as well as toxic metal ions. Recently, Jung et al. [74] reviewed the preparing of a variety of silica nanotubes by self-assembled organogels and the recent development of silica-based organic-inorganic hybrid nanomaterials for use as chemosensors for environmental studies, as well as within biological applications. Tran-Thi et al. [75] noticed that sol-gel porous materials with tailored nanostructured cavities were being increasingly used with regard to their potential as sensitive matrices or layers of chemical sensors for the determination of gaseous and ionic analytes.

### 3. Sensing Mechanisms

The more commonly applied methods for the optical sensing of heavy metals using mesoporous materials are those based on light absorption or light emission. Absorption or colorimetric sensing is accomplished using an indicator that changes its colour upon binding the analyte; this change is not only spectroscopically determined but can also be observed visibly [14, 76]. In light-emission methods, the analyte concentration is determined by the change in the emission properties of a luminophore after being excited by a defined electromagnetic wavelength. Fluorescence typically occurs from aromatic molecules due to the rigid conjugated structure and the high rigid density of  $\pi$  electrons [77]. Compared to the absorption-based methods, molecular emissions (fluorescence, phosphorescence, and, generally speaking, luminescence) are particularly important because of their extreme sensitivities and good specificities. The sensitivity of the luminescence method is about 1000 times greater than that of most spectrophotometric methods. In addition, lower LOD for the desired analytes can be achieved [76–80].

Measuring the emission intensity is also the most popular because the instrumentation needed is very simple and cheap. Nevertheless, measuring light-emission intensity has some disadvantages compared to emission lifetime measurements, in which the sample is excited only by a pulse of EM rather than via continuous illumination, which is the case with intensity-based methods. The precisions and accuracies of luminescence intensity-based schemes are greatly affected by fluctuations in the light-source's intensity, detector sensitivity, inner filter effects, indicator concentration (bleaching and leaching), sample turbidity, and sensing layer thickness. One method of reducing the problems associated with intensity detection principles is the use of ratiometric measurements. This technique employs dual emission or dual excitation indicators or mixtures of two luminophores, exhibiting separated spectral areas with different behaviour. For example, the ratio of two fluorescent peaks is used instead of the absolute intensity of one peak. The sensors therefore typically contain a reference dye; the advantage of this approach is that factors such as excitation source fluctuations and sensor concentration will not affect the ratio between the fluorescence intensities of the indicator and reference dye [81–83].

When a fluorescent indicator is used for sensing heavy metals, the complexation of the metal ions with the indicator results in either enhanced fluorescence (chelation-enhanced fluorescence—CHEF) or in decreased fluorescence (chelation-enhanced quenching—CHEQ). These mechanisms usually involve electron transfer (ET) and charge transfer (CT). Accordingly, these categories include photoinduced electron transfer (PET) and photoinduced charge transfer (PCT), also called intramolecular charge transfer. The PET mechanism is the more widely accepted and belongs to the group of turn-on fluorescent sensors, which fluoresce only in the presence of analytes. Sensors based on the PET mechanism often use a rational combination of a triple component system, namely, the “fluorophore-spacer-ionophore” format [84]. The receptor contains a high-energy nonbonding electron pair (e.g., nitrogen or sulphur atoms), which can transfer an electron to an excited fluorophore group and result in fluorescence quenching. However, when the electron pair is coordinated by a metal ion, the electron transfer will be prevented and the fluorescence is switched on [85, 86]. The principle is shown in Figure 2. PET type fluorescent response does not cause any spectroscopic shifts in the emission band regarding the complexation of the metal ions [86].

The PCT mechanism involves the transfer of an electron between the donor and acceptor functionalities in order to promote fluorescence [86, 87]. All the indicators have integrated ionophore and fluorophore, as opposed to the PET indicators that have the electron donor moiety separated by spacer from the fluorophore. For this reason, with PCT indicators, the complexation of the metal ions give rise to alterations in electron-energy levels causing fluorescence turn-off or turn-on and a variation in emission and absorption wavelengths (Figure 3), depending on the type of fluorophore, metal ion, and complexation mode [86]. More detailed descriptions of sensing mechanisms are described elsewhere [86–88].

Basically, the turn-on or increasing of fluorescence emissions is a better approach than quenching because in real samples there are many species that can in fact quench the fluorophore emission besides the analyte (e.g., oxygen and other heavy metals). In case an insufficient selective indicator is applied, the sensing mechanism based on fluorescence quenching can be prone to several interferences.

#### 4. Continuous Monitoring

The concentrations of trace metals within natural waters vary considerably as functions over time, depending on the discharger sources, seasons, types of urban activities, and so forth. The monitoring of dissolved heavy metals such as copper, lead, and cadmium over four-day periods within coastal waters showed that potentially most toxic forms of metals may vary in concentrations over a time scale of less than one hour [89]. These data confirm the poor ecological relevance of the average conventional sampling protocol and the need for continuous monitoring.

Conventionally, ions have been determined by making use of so-called indicator dyes that undergo a binding reaction with ions. The ion-binding reactions with indicators are reversible in principle [90]. In practice, however, most complexation reactions with heavy metals are irreversible. The indicator is essentially saturated with metal ions and any further increase in metal ion concentration produces little if any change in the observed signal. The decomplexation procedure is used for sensor regeneration/reusage, which needs the appropriate stripping agent. EDTA and  $\text{ClO}^-$  stripping agents are used mostly. In the best case the reusage cycle can be repeated up to 6 times.

#### 5. Specific Sensors for Heavy Metals' Ions

The determination of toxic heavy metal cations by mesoporous material sensors/probes is usually based on the incorporation of appropriate dye molecules within selected mesoporous materials, where either absorbance or fluorescence is used as an optical detection method. Since 2008, researchers have mostly developed mesoporous materials for sensing mercury ( $\text{Hg}^{2+}$ ) and copper ( $\text{Cu}^{2+}$ ). Materials for sensing other cations have also been proposed (zinc, lead, cobalt, chromium, etc.).

*5.1. Mercury Sensing.* The determination of mercury ions has been a subject of investigation by different research groups (Table 3). Most of the sensing materials use fluorescence as a detection principle, whilst only a few use absorption. In regard to  $\text{Hg}^{2+}$  sensing material, SBA-15 is mostly used [21–28]. Other mesoporous materials such as UVM-7 [19], HOM-9 [20], Au-HMS [28] core-shell MPS nanoparticles [30, 31], and MCM-41 [32, 33] have also been studied. The more often used is covalent bonding of the indicator dye to the mesoporous material but immobilisation via H-bonds [23] or ionic bonds [20] is also possible.

In 2008, Ros-Liz et al. [19] reported on the fabrication of dual-function hybrid material for the simultaneous

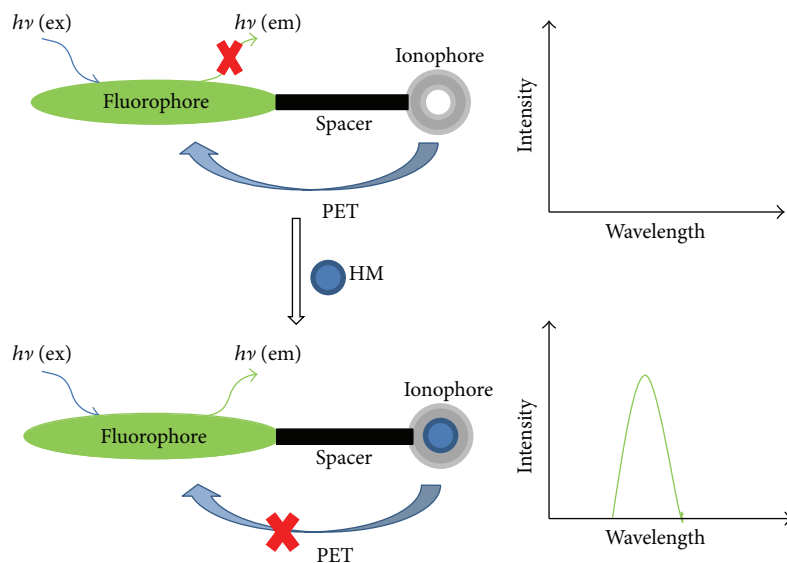


FIGURE 2: Principle of heavy metal recognition by fluorescent PET sensors.

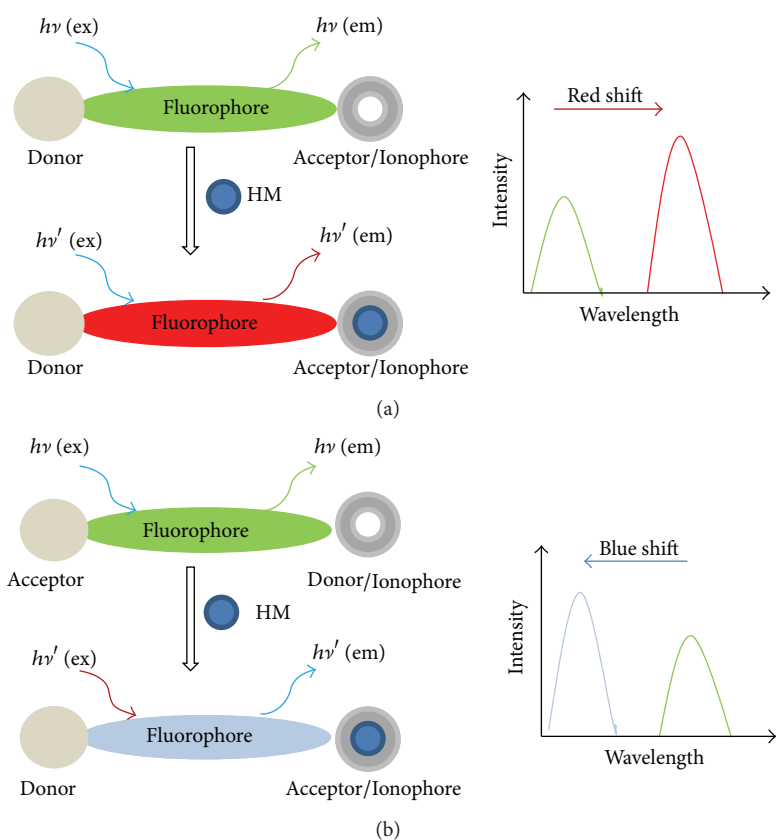


FIGURE 3: Principle of heavy metal recognition by fluorescent PCT sensors.

determination and removal (adsorbent) of  $\text{Hg}^{2+}$  ions within acetonitrile/water (1 : 1) solutions. A mesoporous 3D material such as UVM-7 was used as an inorganic support. The sensing principle is based on a chemodosimeter approach. In this case, a chromofluorogenic squaraine dye is first “switched-off” (colorless and nonfluorescent) by reacting to  $-\text{SH}$  groups

attached to a silica framework. The addition of sensing material to the solution containing  $\text{Hg}^{2+}$  ions results in a rapid and dramatic colour change of the solution from colourless to deep blue (new absorption band at 642 nm), due to the dye released when  $\text{Hg}^{2+}$  reacts with  $-\text{SH}$  groups in sensing materials. After a two-minute reaction, the solid is collected

TABLE 3: Sensors for  $\text{Hg}^{2+}$  determination.

Indicator dye	Material	Detection principle	Working range (M)	LOD (M)	$t_R$ (s)	Ref.
Squaraine	UVM-7	Absorption (turn-on)	$4.9 \times 10^{-7}$ – $4.9 \times 10^{-4}$	$4.9 \times 10^{-7}$	120	[19]
TPPS	HOM-9	Absorption (colour change)	$5.9 \times 10^{-9}$ – $1.7 \times 10^{-5}$	$5.9 \times 10^{-9}$	60	[20]
Acyclic dye	SBA-15	Absorption (colour change)	$1$ – $10 \times 10^{-6}$	$1 \times 10^{-6}$	~10	[21]
R6G	SBA-15	Fluorescence enhancement	$4.9 \times 10^{-9}$ – $4.5 \times 10^{-7}$	$4.9 \times 10^{-9}$	Not given	[22]
R6G	SBA-15	Fluorescence enhancement	$4.9 \times 10^{-9}$ – $6.5 \times 10^{-8}$	$4.9 \times 10^{-9}$	Not given	[23]
R6G	SBA-15	Fluorescence enhancement	$1 \times 10^{-8}$ – $4 \times 10^{-8}$	$1 \times 10^{-8}$	Not given	[24]
Pyrene	SBA-15	Fluorescence enhancement	$8.5 \times 10^{-7}$ – $2 \times 10^{-5}$	$8.5 \times 10^{-7}$	Few seconds	[25]
Ethynylpyrene	SBA-15	Fluorescence enhancement	$0.2 \times 10^{-8}$ – $3 \times 10^{-5}$	$2 \times 10^{-8}$	Not given	[26]
DS	SBA-15	Fluorescence quenching	$10^{-6}$ – $10^{-3}$	$10^{-6}$	Not given	[27]
RhB	SBA-15	Fluorescence (turn-on)	Not given	$1.5 \times 10^{-8}$	Not given	[28]
RhB	Au-HMS	Fluorescence (turn-on)	$7 \times 10^{-8}$ – $7.5 \times 10^{-6}$	$7 \times 10^{-8}$	100	[29]
Pyrene	Core-shell MPS NPs	Fluorescence enhancement	$1.7 \times 10^{-8}$ – $9 \times 10^{-5}$	$1.7 \times 10^{-8}$	Not given	[30]
Pyrene	Core-shell MPS NPs	Fluorescence enhancement	$8.5 \times 10^{-7}$ – $9 \times 10^{-5}$	$8.5 \times 10^{-7}$	14	[31]
Azo dye	MCM-41 NPs	Absorption (colour change)	Not given	$9.97 \times 10^{-6}$	Not given	[32]
Eu(PTA)	MCM-41	Fluorescence quenching	$1$ – $12 \times 10^{-6}$	$1 \times 10^{-6}$	Not given	[33]

by filtration and the absorbance of the resulting solution measured. Inorganic support can be partially regenerated by sample washing with concentrated HCl, which quantitatively removes the loaded mercury, and the material can therefore be used for several cycles. The apparent LOD of the probe is  $4.9 \times 10^{-7}$  M (0.1 ppm). Interestingly, the authors did not try to reduce the LOD by measuring the fluorescence. In addition, the leaching of the dye from the inorganic support raises the question of such a system regarding its practical application. A different approach was used by El-Safty et al. [20], where solid mesoporous cubic  $Pm3n$  discs were used for the simultaneous naked-eye detection and removal of mercury ions within aquatic samples. This method was based on a design of disc-like (HOM-9) sensors by the immobilisation of two different organic groups, however, the first an organic moiety for changing the silica surface polarity and the second a tetraphenylporphine tetrasulphonic acid (TPPS) probe for  $\text{Hg}^{2+}$  ions that showed prominent colour-change when in contact with the analyte. The sensing assay exhibited a  $t_R$  of 1 min and LOD of  $5.9 \times 10^{-9}$  M at pH 9. The reversibility of the disc-like sensor allowed for the retention of its functionality (sensitivity and fast  $t_R$ ) after multiple regeneration/reuse cycles using  $\text{ClO}_4^-$  as the decomplexation agent. After multiple regeneration/reuse cycles ( $\geq 6$ ) there was a kinetic hindrance, as the  $t_R$  was prolonged to 2 min but the sensitivity stayed at up to 92% and the disc was fully reversible. In 2008, and 2010 Kim et al. [21, 34] synthesised a  $\text{Hg}^{2+}$  sensitive acyclic dye which was immobilised on the surface of MPS. The sensing material was a light yellow solid and resulted in a colour change from light yellow to red within 10 s in the presence of  $\text{Hg}^{2+}$ . The removal of  $\text{Hg}^{2+}$  (regeneration) was carried out by the addition of EDTA. A linear response was observed within the concentration range  $1$ – $10 \times 10^{-6}$  M with an LOD of  $\sim 1 \times 10^{-6}$  M [15]. The mesoporous silica-immobilised acyclic dye recognised the  $\text{Hg}^{2+}$  with a high degree of selectivity from amongst other metal ions within the aqueous solution.

Inorganic-organic hybrid fluorescence-based SBA-15 mesoporous materials have been reported over past years (Table 3). In 2008, Zhou et al. [22] reported a fluorescent sensor, R6-SBA-15, for the determination of  $\text{Hg}^{2+}$  within acetonitrile/water (7:3) solution by the covalent bonding of an organic fluorescent molecule Rhodamine 6G (R6G) within the channel of mesoporous silica. In 2010, they published another article [23] involving the same indicator dye for  $\text{Hg}^{2+}$  determination within dimethylformamide/water (1:1) solution that was assembled into SBA-15 (RBSN/SBA-15) through intermolecular hydrogen bonding, instead of covalent bonding [22]. Both SBA-15-based sensors resulted in a slight pink powder that could quantitatively determine  $\text{Hg}^{2+}$  at the  $10^{-9}$  M (ppb) level. However, it would be interesting to know and compare the  $t_R$  of the two described R6G-based sensors, since the dyes were immobilised by two different approaches. Namely, it was shown that covalent-bonding can significantly prolong the  $t_R$  of the sensor [17]. Moreover, from the practical point of view it would be advisable to perform the measurements in water. Wu et al. [24] fabricated a Rhodamine- (R6G-) based SBA-15 sensor that can be used to detect  $\text{Hg}^{2+}$  ions in water. However, the sensor's LOD ( $1 \times 10^{-8}$  M) compared to previously developed sensors [22, 23] was poorer. Fluorescent detection of  $\text{Hg}^{2+}$  ions was also proposed using pyrene-based fluorescent dye [25, 26] and the dansylamine derivate (DS) [27], being covalently grafted onto SBA-15. All the sensors showed good sensitivities and selectivities for  $\text{Hg}^{2+}$ . Dong et al. [28] have prepared a Rhodamine group modified SBA-15 nanocomposite for the determination of  $\text{Hg}^{2+}$  ions in MeCN- $\text{H}_2\text{O}$  solution (9:1 v/v).

Recently, Zhang et al. [29] prepared a worm-like pore-structured mesoporous silica-based (HMS) sensor (Au-HMS-sensor). In this case, gold was used as a connector to prepare Au-HMS and determination was possible through Rhodamine B derivate, covalently grafted on Au-HMS. This sensor exhibited “turn-on” fluorescence enhancement and

showed good selectivity for  $\text{Hg}^{2+}$  over other metal ions. LOD of  $7 \times 10^{-8}$  M concentration was reached within 100 s. The Au-HMS-sensor was successively regenerated by treatment with tetrapropylammonium hydroxide solution.

A different approach for detecting  $\text{Hg}^{2+}$  was used by Guo et al. [30] and Zhang et al. [31], who developed core-shell mesostructured silica as solid support, functionalised with pyrene. The LODs for both sensors were  $1.7 \times 10^{-8}$  M [30] and  $8.5 \times 10^{-7}$  M [31], respectively, whereas the linear working concentration range was between  $10^{-8}$  and  $10^{-4}$  M in both cases. In comparison with the covalently grafted pyrene-SBA-15 sensor [25] the LOD of the core-shell-based system is 50 times lower [30].

MCM-41 mesoporous materials have also been used for preparation of the  $\text{Hg}^{2+}$  sensor [32, 34]. However, compared to other mesoporous materials, it seems that MCM-41 is not the best material for the fabrication of  $\text{Hg}^{2+}$  sensors, since both of the two sensors have rather high LODs.

In view of water legislation, the LODs of the majority of the mentioned sensors are still far from the “ $0.05 \mu\text{g/L}$  ( $2.5 \times 10^{-10}$  M)” target [109]. The sensors developed by Zhou et al. [22] and Song et al. [23] have the lowest LODs and can detect the maximum allowed contaminant level of  $1 \mu\text{g/L}$  ( $4.98 \times 10^{-9}$  M) set by EU legislation for drinking water [5]. Only a few papers [26, 30] have shown the practical applicabilities of the proposed sensors by evaluating them using real samples. Most of them lack water compatibility and need to be used in organic or aqueous organic solvents. Nevertheless, most  $\text{Hg}^{2+}$  sensors have demonstrated high selectivity towards other competing metal cations, showing that mesoporous structures may exhibit high selectivity potential, which is also an important sensor characteristic. Furthermore, the response time is also an important sensor characteristic, which has been overlooked by many authors.

**5.2. Copper Sensing.** Copper(II) ions have been the subject of continuous control, as copper is commonly used throughout industry and is therefore a widespread pollutant. However, it is also an essential trace element that plays important roles in a variety of fundamental physiological processes within living organisms [110]. Two sensors are based on fluorescence quenching [35, 37] and two are based on colour change (absorption) [36, 38].

In 2010, Meng et al. [35] reported on an inorganic-organic silica material, prepared by covalent immobilisation of the 1,8-naphthylimide-based receptor (P2) within the channels of mesoporous silica material SBA-15 (SBA-P2). SBA-P2 exhibited a  $\text{Cu}^{2+}$  specific fluorescence-quenching response in ethanol/water (3:7) solution with an LOD of  $1.6 \times 10^{-9}$  M. The sensor was highly selective towards  $\text{Cu}^{2+}$  ions over the interfering ionic species. Furthermore, the SBA-P2 material was applied for the fluorescence imaging of zebrafish organisms and the subsequent addition of  $\text{Cu}^{2+}$  ions resulted in SBA-P2 emission quenching. Presumably, being the first report on detecting  $\text{Cu}^{2+}$  ions in vivo using a functionalised nanomaterial, these results suggest that MPS is potentially

useful for studying the toxicity or bioactivity of  $\text{Cu}^{2+}$  within living organisms. However, experiments regarding regeneration and  $t_R$  should be done additionally in order to further characterise the sensor characteristics. Recently, El-Safty et al. [36] constructed a Cu(II) ion sensor based on immobilised dithizone (DZ) in 2D hexagonal MCM-41 and 3D cubic *Fd3m* HOM-11 mesoporous silica microscopic monoliths. The reflectance spectra of this sensor exhibited a blue shift as a result of the binding of  $\text{Cu}^{2+}$  ions with the DZ. 3D shape and the geometries of the mesoporous materials significantly affected the ion diffusion and affinity of the metal-ligand binding, thus affecting the sensor's characteristics. The sensors exhibited specific behaviour by permitting Cu(II) ion-selective determination in the model wastewater, despite the presence of active component species. The LODs were  $3.1 \times 10^{-8}$  M and  $12.5 \times 10^{-8}$  M for 3D cubic *Fd3m* HOM-11 and 2D-hexagonal MCM-41, respectively. The  $t_R$  of HOM-11 (3D) was 20 s shorter compared to MCM-41 (2D).

On the other hand, Lu et al. [37] used monodispersed mesoporous silica nanospheres modified by anthracene derivative (SGAAn) and fabricated a fluorescent sensor for the determination of  $\text{Cu}^{2+}$  metal ions in ethanol/water (3:7) solution. Determination of  $\text{Cu}^{2+}$  ions was possible through fluorescent quenching of the modified spheres in a few seconds within a concentration range from  $5 \times 10^{-8}$  to  $10^{-4}$  M of  $\text{Cu}^{2+}$ , with the LOD being  $2 \times 10^{-8}$  M. The recovery of the sensor was repeatedly studied over 4 cycles by the use of EDTA as the recovery agent. Liu et al. [38] designed an absorption-based sensor for  $\text{Cu}^{2+}$  by using an indicator 4-(2-pyridylazo) rescinol (PAR) immobilised on functionalised hexagonal mesoporous silica (HMS). Determination of  $\text{Cu}^{2+}$  ions was possible under strong acidic conditions (pH 12) through colour change from yellow to red of the modified spheres in 60 seconds within a concentration range from  $6.3 \times 10^{-7}$  M to  $6.3 \times 10^{-6}$  M of  $\text{Cu}^{2+}$ , with LOD being  $1.3 \times 10^{-8}$  M. With the addition of EDTA as a regenerating agent, the sensor is reusable and can be used up to 6 times. The authors also showed a potential for developing sensors for other ions, such as  $\text{Fe}^{3+}$ ,  $\text{Cd}^{2+}$ ,  $\text{Ni}^{2+}$ ,  $\text{Zn}^{2+}$ ,  $\text{Pb}^{2+}$ ,  $\text{Co}^{2+}$ , and  $\text{Hg}^{2+}$ , using this sensor design.

All of the reported sensors (Table 4) satisfied the quality of the  $\text{Cu}^{2+}$  parameter for water intended for human consumption ( $2 \text{ mg/L}$  or  $3.1 \times 10^{-5}$  M) as set by the EU directive [5], WHO [3], and EPA [4].

**5.3. Sensing of Other Heavy Metal Ions.** Table 4 summarises the recently developed mesoporous silica-based sensors used for heavy metal cation sensing, including  $\text{Zn}^{2+}$ ,  $\text{Pb}^{2+}$ ,  $\text{Co}^{2+}$ ,  $\text{Bi}^{3+}$ ,  $\text{Cr}^{3+}$ , and  $\text{Cr}^{6+}$ .

The determination of  $\text{Zn}^{2+}$  ions is possible using ordered MPS material MCM-41 functionalised with quinoline derivative N-(quinolin-8-yl)-2-[3-(triethoxysilyl)propylamino]acetamide (QTEPA) [39]. This reported system selectively detects  $\text{Zn}^{2+}$  ions with LOD of  $0.1 \times 10^{-6}$  M and a working range of  $0.01\text{--}30 \times 10^{-6}$  M. The presence of other metal ions did not affect the selectivity, even at high concentrations of  $\text{Na}^+$ ,  $\text{K}^+$ ,  $\text{Ca}^{2+}$ , and  $\text{Mg}^{2+}$  along with  $\text{Zn}^{2+}$  ions

TABLE 4: Properties of OCSs for selected heavy metal ions.

Analyte	Indicator dye	Material	Detection principle	Working range (M)	LOD (M)	$t_R$	Ref.
Cu <sup>2+</sup>	P2	SBA-15	Fluorescence quenching	$1.6 \times 10^{-9}$ – $1.1 \times 10^{-8}$	$1.6 \times 10^{-9}$	Not given	[35]
Cu <sup>2+</sup>	DZ	HOM-11	Absorption (colour change)	$1.57 \times 10^{-8}$ – $7.86 \times 10^{-6}$	$3.1 \times 10^{-8}$	60 s	[36]
		MCM-41		$7.86 \times 10^{-8}$ – $7.86 \times 10^{-6}$	$12.5 \times 10^{-8}$	80 s	
Cu <sup>2+</sup>	SGAAn	Type not defined	Fluorescence quenching	$5 \times 10^{-8}$ – $10^{-4}$	$2 \times 10^{-8}$	4–5 s	[37]
Cu <sup>2+</sup>	PAR	HMS	Absorption (colour change)	$6.3 \times 10^{-7}$ – $6.3 \times 10^{-6}$	$1.3 \times 10^{-8}$	60 s	[38]
Zn <sup>2+</sup>	QTEPA	MCM-41	Fluorescence enhancement	$0.1 \times 10^{-6}$ – $30 \times 10^{-6}$	$0.1 \times 10^{-6}$	Not given	[39]
Zn <sup>2+</sup>	8-AQ	Type not defined	Fluorescence enhancement	$5 \times 10^{-8}$ – $2 \times 10^{-5}$	$2 \times 10^{-8}$	Not given	[40]
Zn <sup>2+</sup>	SSD	Type not defined	Fluorescence enhancement	Not given	$70 \times 10^{-9}$	Not given	[41]
Zn <sup>2+</sup>	8-HQ	MCM-41	Fluorescence enhancement	Not given	$1.2 \times 10^{-6}$	30 s	[42]
Cd <sup>2+</sup>					$1.9 \times 10^{-9}$	30 s	
Co <sup>2+</sup>	Azo dye	HOM-2	Absorption (colour change)	$1.7 \times 10^{-8}$ – $17 \times 10^{-6}$	$\sim 15 \times 10^{-9}$	15 min	[43]
Bi <sup>3+</sup>	DZ	HOM-11 (3.2 nm pore size)	Absorption (colour change)	$2.3 \times 10^{-9}$ – $9.6 \times 10^{-6}$	$6.5 \times 10^{-10}$	20 s	[44]
		MCM-41		$2.39 \times 10^{-8}$ – $9.6 \times 10^{-6}$	$8.1 \times 10^{-9}$	40 s	
Cr <sup>3+</sup>	R6G	SBA-15	Fluorescence enhancement	$1 \times 10^{-6}$ – $6 \times 10^{-6}$	$1 \times 10^{-6}$	Not given	[45]
Cr <sup>6+</sup>	DPC			$13.3 \times 10^{-10}$ – $3.8 \times 10^{-6}$	$8.1 \times 10^{-10}$	60 s	
Pd <sup>2+</sup>	TPPS	HOM-10	Absorption (colour change)	$9.4 \times 10^{-9}$ – $9.4 \times 10^{-6}$	$2.3 \times 10^{-9}$	80 s	[46]
Co <sup>2+</sup>	PR			$8.4 \times 10^{-9}$ – $1.7 \times 10^{-5}$	$2 \times 10^{-9}$	45 s	
Pb <sup>2+</sup>	DZ			$2.4 \times 10^{-10}$ – $4.8 \times 10^{-6}$	$2.7 \times 10^{-11}$	60 s	
Pb <sup>2+</sup>	DTAR	HOM-13	Absorption (colour change)	$4.8 \times 10^{-8}$ – $4.83 \times 10^{-7}$	$13 \times 10^{-9}$	12.5–17.5 min	[46]
		HOM-9		$2.4 \times 10^{-8}$ – $7.2 \times 10^{-7}$	$9 \times 10^{-9}$	5–7 min	
Pb <sup>2+</sup>	PMBA	SBA-15	Fluorescence quenching	$2 \times 10^{-6}$ – $50 \times 10^{-6}$	$0.5 \times 10^{-9}$	Immediate response	[48]

in solution. On the other hand, transition metals, from iron to copper, competed with the binding sites, even though there was an overall increase in fluorescence intensity with Zn<sup>2+</sup> binding. Core-shell mesoporous silica nanospheres encapsulated with Rhodamine 101 into the solid core and 8-aminoquinoline derivatives (AQ) into the mesoporous shell were used as Zn<sup>2+</sup> ratiometric fluorescent sensor [40]. The fluorescence intensity of 8-AQ dramatically increased after the addition of Zn<sup>2+</sup> ions. Concentrations as low as  $5 \times 10^{-8}$  M could be detected in ethanol-water solution (30%). Recently, Shahid et al. [41] reported on the development of a fluorescent-based Zn<sup>2+</sup> sensor using MPS beads on which the fluorescent bis chromophoric dye containing naphthalimide and anthracene moieties (SSD) was covalently immobilised. The complexation between the fluorescent silica beads and Zn<sup>2+</sup> ions ( $50 \times 10^{-6}$  M) caused a ~6-fold increase in fluorescence intensity, accompanied by a 13 nm blue shift of the emission maxima. The sensor was selective for Zn<sup>2+</sup> in the presence of other metal ion interactions and had a LOD of  $70 \times 10^{-9}$  M. The regeneration of the sensor was carried out using EDTA. Tan et al. [42] developed an imprinted mesoporous silica (MCM-41)-based fluorescence sensing arrays for metal ions (Zn<sup>2+</sup> and Cd<sup>2+</sup>). A fluorescent functional monomer containing an 8-hydroxyquinoline (8-HQ) moiety in combination with a one-pot cocondensation method was employed for preparing the sensor array. The LODs for Zn<sup>2+</sup> and Cd<sup>2+</sup> were  $1.2 \times 10^{-6}$  M and  $1.9 \times 10^{-6}$  M, respectively, and were achieved within 30 s. Nevertheless,

both imprinted materials were, to some extent, cross-responsive towards nontemplate metal ions such as Mg<sup>2+</sup>, Ca<sup>2+</sup>, and Mg<sup>3+</sup> and optimisation of the method is needed.

The absorption monitoring of Co<sup>2+</sup> ions can be performed by the use of sensing materials designed by the direct physical adsorption of 8-(4-*n*-dodecyl-phenylazo)2,4-quinolinediol (azo dye) with long hydrophobic tails, onto hexagonal MPS monoliths (HOM-2) [43]. This sensor has a LOD of  $15 \times 10^{-9}$  M concentration of Co<sup>2+</sup> ions, achieved within minutes and a working range of between  $0.017$ – $17 \times 10^{-6}$  M. The sensor can be used up to 6 times with insignificant loss of sensing efficiency, although a slight decrease in sensing activity ( $t_R$ ) can be observed. The selectivity studies revealed no interferences from heavy metal ions such as Al<sup>3+</sup>, Bi<sup>3+</sup>, Cr<sup>6+</sup>, La<sup>3+</sup>, Ir<sup>3+</sup>, Sn<sup>2+</sup>, and Sb<sup>3+</sup>. However, interference was observed from Cu<sup>2+</sup>, Ni<sup>2+</sup>, Hg<sup>2+</sup>, and Zn<sup>2+</sup> ions that can be eliminated by using  $0.2 \times 10^{-3}$  M thiosulphate and thiocyanide. No leaching of the indicator dye from MPS was observed over a long period of time ( $\geq 4$  months), with only slight changes in the absorption spectra.

El-Safty et al. [44] designed absorption-based sensors for the determination of Bi<sup>3+</sup> ions by immobilising diphenylthiocarbazone (DZ) dye into a solid support without previously modifying the pore-surface. Different MPS monoliths were evaluated for solid support, such as 2D hexagonal-(MCM-41) and 3D cubic *Fd3m* (HOM-11). Additionally, the 3D structures were prepared of various pore sizes (2.3 nm, 2.8 nm, and 3.2 nm). The LOD of the MPS-immobilised dye

was ~1100-fold (MCM-41) or ~14000-fold (HOM-11, 3.2 nm pore-size) lower compared to the free dye, which indicated that the mesoporous matrix efficiently preconcentrates the analyte. The LODs were  $81 \times 10^{-10}$  M and  $6.5 \times 10^{-10}$  M for the 2D hexagonal and 3D cubic (3.2 nm pore-size) based sensors, respectively. The  $t_R$  of the 3D cubic-based sensor was about 15–20 s shorter than in the case of the 2D-hexagonal monolith. This study revealed that the pore-size of the 3D cubic mesoporous sensor affected the sensor's characteristics. Bigger pores provided lower LOD and shorter  $t_R$ . Although the DZ dye was physically entrapped within mesopores, no leaching was detected of the dye from the matrix. The sensors were highly selective towards other interfering compounds and could be reused 3 times.

Monitoring all forms of chromium (e.g.,  $\text{Cr}^{3+}$  and  $\text{Cr}^{6+}$ ) is necessary as they have toxic properties of high levels and are harmful to human health [111]. In 2011, Meng et al. [45] presented a multifunctional material that covalently linked the fluorescent dye Rhodamine 6G (R6G-TETA) and a mesoporous material (SBA-15), thus enabling fluorescent response and high adsorptivity for  $\text{Cr}^{3+}$  in water. The LOD of this method was  $1 \times 10^{-6}$  M and the working range was between  $1 \times 10^{-6}$  and  $6 \times 10^{-6}$  M. The functional nanomaterials' features provided good selectivity towards  $\text{Cr}^{3+}$  over the competitive cations. The sensor was also used *in vivo* and showed a potential for monitoring  $\text{Cr}^{3+}$  within living cells and organisms. Furthermore, a "building-block" approach for the immobilisation of indicator dye was used for the development of an optical sensor for  $\text{Cr}^{6+}$  ions determination [46, 67]. This approach is based on firstly modifying the polarities of the silica surface matrices with surfactant and then adsorption of the indicator dyes onto the solid support without the common use of silane- or thiol-coupling agents. In regard to the fabrication of DPC-based optical sensors using the building-block approach, several 3D mesoporous silica monoliths (3D HOM), such as cylindrical cubic *Fm3m* (HOM-10), cubic *Pm3n* with worm-like pore (HOM-13), and cage cubic *Pm3n* (HOM-9) materials, were used as solid supports. This study showed that pore ordering and the geometries of mesoporous materials affect the sensor's LOD and  $t_R$  but do not affect the sensor's selectivity. The LODs were  $8.1 \times 10^{-10}$  M,  $13.2 \times 10^{-10}$  M, and  $80 \times 10^{-9}$  M for HOM-10 and HOM-9 and HOM-13-based sensors, respectively; they were achieved within 60 s in the cases of HOM-10, HOM-9, and within 750 s in the case of the HOM-13-based sensor. The regeneration of the sensors was carried out by the addition of stripping agents ( $\text{EDTA}$ ,  $\text{ClO}_4^-$ ,  $\text{CH}_3\text{COO}^-$ , and  $\text{C}_2\text{O}_4^{2-}$ ) that enabled its reuse over more than 6 cycles.

El-Safty and co-workers [47] reported on an absorption-based  $\text{Pb}^{2+}$  nanosensor using 3D monoliths (wormhole and ordered mesostructures—HOM-type) as solid supports for the immobilisation of indicator dye 4-*n*-dodecyl-6-(2-thiazolylazo)-resorcinol (DTAR). Ordered (HOM-9) and wormhole (HOM-13) cubic *Pm3n* cage monoliths were fabricated via an instant direct-templating method using microemulsion systems by the addition of nonionic surfactants. The sensing characteristics are strongly defined by 3D pore geometry and the shapes of the monoliths,

thus influencing the  $t_R$  ( $5 \leq t_R \leq 7$  min for HOM-9 and  $t_R > 15$ –20 min for HOM-13), as well as working ranges of ( $0.048$ – $0.483 \times 10^{-6}$  M for HOM-13 and  $0.024$ – $0.724 \times 10^{-6}$  M for HOM-9). The prepared sensors exhibited good selectivity for  $\text{Pb}^{2+}$  and showed good efficiency after several regeneration cycles. Furthermore, there was no detected leaching of DTAR, although the dye was physisorbed into solid support. Wang et al. [48] prepared a series of hybrid fluorescent sensors by direct covalent-coupling of bis-schiff-based  $\text{N,N}'$ -(1,4-phenylenedimethylidene)bis-1,4-benzenediamine (PMBA) on the inner surface of MPS (SBA-15), functionalised with chlorine groups. The fluorescent sensor exhibited high selectivity and sensitivity towards  $\text{Pb}^{2+}$  ions with a LOD of  $0.55 \times 10^{-9}$  M (0.1 ppb) and a working range of  $2$ – $50 \times 10^{-6}$  M. However, there is no information on the sensor  $t_R$ . The DZ-HOM-10 sensor [46] had the lowest LOD compared to DTAR-HOM-9 [47] and PMBA-SBA-15 for the determination  $\text{Pb}^{2+}$ . All of them had LODs below the target value for  $\text{Pb}^{2+}$  set by the water directive 2008/32/EC [109] ( $3.4 \times 10^{-8}$  M or 7.2  $\mu\text{g/L}$ ).

## 6. Conclusions

Many published articles demonstrate that mesoporous materials are a good alternative to other solid supports (classical sol-gel materials, polymers) in OCS designs. Since mesoporous materials exhibit tuneable size- and shape-dependent chemical and physical properties, they have found applications for sensing various kinds of analytes.

In summary, the more frequently ordered SBA-15, MCM-41, and HOM mesoporous silica structures have been presented for sensing various heavy metal ions. Rare published studies on applying disordered worm-like materials have also been introduced. The sensors are mostly in the form of particles, rather than thin films. The majority of the published papers were devoted to the determination of mercury, which is one of the most toxic environmental contaminants. Besides the more explored SBA-15 material, MCM-41, and HOM were also reported as solid supports for sensing heavy metals, with SBA-15 being the preferable material of choice for mercury determination. It has been shown that 3D materials such as HOM are more suitable in terms of sensor sensitivity, response time and LOD as solid support, than 2D materials (SBA-15 and MCM-41).

The immobilisation of an indicator into MPS is usually carried out by covalent bonding. Interestingly, when physical entrapment of the organic dye was applied for sensing species in liquids, no indicator leaching was detected and therefore good results were observed in terms of stability.

In most cases, the MPS-based sensors showed good selectivity for the respective analytes. Furthermore, the improved adsorption properties of the heavy metals helped to lower the LOD. In spite of the fact that fluorescence is usually regarded as a more sensitive technique than spectrophotometry, it was also shown that LODs with MPS-based sensors are comparable for absorption and fluorescence-based systems.

The chemical and biological species in real-world samples such as river water, wastewater, and cells, have severe interferences on the sensing signal. Therefore, to show the practical implementation of the developed sensors, the sensors should be tested in real-world samples. However, most of the work only demonstrated a proof-of-concept for sensors that could detect heavy metals in buffer solutions, organic/water solutions, or artificial matrices. Only a few papers had reported the testing of real-world samples and only one paper had reported the sensors' validation data. There was no report on the development of cadmium and nickel MPS-based sensors, although cadmium and nickel are listed as target priority heavy metals by the Water Framework directive (2000/60/EC, 2006/11/EC, and 2008/105/EC). The on-line monitoring of heavy metals remains a significant challenge.

## References

- [1] J. H. Duffus, "Heavy metals—'a meaningless term?'" *Pure and Applied Chemistry*, vol. 74, no. 5, pp. 793–807, 2002.
- [2] G. Aragay, J. Pons, and A. Merkoçi, "Recent trends in macro-, micro-, and nanomaterial-based tools and strategies for heavy-metal detection," *Chemical Reviews*, vol. 111, no. 5, pp. 3433–3458, 2011.
- [3] WHO, *Guidelines for Drinking-Water Quality Volume I: Recommendations*, Geneva, Switzerland, 3rd edition, 2008.
- [4] U.S. Environmental Protection Agency, Risk Assessment, Management and Communication of Drinking Water Contamination, US EPA 625/4-89/024, EPA, Washington, DC, USA, 1989.
- [5] Council Directive 98/83/EC of 3 November 1998 on the quality of water intended for human consumption, pp. 90–112, 1998.
- [6] R. Kunkel and S. E. Manahan, "Atomic absorption analysis of strong heavy metal chelating agents in water and waste water," *Analytical Chemistry*, vol. 45, no. 8, pp. 1465–1468, 1973.
- [7] M. Lopez-Artiguez, A. Cameán, and M. Repetto, "Preconcentration of heavy metals in urine and quantification by inductively coupled plasma atomic emission spectrometry," *Journal of Analytical Toxicology*, vol. 17, no. 1, pp. 18–22, 1993.
- [8] N. H. Bings, A. Bogaerts, and J. A. C. Broekaert, "Atomic spectroscopy," *Analytical Chemistry*, vol. 78, no. 12, pp. 3917–3946, 2006.
- [9] P. Pohl, "Determination of metal content in honey by atomic absorption and emission spectrometries," *Trends in Analytical Chemistry*, vol. 28, no. 1, pp. 117–128, 2009.
- [10] J. Gasparik, D. Vladarova, M. Capcarova et al., "Concentration of lead, cadmium, mercury and arsenic in leg skeletal muscles of three species of wild birds," *Journal of Environmental Science and Health A*, vol. 45, no. 7, pp. 818–823, 2010.
- [11] K. E. Lorber, "Monitoring of heavy metals by energy dispersive X-ray fluorescence spectrometry," *Waste Management and Research*, vol. 4, no. 1, pp. 3–13, 1986.
- [12] F. E. McNeill and J. M. O'Meara, "The in vivo measurement of trace heavy metals by K x-ray fluorescence," *Advances in X-Ray Analysis*, vol. 41, pp. 910–921, 1999.
- [13] L. J. Blum, *Bio- and Chemi-Luminescent Sensors*, World Scientific Publishing Company, Singapore, 1997.
- [14] A. Lobnik, "Absorption-based sensors," in *Optical Chemical Sensors*, F. Baldini, A. N. Chester, J. Homola, and S. Martellucci, Eds., pp. 77–98, Springer, Amsterdam, The Netherlands, 2006.
- [15] S. Nagl and O. S. Wolfbeis, "Classification of optical chemical sensors and biosensors based on fluorescence and phosphorescence," in *Standardization and Quality Assurance in Fluorescence Measurements I*, vol. 5 of *Springer Series on Fluorescence*, pp. 325–346, 2008.
- [16] C. McDonagh, C. S. Burke, and B. D. MacCraith, "Optical chemical sensors," *Chemical Reviews*, vol. 108, no. 2, pp. 400–422, 2008.
- [17] A. Lobnik, I. Oehme, I. Murkovic, and O. S. Wolfbeis, "pH optical sensors based on sol-gels: chemical doping versus covalent immobilization," *Analytica Chimica Acta*, vol. 367, no. 1–3, pp. 159–165, 1998.
- [18] A. Lobnik, M. Turel, Š. Korent Urek, and A. Košak, "Nanostructured materials use in sensors: their benefits and drawbacks," in *Carbon and Oxide Nanostructures*, A. Öchsner, H. Altenbach, and L. F. Martins da Silva, Eds., pp. 307–354, Springer, Berlin, Germany, 2010.
- [19] J. V. Ros-Lis, R. Casasús, M. Comes et al., "A mesoporous 3D hybrid material with dual functionality for Hg<sup>2+</sup> detection and adsorption," *Chemistry*, vol. 14, pp. 8267–8278, 2008.
- [20] S. A. El-Safty, "Organic-inorganic hybrid mesoporous monoliths for selective discrimination and sensitive removal of toxic mercury ions," *Journal of Materials Science*, vol. 44, no. 24, pp. 6764–6774, 2009.
- [21] E. Kim, H. Eun Kim, S. Jin Lee, S. Sung Lee, M. Lyong Seo, and J. Hwa Jung, "Reversible solid optical sensor based on acyclic-type receptor immobilized SBA-15 for the highly selective detection and separation of Hg(II) ion in aqueous media," *Chemical Communications*, no. 33, pp. 3921–3923, 2008.
- [22] P. Zhou, Q. Meng, G. He, H. Wu, C. Duan, and X. Quan, "Highly sensitive fluorescence probe based on functional SBA-15 for selective detection of Hg<sup>2+</sup> in aqueous media," *Journal of Environmental Monitoring*, vol. 11, no. 3, pp. 648–653, 2009.
- [23] C. Song, X. Zhang, C. Jia, P. Zhou, X. Quan, and C. Duan, "Highly sensitive and selective fluorescence sensor based on functional SBA-15 for detection of Hg<sup>2+</sup> in Aqueous Media," *Talanta*, vol. 81, no. 1-2, pp. 643–649, 2010.
- [24] D. Wu, Z. Wang, G. Wu, and W. Huang, "Chemosensory rhodamine-immobilized mesoporous silica material for extracting mercury ion in water with improved sensitivity," *Materials Chemistry and Physics*, vol. 137, no. 1, pp. 428–433, 2012.
- [25] Y. Wang, B. Li, L. Zhang et al., "A highly selective regenerable optical sensor for detection of mercury(II) ion in water using organic-inorganic hybrid nanomaterials containing pyrene," *New Journal of Chemistry*, vol. 34, no. 9, pp. 1946–1953, 2010.
- [26] Z. Jin, X.-B. Zhang, D.-X. Xie et al., "Clicking fluoroionophores onto mesoporous silicas: a universal strategy toward efficient fluorescent surface sensors for metal ions," *Analytical Chemistry*, vol. 82, no. 15, pp. 6343–6346, 2010.
- [27] X. Wang, P. Wang, Z. Dong et al., "Highly sensitive fluorescence probe based on functional SBA-15 for selective detection of Hg<sup>2+</sup>," *Nanoscale Research Letters*, vol. 5, no. 9, pp. 1468–1473, 2010.
- [28] Z. Dong, X. Tian, Y. Chen, J. Hou, and J. Ma, "Rhodamine group modified SBA-15 fluorescent sensor for highly selective detection of Hg<sup>2+</sup> and its application as an INHIBIT logic device," *RSC Advances*, vol. 3, no. 7, pp. 2227–2233, 2013.
- [29] N. Zhang, G. Li, Z. Cheng, and X. Zuo, "Rhodamine B immobilized on hollow Au-HMS material for naked-eye detection of Hg<sup>2+</sup> in aqueous media," *Journal of Hazardous Materials*, vol. 229–230, pp. 401–410, 2012.

- [30] X. Guo, B. Li, L. Zhang, and Y. Wang, "Highly selective fluorescent chemosensor for detecting Hg(II) in water based on pyrene functionalized coreshell structured mesoporous silica," *Journal of Luminescence*, vol. 132, no. 7, pp. 1729–1734, 2012.
- [31] N.-B. Zhang, J.-J. Xu, and C.-G. Xue, "Core-shell structured mesoporous silica nanoparticles equipped with pyrene-based chemosensor: synthesis, characterization, and sensing activity towards Hg(II)," *Journal of Luminescence*, vol. 131, no. 9, pp. 2021–2025, 2011.
- [32] G. Sánchez, D. Curiel, I. Ratera, A. Tárraga, J. Veciana, and P. Molina, "Modified mesoporous silica nanoparticles as a reusable, selective chromogenic sensor for mercury(II) recognition," *Dalton Transactions*, vol. 42, no. 18, pp. 6318–6326, 2013.
- [33] D. Zhai, K. Zhang, Y. Zhang et al., "Mesoporous silica equipped with europium-based chemosensor for mercury ion detection: synthesis, characterization, and sensing performance," *Inorganica Chimica Acta*, vol. 387, pp. 396–400, 2012.
- [34] E. Kim, S. Seo, M. L. Seo, and J. H. Jung, "Functionalized monolayers on mesoporous silica and on titania nanoparticles for mercuric sensing," *Analyst*, vol. 135, no. 1, pp. 149–156, 2010.
- [35] Q. Meng, X. Zhang, C. He, G. He, P. Zhou, and C. Duan, "Multifunctional mesoporous silica material used for detection and adsorption of  $\text{Cu}^{2+}$  in aqueous solution and biological applications in vitro and in vivo," *Advanced Functional Materials*, vol. 20, no. 12, pp. 1903–1909, 2010.
- [36] S. A. El-Safty, A. A. Ismail, and A. Shahat, "Optical supermicrosensor responses for simple recognition and sensitive removal of Cu (II) Ion target," *Talanta*, vol. 83, no. 5, pp. 1341–1351, 2011.
- [37] D. Lu, J. Lei, Z. Tian, L. Wang, and J. Zhang, " $\text{Cu}^{2+}$  fluorescent sensor based on mesoporous silica nanosphere," *Dyes and Pigments*, vol. 94, no. 2, pp. 239–246, 2012.
- [38] T. Liu, G. Li, N. Zhang, and Y. Chen, "An inorganic-organic hybrid optical sensor for heavy metal ion detection based on immobilizing 4-(2-pyridylazo)-resorcinol on functionalized HMS," *Journal of Hazardous Materials*, vol. 201–202, pp. 155–161, 2012.
- [39] P. Pal, S. K. Rastogi, C. M. Gibson, D. E. Aston, A. L. Branen, and T. E. Bitterwolf, "Fluorescence sensing of Zinc(II) using ordered mesoporous silica material (MCM-41) functionalized with *N*-(Quinolin-8-yl)-2-[3-(triethoxysilyl)propylamino]acetamide," *ACS Applied Materials and Interfaces*, vol. 3, no. 2, pp. 279–286, 2011.
- [40] D. Lu, L. Yang, Z. Tian, L. Wang, and J. Zhang, "Core-shell mesoporous silica nanospheres used as  $\text{Zn}^{2+}$  ratiometric fluorescent sensor and adsorbent," *RSC Advances*, vol. 2, no. 7, pp. 2783–2789, 2012.
- [41] M. Shahid, P. Srivastava, S. S. Razi, R. Ali, and A. Misra, "Detection of  $\text{Zn}^{2+}$  ion on a reusable fluorescent mesoporous silica beads in aqueous medium," *Journal of Inclusion Phenomena and Macrocyclic Chemistry*, 2012.
- [42] J. Tan, H. F. Wang, and X. P. Yan, "A fluorescent sensor array based on ion imprinted mesoporous silica," *Biosensors and Bioelectronics*, vol. 24, no. 11, pp. 3316–3321, 2009.
- [43] S. A. El-Safty, "Functionalized hexagonal mesoporous silica monoliths with hydrophobic azo-chromophore for enhanced Co(II) ion monitoring," *Adsorption*, vol. 15, no. 3, pp. 227–239, 2009.
- [44] S. A. El-Safty, A. A. Ismail, H. Matsunaga, H. Nanjo, and F. Mizukami, "Uniformly mesocaged cubic *Fd3m* monoliths as modal carriers for optical chemosensors," *Journal of Physical Chemistry C*, vol. 112, no. 13, pp. 4825–4835, 2008.
- [45] Q. Meng, W. Su, X. Hang, X. Li, C. He, and C. Duan, "Dye-functional mesoporous silica material for fluorimetric detection of Cr(III) in aqueous solution and biological imaging in living systems," *Talanta*, vol. 86, no. 1, pp. 408–414, 2011.
- [46] S. A. El-Safty, A. A. Ismail, H. Matsunaga, T. Hanaoka, and F. Mizukami, "Optical nanoscale pool-on-surface design for control sensing recognition of multiple cations," *Advanced Functional Materials*, vol. 18, no. 10, pp. 1485–1500, 2008.
- [47] S. A. El-Safty, D. Prabhakaran, A. A. Ismail, H. Matsunaga, and F. Mizukami, "Three-dimensional wormhole and ordered mesostructures and their applicability as optically ion-sensitive probe templates," *Chemistry of Materials*, vol. 20, no. 8, pp. 2644–2654, 2008.
- [48] J. Wang, S. Chu, F. Kong, L. Luo, Y. Wang, and Z. Zou, "Designing a smart fluorescence chemosensor within the tailored channel of mesoporous material for sensitively monitoring toxic heavy metal ions Pb(II)," *Sensors and Actuators B*, vol. 150, no. 1, pp. 25–35, 2010.
- [49] F. Hoffmann, M. Cornelius, J. Morell, and M. Fröba, "Silica-based mesoporous organic-inorganic hybrid materials," *Angewandte Chemie*, vol. 45, no. 20, pp. 3216–3251, 2006.
- [50] G. J. D. A. A. Soler-Illia, C. Sanchez, B. Lebeau, and J. Patarin, "Chemical strategies to design textured materials: from microporous and mesoporous oxides to nanonetworks and hierarchical structures," *Chemical Reviews*, vol. 102, no. 11, pp. 4093–4138, 2002.
- [51] F. Hoffman and M. Fröba, "Visiting porous inorganic silica networks with organic functions-PMOs and related hybrid materials," *Chemical Society Reviews*, vol. 40, no. 2, pp. 608–620, 2011.
- [52] Y. Wan and D. Zhao, "On the controllable soft-templating approach to mesoporous silicates," *Chemical Reviews*, vol. 107, no. 7, pp. 2821–2860, 2007.
- [53] V. Meynen, P. Cool, and E. F. Vansant, "Verified syntheses of mesoporous materials," *Microporous and Mesoporous Materials*, vol. 125, no. 3, pp. 170–223, 2009.
- [54] J. Y. Ying, C. P. Manhart, and M. S. Wong, "Synthesis and applications of supramolecular-templated mesoporous materials," *Angewandte Chemie*, vol. 38, pp. 56–77, 1999.
- [55] J. D. Epping and B. F. Chmelka, "Nucleation and growth of zeolites and inorganic mesoporous solids: molecular insights from magnetic resonance spectroscopy," *Current Opinion in Colloid and Interface Science*, vol. 11, no. 2–3, pp. 81–117, 2006.
- [56] G. L. Athens, R. M. Shayib, and B. F. Chmelka, "Functionalization of mesostructured inorganic-organic and porous inorganic materials," *Current Opinion in Colloid and Interface Science*, vol. 14, no. 4, pp. 281–292, 2009.
- [57] T. Yanagisawa, T. Shimizu, K. Kuroda, and C. Kato, "The preparation of alkyltrimethylammonium-kanemite complexes and their conversion to microporous materials," *Bulletin of the Chemical Society of Japan*, vol. 63, no. 4, pp. 988–992, 1990.
- [58] B. Wang, Y. Liu, B. Li, S. Yue, and W. Li, "Optical oxygen sensing materials based on trinuclear starburst ruthenium(II) complexes assembled in mesoporous silica," *Journal of Luminescence*, vol. 128, no. 3, pp. 341–347, 2008.
- [59] X. Wu, L. Song, B. Li, and Y. Liu, "Synthesis, characterization, and oxygen sensing properties of Ru(II) complex covalently grafted to mesoporous MCM-41," *Journal of Luminescence*, vol. 130, no. 3, pp. 374–379, 2010.

- [60] Y. Liu, B. Li, Y. Cong, L. Zhang, D. Fan, and L. Shi, "Optical oxygen sensing materials based on a novel dirhenium(I) complex assembled in mesoporous silica," *Journal of Luminescence*, vol. 131, no. 4, pp. 781–785, 2011.
- [61] L. Shi, B. Li, S. Yue, and D. Fan, "Synthesis, photophysical and oxygen-sensing properties of a novel bluish-green emission Cu(I) complex," *Sensors and Actuators B*, vol. 137, no. 1, pp. 386–392, 2009.
- [62] J. Haitao, Y. Huilin, L. Fan, and L. Yang, "Fabrication and performances of an optical sensor system constructed by a novel Cu(I) complex embedded on silica matrix," *Journal of Luminescence*, vol. 132, no. 1, pp. 198–204, 2012.
- [63] Y. C. Chang, H. Bai, S. N. Li, and C. N. Kuo, "Bromocresol green/mesoporous silica adsorbent for ammonia gas sensing via an optical sensing instrument," *Sensors*, vol. 11, no. 4, pp. 4060–4072, 2011.
- [64] J. Zhu, R. Liu, J. Xu, and C. Meng, "Preparation and characterization of mesoporous silicon spheres directly from MCM-48 and their response to ammonia," *Journal of Materials Science*, vol. 46, no. 22, pp. 7223–7227, 2011.
- [65] F. Liu, L.-J. Zhang, J.-H. Xiao, J. Hu, and H.-L. Liu, "A mesoporous silica modified conjugated polymer film: preparation and detection nitroaromatics in aqueous phase," *Frontiers of Materials Science in China*, vol. 4, no. 2, pp. 158–163, 2010.
- [66] D. Li, J. Liu, R. T. Kwok, Z. Liang, B. Z. Tang, and J. Yu, "Super-sensitive detection of explosives by recyclable AIE luminogen-functionalized mesoporous materials," *Chemical Communications*, vol. 48, no. 57, pp. 7167–7169, 2012.
- [67] S. El-Safty and M. A. Sheneshen, "High-order mesoporous (HOM) sensors for visual recognition of toxic metal ions in drinking water," in *Proceedings of the 14th International Meeting on Chemical Sensors (IMCS '12)*, pp. 725–728, Nuremberg, Germany, 2012.
- [68] T. Mayr, S. M. Borisov, T. Abel et al., "Light harvesting as a simple and versatile way to enhance brightness of luminescent sensors," *Analytical Chemistry*, vol. 81, no. 15, pp. 6541–6545, 2009.
- [69] E.-B. Cho, D. O. Volkov, and I. Sokolov, "Ultrabright fluorescent silica mesoporous silica nanoparticles: control of particle size and dye loading," *Advanced Functional Materials*, vol. 21, no. 16, pp. 3129–3135, 2011.
- [70] E.-B. Cho, D. O. Volkov, and I. Sokolov, "Ultrabright fluorescent mesoporous silica nanoparticles," *Small*, vol. 6, no. 20, pp. 2314–2319, 2010.
- [71] M. Comes, M. D. Marcos, R. Martínez-Máñez et al., "Hybrid functionalized silica-polymer composites for enhanced analyte monitoring using optical sensors," *Journal of Materials Chemistry*, vol. 18, pp. 5815–5823, 2008.
- [72] B. J. Melde, B. J. Johnson, and P. T. Charles, "Mesoporous silicate materials in sensing," *Sensors*, vol. 8, no. 8, pp. 5202–5228, 2008.
- [73] W. S. Han, H. Y. Lee, S. H. Jung, S. J. Lee, and J. H. Jung, "Silica-based chromogenic and fluorogenic hybrid chemosensor materials," *Chemical Society Reviews*, vol. 38, no. 7, pp. 1904–1915, 2009.
- [74] J. H. Jung, M. Park, and S. Shinkai, "Fabrication of silica nanotubes by using self-assembled gels and their applications in environmental and biological fields," *Chemical Society Reviews*, vol. 39, no. 11, pp. 4286–4302, 2010.
- [75] T.-H. Tran-Thi, R. Dagnelie, S. Crunaire, and L. Nicole, "Optical chemical sensors based on hybrid organic-inorganic sol-gel nanoreactors," *Chemical Society Reviews*, vol. 40, pp. 621–639, 2011.
- [76] O. S. Wolfbeis, "Materials for fluorescence-based optical chemical sensors," *Journal of Materials Chemistry*, vol. 15, no. 27–28, pp. 2657–2669, 2005.
- [77] J. R. Lakowicz, *Principles of Fluorescence Spectroscopy*, Springer, 2006.
- [78] G. Guilbault, *Practical Fluorescence*, Marcel Dekker, New York, NY, USA, 1990.
- [79] S. G. Schulman, *Molecular Luminescence Spectroscopy, Methods and Applications, Part 2*, John Wiley & Sons, New York, NY, USA, 1988.
- [80] O. S. Wolfbeis, in *Fiber Optic Chemical Sensors and Biosensors*, CRC Press, Boca Raton, Fla, USA, 1991.
- [81] M. Valledor, J. C. Campo, I. Sánchez-Barragán, J. C. Viera, J. M. Costa-Fernández, and A. Sanz-Medel, "Luminescent ratiometric method in the frequency domain with dual phase-shift measurements: application to oxygen sensing," *Sensors and Actuators B*, vol. 117, no. 1, pp. 266–273, 2006.
- [82] S. M. Buck, Y.-E. L. Koo, E. Park et al., "Optochemical nanosensor PEBBLES: photonic explorers for bioanalysis with biologically localized embedding," *Current Opinion in Chemical Biology*, vol. 8, no. 5, pp. 540–546, 2004.
- [83] H. Sun, A. M. Scharff-Poulsen, H. Gu, and K. Almdal, "Synthesis and characterization of ratiometric, pH sensing nanoparticles with covalently attached fluorescent dyes," *Chemistry of Materials*, vol. 18, no. 15, pp. 3381–3384, 2006.
- [84] A. Prasanna de Silva, T. S. Moody, and G. D. Wright, "Fluorescent PET (Photoinduced Electron Transfer) sensors as potent analytical tools," *Analyst*, vol. 134, no. 12, pp. 2385–2393, 2009.
- [85] X. M. Meng, S. X. Wang, and M. Z. Zhu, "Quinoline-based fluorescence sensors," in *Molecular Photochemistry—Various Aspects*, S. Saha, Ed., InTech, Rijeka, Croatia, 2012.
- [86] M. Formica, V. Fusi, L. Giorgi, and M. Micheloni, "New fluorescent chemosensors for metal ions in solution," *Coordination Chemistry Reviews*, vol. 256, no. 1–2, pp. 170–192, 2012.
- [87] Z. Liu, W. He, and Z. Guo, "Metal coordination in photoluminescent sensing," *Chemical Society Reviews*, vol. 42, no. 4, pp. 1568–1600, 2013.
- [88] B. Valeur and I. Leray, "Design principles of fluorescent molecular sensors for cation recognition," *Coordination Chemistry Reviews*, vol. 205, no. 1, pp. 3–40, 2000.
- [89] C. B. Braungardt, E. P. Achterberg, B. Axelsson et al., "Analysis of dissolved metal fractions in coastal waters: an inter-comparison of five voltammetric in situ profiling (VIP) systems," *Marine Chemistry*, vol. 114, no. 1–2, pp. 47–55, 2009.
- [90] I. Oehme and O. S. Wolfbeis, "Optical sensors for determination of heavy metal ions," *Mikrochimica Acta*, vol. 126, no. 3–4, pp. 177–192, 1997.
- [91] H. Zhang, B. Lei, W. Mai, and Y. Liu, "Oxygen-sensing materials based on ruthenium(II) complex covalently assembled mesoporous MSU-3 silica," *Sensors and Actuators B*, vol. 160, no. 1, pp. 677–683, 2011.
- [92] F. Kleitz, S. H. Choi, and R. Ryoo, "Cubic *Ia3d* large mesoporous silica: synthesis and replication to platinum nanowires, carbon nanorods and carbon nanotubes," *Chemical Communications*, vol. 9, no. 17, pp. 2136–2137, 2003.
- [93] X. Liu, B. Tian, T. Yu et al., "Room temperature synthesis in acidic media of large pore three-dimension bicontinuous mesoporous silica with *Ia3d* symmetry," *Angewandte Chemie*, vol. 41, pp. 3876–3878, 2002.
- [94] S. A. El-Safty and T. Hanaoka, "Monolithic nanostructured silicate family templated by lyotropic liquid-crystalline nonionic

- surfactant mesophases,” *Chemistry of Materials*, vol. 15, no. 15, pp. 2892–2902, 2003.
- [95] S. A. El-Safty and T. Hanaokat, “Microemulsion liquid crystal templates for highly ordered three-dimensional mesoporous silica monoliths with controllable mesopore structures,” *Chemistry of Materials*, vol. 16, no. 3, pp. 384–400, 2004.
- [96] S. A. El-Safty, T. Hanaoka, and F. Mizukami, “Large-scale design of cubic  $Ia3d$  mesoporous silica monoliths with high order, controlled pores, and hydrothermal stability,” *Advanced Materials*, vol. 17, pp. 47–53, 2005.
- [97] S. A. El-Safty and J. Evans, “Formation of highly ordered mesoporous silica materials adopting lyotropic liquid crystal mesophases,” *Journal of Materials Chemistry*, vol. 12, no. 1, pp. 117–123, 2002.
- [98] C. Gao, Y. Sakamoto, K. Sakamoto, O. Terasaki, and S. Che, “Synthesis and characterization of mesoporous silica AMS-10 with bicontinuous cubic  $Pn3m$  symmetry,” *Angewandte Chemie*, vol. 45, no. 26, pp. 4295–4298, 2006.
- [99] C. Z. Yu, Y. H. Yu, and D. Y. Zhao, “Highly ordered large caged cubic mesoporous silica structures templated by triblock PEO-PBO-PEO copolymer,” *Chemical Communications*, no. 7, pp. 575–576, 2000.
- [100] Q. Huo, D. I. Margolese, and G. D. Stucky, “Surfactant control of phases in the synthesis of mesoporous silica-based materials,” *Chemistry of Materials*, vol. 8, no. 5, pp. 1147–1160, 1996.
- [101] Q. Huo, D. I. Margolese, U. Ciesla et al., “Generalized synthesis of periodic surfactant/inorganic composite materials,” *Nature*, vol. 368, no. 6469, pp. 317–321, 1994.
- [102] Y. Sakamoto, M. Kaneda, O. Terasaki et al., “Direct imaging of the pores and cages of three-dimensional mesoporous materials,” *Nature*, vol. 408, no. 6811, pp. 449–453, 2000.
- [103] J. Fan, C. Z. Yu, F. Gao et al., “Cubic mesoporous silica with large controllable entrance sizes and advanced adsorption properties,” *Angewandte Chemie*, vol. 42, no. 27, pp. 3146–3150, 2003.
- [104] F. Kleitz, D. Liu, G. M. Anilkumar et al., “Large cage face-centered-cubic  $Fm3m$  mesoporous silica: synthesis and structure,” *Journal of Physical Chemistry B*, vol. 107, no. 51, pp. 14296–14300, 2003.
- [105] J. R. Matos, M. M. Kruk, L. P. Mercuri et al., “Ordered mesoporous silica with large cage-like pores: structural identification and pore connectivity design by controlling the synthesis temperature and time,” *Journal of the American Chemical Society*, vol. 125, no. 3, pp. 821–829, 2003.
- [106] S. D. Shen, Y. Q. Li, Z. D. Zhang et al., “A novel ordered cubic mesoporous silica templated with tri-head group quaternary ammonium surfactant,” *Chemical Communications*, no. 19, pp. 2212–2213, 2002.
- [107] S. Che, Z. Liu, T. Ohsuna, K. Sakamoto, O. Terasaki, and T. Tatsumi, “Synthesis and characterization of chiral mesoporous silica,” *Nature*, vol. 429, no. 6989, pp. 281–284, 2004.
- [108] C. T. Kresge, M. E. Leonowicz, W. J. Roth, J. C. Vartuli, and J. S. Beck, “Ordered mesoporous molecular sieves synthesized by a liquid-crystal template mechanism,” *Nature*, vol. 359, no. 6397, pp. 710–712, 1992.
- [109] Directive 2008/32/EC of the European Parliament and of the Council of 11 March 2008 amending Directive 2000/60/EC establishing a framework for Community action in the field of water policy, as regards the implementing powers conferred on the Commission, pp. 60–61, 2008.
- [110] D. G. Barceloux, “Copper,” *Journal of Toxicology*, vol. 37, no. 2, pp. 217–230, 1999.
- [111] M. Cieślak-Golonka, “Toxic and mutagenic effects of chromium(VI). A review,” *Polyhedron*, vol. 15, no. 21, pp. 3667–3689, 1996.

## Research Article

# Optical Property Characterization of Novel Graphene-X (X=Ag, Au and Cu) Nanoparticle Hybrids

Sumit Ranjan Sahu,<sup>1</sup> Mayanglambam Manolata Devi,<sup>1</sup> Puspall Mukherjee,<sup>2</sup> Pratik Sen,<sup>2</sup> and Krishanu Biswas<sup>1</sup>

<sup>1</sup> Department of Materials Science and Engineering, Indian Institute of Technology Kanpur, Kanpur 208016, India

<sup>2</sup> Department of Chemistry, Indian Institute of Technology Kanpur, Kanpur 208016, India

Correspondence should be addressed to Krishanu Biswas; kbiswas@iitk.ac.in

Received 6 August 2013; Accepted 29 September 2013

Academic Editor: Pathik Kumbhakar

Copyright © 2013 Sumit Ranjan Sahu et al. This is an open access article distributed under the Creative Commons Attribution License, which permits unrestricted use, distribution, and reproduction in any medium, provided the original work is properly cited.

The present investigation reports new results on optical properties of graphene-metal nanocomposites. These composites were prepared by a solution-based chemical approach. Graphene has been prepared by thermal reduction of graphene oxide (GO) at 90°C by hydrazine hydrate in an ammoniacal medium. This ammoniacal solution acts as a solvent as well as a basic medium where agglomeration of graphene can be prevented. This graphene solution has further been used for functionalization with Ag, Au, and Cu nanoparticles (NPs). The samples were characterized by X-ray diffraction (XRD), Raman spectroscopy, UV-Vis spectroscopy, scanning electron microscopy (SEM), and transmission electron microscopy (TEM) to reveal the nature and type of interaction of metal nanoparticles with graphene. The results indicate distinct shift of graphene bands both in Raman and UV-Vis spectroscopies due to the presence of the metal nanoparticles. Raman spectroscopic analysis indicates blue shift of D and G bands in Raman spectra of graphene due to the presence of metal nanoparticles except for the G band of Cu-G, which undergoes red shift, reflecting the charge transfer interaction between graphene sheets and metal nanoparticles. UV-Vis spectroscopic analysis also indicates blue shift of graphene absorption peak in the hybrids. The plasmon peak position undergoes blue shift in Ag-G, whereas red shift is observed in Au-G and Cu-G.

## 1. Introduction

Graphene is a unique allotrope of carbon characterized by honeycomb lattice of sp<sup>2</sup>-hybridized carbon atoms in which carbon atoms are packed in a two-dimensional (2D) hexagonal lattice [1]. Graphene, often considered as a “miracle material” of the 21st century, has attracted tremendous attention in the academic community [2]. Being one-atomic layer thick sheet of carbon extending infinitely in 2D, its properties encompass range of superlattices. This includes high value of Young’s modulus (~1100 GPa) [3], fracture strength (125 GPa) [3], thermal conductivity (~5000 W/mK) [4], mobility of charge carriers ( $2 \times 10^5$  cm<sup>2</sup>/Vs) [5], and specific surface area 2630 (m<sup>2</sup>/g) [6]. Owing to its excellent physical and chemical properties, graphene is considered as a potential candidate for large number of applications in many technological fields such as nanoelectronics [7], composites [8], energy storage

devices [6], efficient lasers, photodetectors, and biomedical applications [9].

Preparation of high quality graphene is needed to study the unique properties for applications. A number of different ways of preparing graphene have been reported in the literature [10]. This includes micromechanical exfoliation of graphite [11], chemical vapor deposition [12], and chemical methods to create colloidal suspension [13]. The micromechanical method is time consuming, and the yield is low and thus limits our ability to have significant economic and technological impact [11]. On the other hand, graphene is prepared via solution chemistry involving oxidation of graphite to prepare layered graphene oxide sheets (GOS), which can further be reduced to obtain graphene sheets (GS). GS can be considered as chemically modified sheets having controllable electronic properties. However, unless these sheets are well separated from each other, the graphene sheets tend to form

agglomerates or even restack to form graphite due to Van der Waals interaction [14, 15]. Thus, the addition of any dispersoid which can bind tightly onto graphene sheets is of utmost necessity to achieve better dispersion of graphene sheets. In this context, decoration of graphene with metal nanoparticle becomes very important. Very recently, integration of graphene and metal nanoparticle to prepare new generation of hybrid nanomaterials has aroused extensive interest for large number of potential applications like chemical sensors, energy storage and catalysis, as well as hydrogen storage [16–21]. Most notably, noble metal nanoparticles (NP) have widely been used as a catalyst to promote various chemical reactions [22]. Catalyst support is found to be an important aspect affecting the catalytic activity of the catalyst [23]. To enhance the catalytic activity, graphene-metal nanoparticle hybrid composite can be used due to its very high specific surface area.

In the light of recent studies carried out by different groups on decoration of NPs with graphene to prepare hybrid structure, we consider that it is important to investigate the influence of metal nanoparticles on the electronic structure of graphene. For this purpose, we have synthesized gold (Au-G), silver (Ag-G), and copper nanoparticle decorated-graphene (Cu-G) via chemical synthesis. Almost all the previous works had generally dealt with synthesis of such hybrid structure [24, 25]. The nature of interaction between graphene and NPs is not properly studied. In this work, we have employed both Raman and UV-Vis spectroscopic techniques to obtain optical properties of the nanomaterials, and thereby electronic structures of the materials are brought about.

## 2. Experimental Procedure

**2.1. Materials.** Graphite powder (100 mesh, 99.9995%), silver nitrate ( $\text{AgNO}_3$ , 99.9%), hydrogen tetrachloroaurate (III) hydrate ( $\text{HAuCl}_4$ , 99.9%), copper sulfate ( $\text{CuSO}_4$ , 99.9%) (Alfa Aesar, India), sodium nitrate ( $\text{NaNO}_3$ ), potassium permanganate ( $\text{KMnO}_4$ ), concentrated sulfuric acid ( $\text{H}_2\text{SO}_4$ ), ammonia solution ( $\text{NH}_4\text{OH}$ ), hydrazine hydrate solution ( $\text{H}_2\text{NNH}_2 \cdot \text{H}_2\text{O}$ ) and hydrogen peroxide ( $\text{H}_2\text{O}_2$ ) (Sigma Aldrich, India), Trisodiumcitrate dehydrate ( $\text{C}_6\text{H}_5\text{Na}_3\text{O}_7 \cdot \text{H}_2\text{O}$ ), Dextrose ( $\text{C}_6\text{H}_{12}\text{O}_6$ ), and Sodium hydroxide ( $\text{NaOH}$ ) (Merck Millipore, India) were used for the preparation of graphene and nanocomposites. All the chemicals were used in the condition as received without further purification. The water used in all the experiments was purified through a Millipore system.

**2.2. Preparation of Graphite Oxide.** Graphite oxide was prepared by modified Hummers method [26] by taking 2 g of natural graphite powder in a 250 mL beaker placed in an ice bath, maintaining the temperature at  $20^\circ\text{C}$ . Subsequently, 1 g of  $\text{NaNO}_3$ , 46 mL of  $\text{H}_2\text{SO}_4$ , and 6 g of  $\text{KMnO}_4$  were added slowly to the graphite powder and kept under stirring for 15 min. After that, the ice bath was removed, and the solution was heated at  $35^\circ\text{C}$  for 30 min. Then, 92 mL of distilled water was added slowly into the solution and stirred

for further 30 min. Finally, 80 mL of hot distilled water was added, followed by the addition of 30%  $\text{H}_2\text{O}_2$  aqueous solution until the bubbling disappeared and the colour of the solution turned to deep yellow. The residue was collected after centrifugation, and warm water was utilized for subsequent washing to make it neutral ( $\text{pH} = 7$ ). The resulting powder was redispersed into distilled water by ultrasonication for 30 min. The solution was freeze dried to get the desired brown coloured graphite oxide powder.

**2.3. Exfoliation and Reduction of Graphene Oxide (GO).** The exfoliated GO was prepared by ultrasonating 0.01 g of the synthesized graphite oxide powder in 100 mL of distilled water in a 250 mL round-bottom flask for 2 h. The pH of the so obtained yellow brown suspension of GO was adjusted to the value of 10 by dropwise addition of  $315 \mu\text{L}$  of 25% ammonia solution into it. For reduction of GO,  $35 \mu\text{L}$  of hydrazine hydrate was added slowly, and the whole suspension was refluxed in an oil bath at  $90^\circ\text{C}$  for 2 h while stirring. Finally, black coloured precipitate of graphene (G) obtained after centrifugation was redispersed in distilled water and kept as a stock solution for the synthesis of Ag-G, Au-G, and Cu-G.

**2.4. Preparation of Ag-G, Au-G, and Cu-G.** The synthesis of Ag-G has been carried out according to the method described by Mao et al. [27]. Equal volume (20 mL) of graphene stock solution and silver nitrate aqueous solution (0.001 M) were slowly mixed in a 250 mL round-bottom flask. The whole solution was heated to  $90^\circ\text{C}$  with subsequent addition of 2 mL sodium citrate (w/v 1%) aqueous solution into it while stirring for 15 min to complete the reaction. After cooling down to room temperature, the solution was centrifuged many times with ethanol and water until the undesired by-products are removed, and the precipitate was redispersed in distilled water. Au-G was also prepared in similar fashion by mixing equal volume (20 mL) of graphene solution and  $\text{HAuCl}_4$  aqueous solution (0.001 M) followed by the addition of 2 mL of 38.8 mM sodium citrate aqueous solution. Cu-G was prepared by the following method. 2.4 g of dextrose was dissolved in 30 mL of water.  $60 \mu\text{L}$  of 1.0 M NaOH solution and 1 mL of graphene stock solution were added to it. The whole mixture was heated to  $80^\circ\text{C}$  under stirring in argon atmosphere. 1.2 mL of copper sulfate aqueous solution (0.01 M) was added to it. After five minutes of constant stirring at  $80^\circ\text{C}$ , Cu-G was obtained.

## 3. Characterizations

X-ray diffraction (XRD) of all the powder samples were recorded by a Bruker D8 focus X-ray diffractometer with  $\text{Cu K}_\alpha$  radiation ( $\lambda = 0.154056 \text{ nm}$ ) operating at 40 KV and 20 mA. To investigate structural change during chemical processing, the Raman spectra were recorded with a WITec GmbH alpha 300 R Raman spectrometer in the back-scattering mode using an Ar-ion laser (514.5 nm) as an excitation source. The UV-Visible absorption spectra of aqueous solutions of GO, G, Ag-G, Au-G, and Cu-G were recorded in the range between 200 and 800 nm using

a Jasco V-670 UV-Vis spectrophotometer. Scanning electron microscopic (SEM) and Transmission electron microscopic (TEM) micrographs of G, Ag-G, Au-G, and Cu-G were taken with a Carl Zeiss EVO 50 VP scanning electron microscope and FEI Tecnai G<sup>2</sup> U-twin 200 KV instrument, respectively, to observe the nanoscale microstructure.

## 4. Results and Discussions

In the following, we shall describe the results obtained during present investigation and discuss the results in the light of the available literature.

### 4.1. Structural Characterization

**4.1.1. X-Ray Diffraction (XRD).** X-ray diffraction patterns of graphene oxide (GO), graphene (G), and graphene silver (Ag-G) nanoparticles hybrid materials are presented in Figure 1. XRD pattern of GO shows a sharp diffraction peak at  $2\theta = 14.03^\circ$  corresponding to (001) of GO. The XRD pattern of G shows two distinct peaks at  $2\theta = 24^\circ$  and  $44.8^\circ$ , which are attributed to (002) and (100) reflections of graphene nanosheets. The calculated d-spacing of graphene using broad peak is 0.364 nm. The broadness of the peak signifies decrease in the crystallinity of graphene upon reduction from GO. On the other hand, XRD pattern of Ag-G reveals the peaks due to (111), (200), (220), and (311) of Ag nanocrystals as well as broad peak (002) due to graphene. Similar observation has been made for Au-G and Cu-G nanohybrids. No peaks corresponding to oxides of Ag, Au, or Cu are observed within the detectable limit of XRD. The peaks due to metal nanocrystals are broad, indicating nanocrystalline size and strain due to incorporation within graphene nanosheet. The position of (002) peak of graphene does not change for different metal hybrids. Using the peak position of graphene, the calculated d-spacing of Ag-G is 0.370 nm, whereas  $d_{002}$  of graphite is 0.335 nm. The broadness of the peak is the indication of the presence of graphene nanosheets with varying d-spacing values.

**4.1.2. Scanning (SEM) and Transmission Electron (TEM) Microscopic Observation.** The detailed microstructural characterization of graphene and graphene-metal nanoparticle hybrids has been carried out using SEM and TEM. Figure 2(a) shows high resolution SEM micrograph of graphene and reveals crumpled and scrolled morphology of graphene sheets. Thin sheet of graphene crumpled into different layers is clearly visible in the Figure 2(a). Figures 2(b), 2(c), and 2(d) are the SEM images of graphene-metal hybrids, that is, Ag-G, Au-G, and Cu-G. The figure shows that the metal nanoparticles appear as discrete bright dots, which are homogeneously distributed on the surface of the graphene sheets. The graphene and graphene-metal nanoparticle hybrids are characterized directly under SEM without coating by gold film, suggesting their conductive nature. The detailed morphology and structure of the graphene-metal nanoparticle hybrids have been characterized by TEM. It is to be noted that TEM samples were prepared by dropping the sonicated dispersion

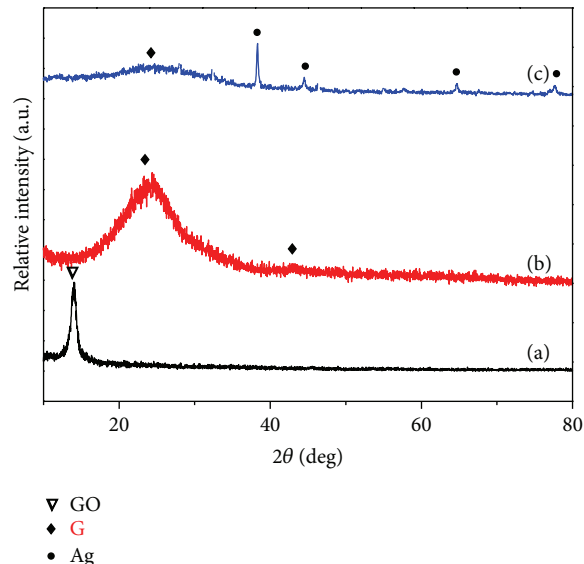


FIGURE 1: XRD patterns of (a) GO (b) G, and (c) Ag-G.

of sample in ultrapure methanol onto 600 mesh copper grids coated with lacy carbon and dried at room temperature for 3 hours. As observed in Figure 3(a), graphene nanosheets are randomly compact and stacked, revealing uniform laminar morphology such as crumpled silk veil waves. The selected area diffraction pattern (SADP) obtained from such nanosheets is shown as inset in Figure 3(a). The SADP reveals two diffraction rings, which can be indexed using (100) and (002) of graphene. Therefore, the formation of graphene by the reduction of graphene oxide is confirmed from the SADP pattern. Figures 3(b), 3(c), and 3(d) reveal graphene-metal nanoparticles hybrid composite with Ag, Au, and Cu used as nanoparticles to decorate the graphene nanosheets. Figure 3(b) shows scrolled morphology of graphene sheets with distributed Ag nanoparticles, embedded within the graphene sheets. The multiple stacking of graphene consisting of uniformly distributed Ag nanoparticles with average size of  $25 \pm 5$  nm is distinctly observed. The histogram (as shown in the bottom inset) corroborates the narrow size distribution with maximum number of particles around 25 nm along with few larger particles of about 30 nm. The SADP obtained from the hybrid nanocomposite is shown as inset in Figure 3(b). The sharp diffraction rings can be indexed as those of Ag, while diffraction rings corresponding to (100) and (002) of graphene can also be deciphered. Figure 3(c) shows the results of the TEM investigation on graphene-Au hybrid prepared by chemical synthesis as outlined in Section 2.4. The bright field micrograph (Figure 3(c)) shows uniform distribution of Au nanocrystals (appeared as dark dots) in the crumpled nanosheets of graphene. It is clearly visible that highly dispersed Au nanoparticles may provide large available surface area and enhance activities towards different reactions. The distribution of Au nanoparticles embedded in the graphene is shown as bottom inset of Figure 3(c). The average size of the particle is  $8 \pm 4$  nm. The histogram indicates broad size distribution. The SADP pattern obtained from the hybrid is shown as upper inset of Figure 3(c). It

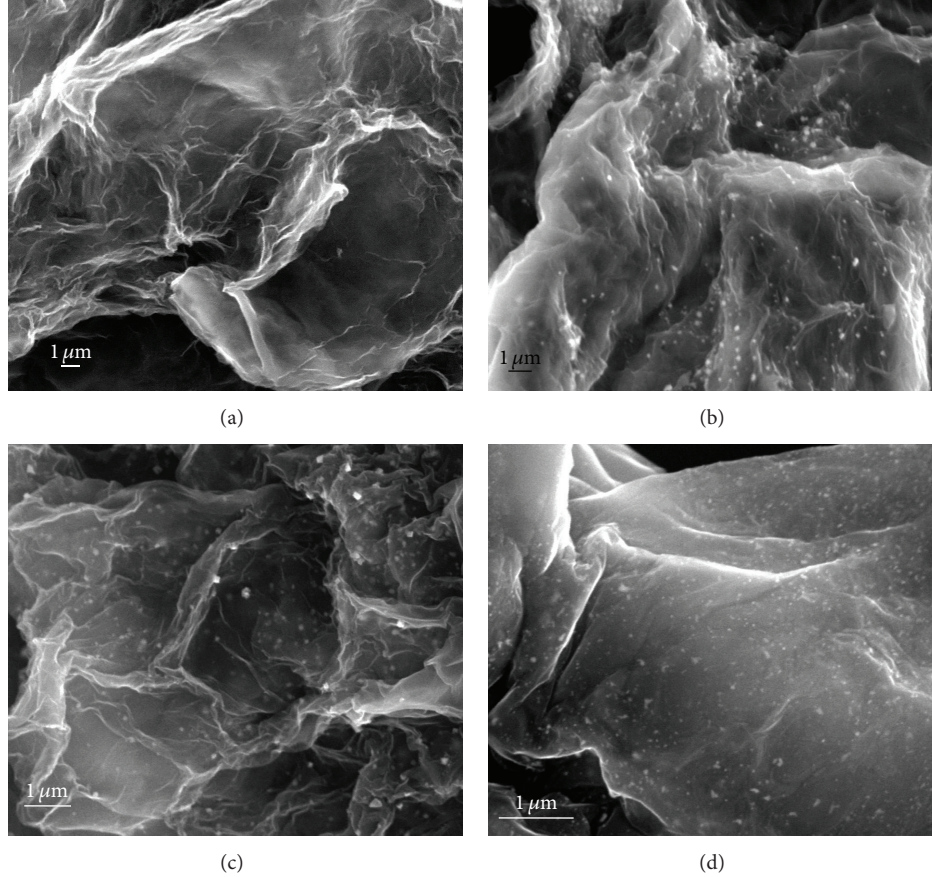


FIGURE 2: SEM image of (a) G, (b) Ag-G, (c) Au-G, and (d) Cu-G.

clearly reveals the diffraction rings corresponding to Au along with diffraction rings due to graphene. Figure 3(d) shows the bright field micrograph of graphene-Cu nanoparticle hybrid, revealing uniform distribution of Cu nanoparticle within the graphene sheets. The SADP pattern, as shown in the inset of the figure, confirms the presence of Cu. The detailed particle size analysis indicates that the average particle size is  $6 \pm 3$  nm.

**4.2. Optical Property Characterization.** In the following, we shall describe and discuss the results obtained during optical property characterization of the graphene as well as graphene-metal nanoparticle hybrids. The optical properties of the graphene and hybrids are obtained using Raman and UV-Vis spectroscopy. From the earlier section, it is clear that the hybrids contain uniform distribution of Ag, Au, and Cu nanoparticles embedded in the graphene matrix. Therefore, it is worth to look into the optical properties of these hybrids. The discussion will be done by comparing the optical properties of monolithic graphene sheets with the hybrids.

**4.2.1. Raman Spectroscopy.** Figure 4(a) shows the Raman spectra of GO and graphene. The spectra reveal the presence of characteristics D (defect) and G (graphite) bands, 2D band, and (D + G) band. It is to be noted that D band arises due

to in-plane stretching of  $sp^2$ -bonded carbon atoms in the hexagonal lattice, whereas G band is due to small graphitic domains because of vibrations of  $sp^3$ -bonded carbon atoms [28]. The 2D band originates due to second order two phonon process. Table 1 shows the detailed value of different bands in GO and graphene. For GO, D band is located at  $1346 \text{ cm}^{-1}$ , whereas G and 2D bands are located at  $1590 \text{ cm}^{-1}$  and  $2697 \text{ cm}^{-1}$ , respectively. The reduction of GO to graphene shows significant red shift in position of G ( $1579 \text{ cm}^{-1}$ ), D band ( $1340 \text{ cm}^{-1}$ ), and 2D band ( $2677 \text{ cm}^{-1}$ ) (Figure 4(a)). The red shift of G band in graphene is mainly due to the restoration of conjugated double bonds and the increase in the number of  $sp^2$ -bonded carbon atoms in the graphene during the reduction of GO. Table 1 also reports the ratio of the intensities of D and G bands ( $I_D/I_G$ ) in GO (1.01) and graphene (1.09). It is to be noted that the ratio ( $I_D/I_G$ ) is a measure of disordered carbon and normally expresses ( $sp^2/sp^3$ ) carbon ratio [29]. It can be observed that  $I_D/I_G$  value increases from GO to graphene. The increase in the value indicates the relative increase of  $sp^2$  domains and decrease of average crystallite size [30]. The ratio is found to be inversely proportional to the crystallite size ( $L_a$ ):

$$L_a = (2.4 \times 10^{-10}) \lambda_{\text{laser}}^4 \left( \frac{I_D}{I_G} \right)^{-1}. \quad (1)$$

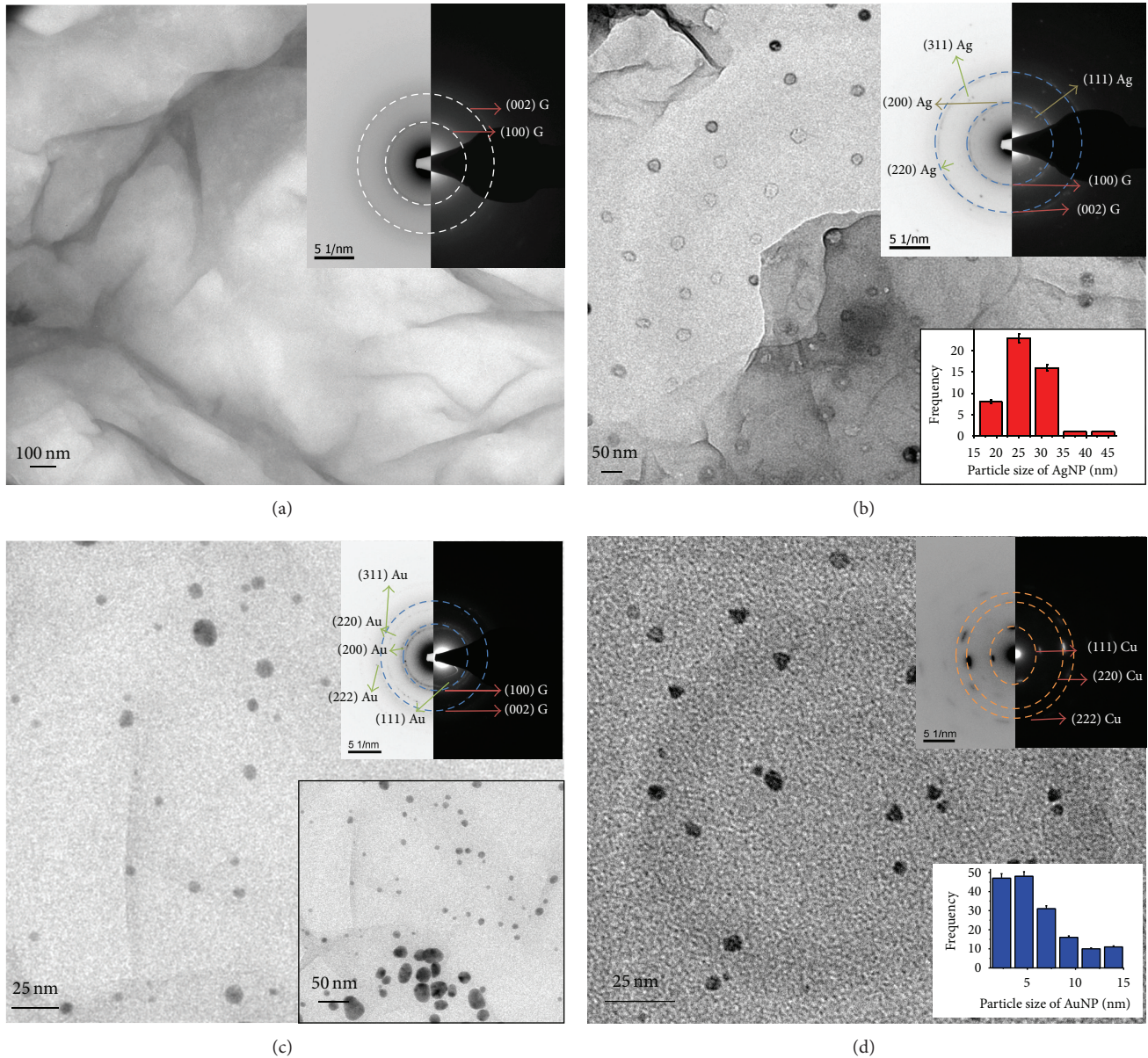


FIGURE 3: TEM micrographs and corresponding SAED patterns of (a) G, (b) Ag-G, (c) Au-G, and (d) Cu-G. The upper inset in each figure shows SAD pattern, whereas lower inset in figure (b) and (d) shows nanoparticle size distribution and in figure (c) shows low magnification bright field micrograph, revealing graphene sheets decorated with nanoparticles.

Using  $\lambda_{\text{laser}} = 514.5 \text{ nm}$ , the calculated crystallite size of graphene is 18 nm.

Let us now discuss the case of graphene-metal nanoparticle hybrids. Figure 4(b) reveals Raman spectra of Ag-G, Au-G, and Cu-G hybrids. Table 1 shows detailed results of the positions of different vibrational bands as well as  $I_D/I_G$  values. The nature of the peaks of different bands, that is, D, G, 2D, and D + G bands, remains almost the same as that of monolithic graphene.

As indicated, G band is usually assigned to  $E_{2g}$  phonons of  $sp^2$ -bonded carbon atoms, whereas D band is assigned to breathing mode of k-phonon of  $A_{1g}$  symmetry. The position of G band does not change (Table 1) after the incorporation

of metal nanoparticles. However, nature of shift is distinctly different in case of Cu-G as compared to Ag-G and Au-G. In case of Cu-G, the G band has undergone slight red shift ( $1578 \text{ cm}^{-1}$ ) as compared to graphene ( $1579 \text{ cm}^{-1}$ ). This indicates that the vibrational nature of small graphitic domain ( $sp^3$ -bonded carbon) has not been affected much by the presence of the metal nanoparticles. On the other hand, the position of D band in the hybrids has undergone blue shift as compared to graphene. The major shift has occurred in case of Cu-G ( $1351 \text{ cm}^{-1}$ ) indicating that the vibrational energy due to in-plane stretching of  $sp^2$ -bonded carbon is increased due to incorporation of metal nanoparticles. We believe that this is due to occupation of Cu atoms in specific position in

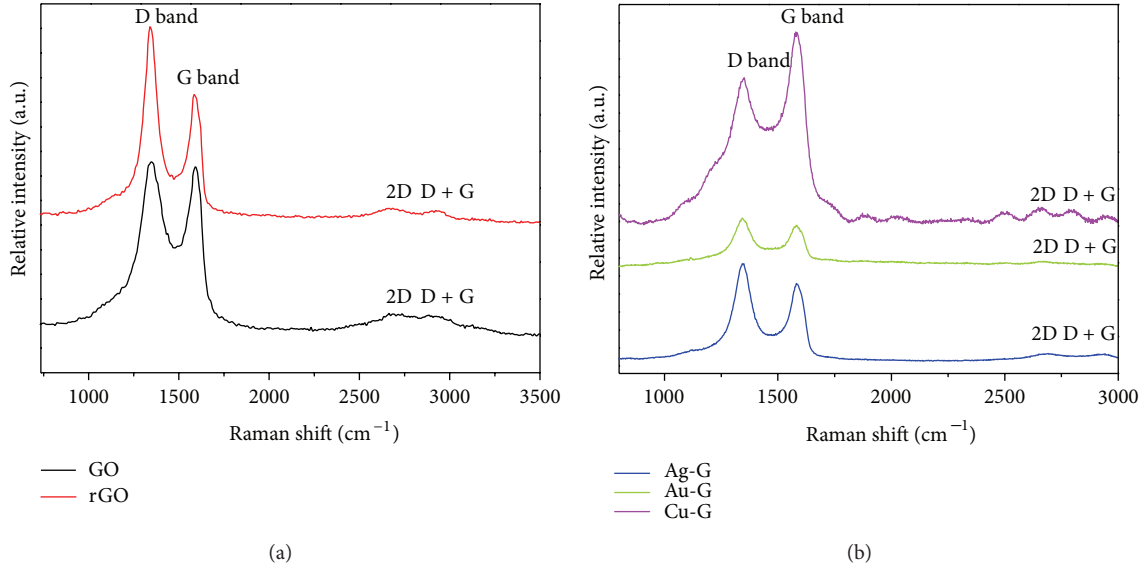


FIGURE 4: Raman spectra of (a) GO and G (b) Ag-G, Au-G, and Cu-G.

TABLE 1: Comparison of D, G, 2D, and (D + G) band positions and  $I_D/I_G$  value of GO, G, Ag-G Au-G, and Cu-G.

Material	D band	G band	2D band	D + G band	$I_D/I_G$ value
Graphene oxide (GO)	1346 $\text{cm}^{-1}$	1590 $\text{cm}^{-1}$	2687 $\text{cm}^{-1}$	2919 $\text{cm}^{-1}$	1.01
Graphene (G)	1340 $\text{cm}^{-1}$	1579 $\text{cm}^{-1}$	2677 $\text{cm}^{-1}$	2912 $\text{cm}^{-1}$	1.09
Silver decorated graphene (Ag-G)	1346 $\text{cm}^{-1}$	1581 $\text{cm}^{-1}$	2690 $\text{cm}^{-1}$	2934 $\text{cm}^{-1}$	1.12
Gold decorated graphene (Au-G)	1342 $\text{cm}^{-1}$	1581 $\text{cm}^{-1}$	2667 $\text{cm}^{-1}$	2924 $\text{cm}^{-1}$	1.05
Copper decorated graphene (Cu-G)	1351 $\text{cm}^{-1}$	1578 $\text{cm}^{-1}$	2660 $\text{cm}^{-1}$	2949 $\text{cm}^{-1}$	0.89

the graphene structure, that is, in the hexagonal cage. These shifts in the position of G band may also be related to the position of nanoparticles that occupy the sites on the surface of graphene. As Cu has smaller atomic radius as compared to Ag and Au, we believe that Cu atoms may occupy the hexagonal cage of graphene, while Ag and Au occupy other adsorption sites T, (top on carbon atom) or B (bridge between two carbons). On the other hand, the shift in the position of D band is significantly larger in case of Cu-G as compared to that of Ag-G and Au-G. This may be due to larger distortion generated by occupation of Cu atoms in hexagonal cage of graphene than that generated by occupation of Ag and Au atoms on T or B site. Another important parameter characterizing the Raman spectra of hybrid is  $I_D/I_G$  ratio. This ratio has been found to increase from 1.09 to 1.12 in case of Ag-G, whereas it decreases in case of Au-G (1.05) and 0.89. The enhancement in the ratio indicates decrease in the site of in-plane  $sp^2$  domain and partially ordered crystal structure of graphene nanosheets (GNs). On the other hand, the significant decrease in  $I_D/I_G$  ratio for Cu-G indicates that the new graphitic domains are more in number but smaller in size, formed upon reduction of GO to Cu-G.

Another important parameter of Raman spectroscopy is full width at half maxima (FWHM) of the D and G bands. Table 2 shows the results of GO, G, and graphene-metal nanoparticle hybrids. It is clearly observed that FWHM decreases substantially for Cu-G, whereas it does not change

TABLE 2: Comparison of FWHM of D and G band of GO, G, Ag-G, Au-G, and Cu-G.

Material	FWHM (D band)	FWHM (G band)
Graphene oxide (GO)	106 $\text{cm}^{-1}$	64 $\text{cm}^{-1}$
Graphene (G)	80 $\text{cm}^{-1}$	38 $\text{cm}^{-1}$
Silver decorated graphene (Ag-G)	81 $\text{cm}^{-1}$	67 $\text{cm}^{-1}$
Gold decorated graphene (Au-G)	78 $\text{cm}^{-1}$	63 $\text{cm}^{-1}$
Copper decorated graphene (Cu-G)	74 $\text{cm}^{-1}$	73 $\text{cm}^{-1}$

much for Au-G and Ag-G. On the other hand, FWHM of G band increases substantially for hybrids as compared to graphene. The most notable increase occurs in case of Cu-G. As the size of Cu NPs is smaller than Ag NPs and Au NPs, the local structural defect on the crystallite domains of graphene formed due to incorporation of Cu nanoparticles is lesser than those due to Ag and Au nanoparticles. The crystallite domain size of graphene calculated by using (1) for the Ag-G, Au-G, and Cu-G has been found to be 18 nm, 19 nm, and 22 nm, respectively. Therefore, as the crystallite size increases from Ag to Au to Cu, the FWHM value for D band shows decreasing trend.

**4.2.2. UV-Vis Spectroscopy.** Another important optical characterization tool for graphene and graphene-related hybrids

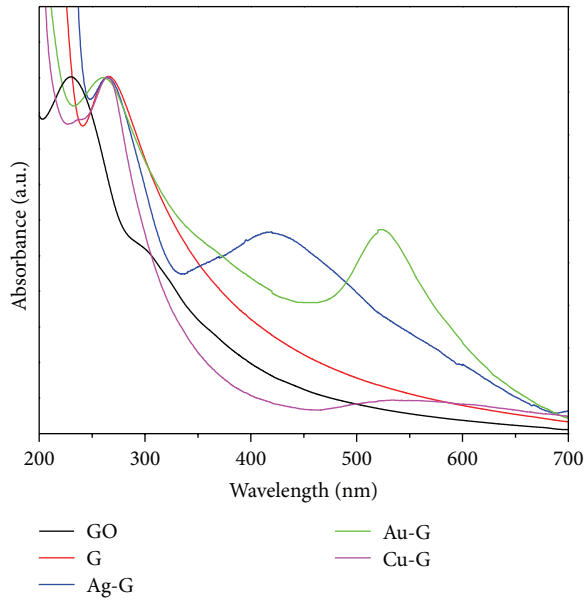


FIGURE 5: UV-Vis spectra of GO, G, Au-G, Ag-G, and Cu-G.

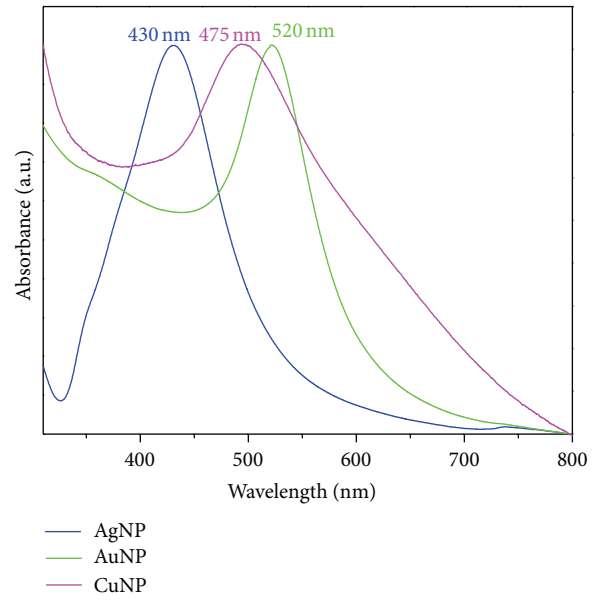


FIGURE 6: UV-Vis spectra of AgNP, AuNP, and CuNP.

is UV-Vis spectroscopy. Figures 5 and 6 summarize the UV-Vis spectroscopic observations in the present investigation. Detailed results are summarized in Table 3. Figure 5 reveals UV-Vis absorption spectra of graphene oxide (GO), graphene (G), graphene-metal nanoparticle hybrids, Ag-G, Au-G, and Cu-G. For GO, two characteristic peaks are observed in UV-Vis spectrum, a maximum at 230 nm, due to  $\pi \rightarrow \pi^*$  transition of aromatic C-C bond and a shoulder at 303 nm, from  $n \rightarrow \pi^*$  transition of C=O bond [31]. The original electronic conjugation is restored during reduction of GO to G by hydrazine hydrate, and a characteristic absorption peak of G has been observed at 266 nm, whereas the shoulder at 303 nm disappears. The incorporation of Ag NPs, in the G framework (Ag-G) is confirmed by the presence of absorption peak at 420 nm, which is considered to be due to surface plasmon resonance of Ag NPs. The bare Ag NPs derived from the reduction of  $\text{Ag}^+$  by hydrazine hydrate under same condition is characterized by an absorption peak at 430 nm, which is consistent with previous studies [32, 33]. Clearly the incorporation of Ag NPs onto the stable aqueous graphene dispersion leads to blue shift of the surface plasmon resonance characteristics. It also has been observed that the absorption peak position of graphene for Ag-G hybrids changes to 260 nm, a blue shift of 6 nm as compared to aqueous graphene dispersion. The blue shift can be the result of charge transfer interaction between graphene and Ag NPs and has been confirmed by enhancement of Raman signals (Figure 4(b)). Similar measurements have been carried out for Au-G and Cu-G hybrids. The absorption peak of graphene in the Au-G is also blue shifted, by 4 nm. Therefore, charge transfer interaction between graphene and Au is poor as compared to Ag-G. The similar observation has been made for absorption peak of graphene in case of Cu-G. Table 3 also reveals that the surface plasmon resonance of Cu NPs is affected strongly by graphene nanosheets as plasmon resonance has red shifted by 65 nm. On the other hand, the

TABLE 3: Comparison of UV-Vis absorption peak position of GO, G, AgNPs, Ag-G, AuNPs, Au-G, CuNPs, and Cu-G.

Material	Graphene peak position	Plasmon peak position
Graphene oxide (GO)	230 nm ( $\pi \rightarrow \pi^*$ ) 303 nm ( $n \rightarrow \pi^*$ )	—
Graphene (G)	266 nm	—
Pure silver nanoparticles (AgNP)	—	430 nm
Silver decorated graphene (Ag-G)	260 nm	420 nm
Pure gold nanoparticles (AuNP)	—	520 nm
Gold decorated graphene (Au-G)	264 nm	524 nm
Pure copper nanoparticles (CuNP)	—	475 nm
Copper decorated graphene (Cu-G)	264 nm	540 nm

surface plasmon resonance of Au NPs has undergone red shift only by 4 nm as compared to free Au NPs. Therefore, the behavior of metal NPs can be modified extensively by incorporating them into the graphene nanosheets. Obviously these interactions depend on the position of these NPs, where they occupy the hexagonal graphene framework. This will be investigated further.

## 5. Summary

The present investigation has categorically shown that it is possible to synthesize graphene-metal nanoparticle hybrids in aqueous media by chemical rule. The following conclusion can be drawn from the study.

- Fine nanoparticles (Ag, Au, and Cu) decorated graphene can be prepared by chemical synthesis. The size of the nanoparticles varies from 5 to 35 nm.

- (b) The G and D bands can be modified more extensively by Cu than Ag or Au.
- (c) The surface plasmon resonance of the metal nanoparticles can be altered by incorporation of nanoparticles in the graphene nanosheets.
- (d) The electronic interaction between the metal nanoparticle and graphene depends on the type of metal as well as size of the atom.

## Acknowledgments

This work was supported by research funding from Department of Science and Technology (DST), the Government of India. The authors would like to acknowledge the usage of Electron Microscopy facility (SEM, TEM), XRD facility Raman Spectroscopy facility, FTIR facility, and UV-Vis spectroscopy facility at IIT Kanpur. The authors would like to thank Indian National Science Academy for funding for making the paper as open access.

## References

- [1] A. K. Geim and K. S. Novoselov, "The rise of graphene," *Nature Materials*, vol. 6, no. 3, pp. 183–191, 2007.
- [2] X. Huang, Z. Yin, S. Wu et al., "Graphene-based materials: synthesis, characterization, properties, and applications," *Small*, vol. 7, no. 14, pp. 1876–1902, 2011.
- [3] C. Lee, X. Wei, J. W. Kysar, and J. Hone, "Measurement of the elastic properties and intrinsic strength of monolayer graphene," *Science*, vol. 321, no. 5887, pp. 385–388, 2008.
- [4] A. A. Balandin, S. Ghosh, W. Bao et al., "Superior thermal conductivity of single-layer graphene," *Nano Letters*, vol. 8, no. 3, pp. 902–907, 2008.
- [5] K. I. Bolotin, K. J. Sikes, Z. Jiang et al., "Ultrahigh electron mobility in suspended graphene," *Solid State Communications*, vol. 146, no. 9–10, pp. 351–355, 2008.
- [6] M. D. Stoller, S. Park, Z. Yanwu, J. An, and R. S. Ruoff, "Graphene-based ultracapacitors," *Nano Letters*, vol. 8, no. 10, pp. 3498–3502, 2008.
- [7] D. A. Areshkin and C. T. White, "Building blocks for integrated graphene circuits," *Nano Letters*, vol. 7, no. 11, pp. 3253–3259, 2007.
- [8] U. Khan, P. May, A. O'Neill, and J. N. Coleman, "Development of stiff, strong, yet tough composites by the addition of solvent exfoliated graphene to polyurethane," *Carbon*, vol. 48, no. 14, pp. 4035–4041, 2010.
- [9] J. Y. Liu and R. H. Hurt, "Ion release kinetics and particle persistence in aqueous nano-silver colloids," *Environmental Science and Technology*, vol. 44, no. 6, pp. 2169–2175, 2010.
- [10] M. Pumera, "Graphene-based nanomaterials and their electrochemistry," *Chemical Society Reviews*, vol. 39, no. 11, pp. 4146–4157, 2010.
- [11] X. Lu, M. Yu, H. Huang, and R. S. Ruoff, "Tailoring graphite with the goal of achieving single sheets," *Nanotechnology*, vol. 10, no. 3, pp. 269–272, 1999.
- [12] M. Eizenberg and J. M. Blakely, "Carbon monolayer phase condensation on Ni(111)," *Surface Science*, vol. 82, no. 1, pp. 228–236, 1979.
- [13] S. Stankovich, D. A. Dikin, R. D. Piner et al., "Synthesis of graphene-based nanosheets via chemical reduction of exfoliated graphite oxide," *Carbon*, vol. 45, no. 7, pp. 1558–1565, 2007.
- [14] S. Niyogi, E. Bekyarova, M. E. Itkis, J. L. McWilliams, M. A. Hamon, and R. C. Haddon, "Solution properties of graphite and graphene," *Journal of the American Chemical Society*, vol. 128, no. 24, pp. 7720–7721, 2006.
- [15] L.-X. Li, B.-G. An, H. Nishihara et al., "Water-dispersible "carbon nanotubes" with controllable graphene layer orientation," *Chemical Communications*, no. 30, pp. 4554–4556, 2009.
- [16] Y.-K. Kim, H.-K. Na, and D.-H. Min, "Influence of surface functionalization on the growth of gold nanostructures on graphene thin films," *Langmuir*, vol. 26, no. 16, pp. 13065–13070, 2010.
- [17] K. Jasuja and V. Berry, "Implantation and growth of dendritic gold nanostructures on graphene derivatives: electrical property tailoring and Raman enhancement," *ACS Nano*, vol. 3, no. 8, pp. 2358–2366, 2009.
- [18] J. Li and C.-Y. Liu, "Ag/Graphene heterostructures: synthesis, characterization and optical properties," *European Journal of Inorganic Chemistry*, no. 8, pp. 1244–1248, 2010.
- [19] N. Tian, Z.-Y. Zhou, S.-G. Sun, Y. Ding, and L. W. Zhong, "Synthesis of tetrahedral platinum nanocrystals with high-index facets and high electro-oxidation activity," *Science*, vol. 316, no. 5825, pp. 732–735, 2007.
- [20] B. Lim, M. Jiang, P. H. C. Camargo et al., "Pd-Pt bimetallic nanodendrites with high activity for oxygen reduction," *Science*, vol. 324, no. 5932, pp. 1302–1305, 2009.
- [21] S. Chu, L. Hu, X. Hu, M. Yang, and J. Deng, "Titanium-embedded graphene as high-capacity hydrogen-storage media," *International Journal of Hydrogen Energy*, vol. 36, no. 19, pp. 12324–12328, 2011.
- [22] D. Astruc, F. Lu, and J. R. Aranzas, "Nanoparticles as recyclable catalysts: the frontier between homogeneous and heterogeneous catalysis," *Angewandte Chemie—International Edition*, vol. 44, no. 48, pp. 7852–7872, 2005.
- [23] A. Y. Stakheev and L. M. Kustov, "Effects of the support on the morphology and electronic properties of supported metal clusters: modern concepts and progress in 1990s," *Applied Catalysis A*, vol. 188, no. 1–2, pp. 3–35, 1999.
- [24] W. Yuana, Y. Gao, and L. Li, "Green synthesis of graphene/Ag nanocomposites," *Applied Surface Science*, vol. 261, pp. 753–758, 2012.
- [25] K. S. Subrahmanyam, A. K. Manna, S. K. Pati, and C. N. R. Rao, "A study of graphene decorated with metal nanoparticles," *Chemical Physics Letters*, vol. 497, no. 1–3, pp. 70–75, 2010.
- [26] W. S. Hummers Jr. and R. E. Offeman, "Preparation of graphitic oxide," *Journal of the American Chemical Society*, vol. 80, no. 6, p. 1339, 1958.
- [27] A. Mao, D. Zhang, X. Jin et al., "Synthesis of graphene oxide sheets decorated by silver nanoparticles in organic phase and their catalytic activity," *Journal of Physics and Chemistry of Solids*, vol. 73, pp. 982–986, 2012.
- [28] H.-S. Zhang and K. Komvopoulos, "Direct-current cathodic vacuum arc system with magnetic-field mechanism for plasma stabilization," *Review of Scientific Instruments*, vol. 79, no. 7, Article ID 073905, 2008.
- [29] A. C. Ferrari and J. Robertson, "Interpretation of Raman spectra of disordered and amorphous carbon," *Physical Review B*, vol. 61, no. 20, pp. 14095–14107, 2000.

- [30] F. Tuinstra and J. L. Koenig, "Raman spectrum of graphite," *Journal of Chemical Physics*, vol. 53, no. 3, pp. 1126–1130, 1970.
- [31] N. Tian, Z.-Y. Zhou, S.-G. Sun, Y. Ding, and L. W. Zhong, "Synthesis of tetrahedral platinum nanocrystals with high-index facets and high electro-oxidation activity," *Science*, vol. 316, no. 5825, pp. 732–735, 2007.
- [32] I. A. Wani, S. Khatoun, A. Ganguly, J. Ahmed, A. K. Ganguli, and T. Ahmad, "Silver nanoparticles: Large scale solvothermal synthesis and optical properties," *Materials Research Bulletin*, vol. 45, no. 8, pp. 1033–1038, 2010.
- [33] I. Pastoriza-Santos and L. M. Liz-Marzán, "Reduction of silver nanoparticles in DMF. Formation of monolayers and stable colloids," *Pure and Applied Chemistry*, vol. 72, no. 1-2, pp. 83–90, 2000.

## Research Article

# Green Light Emission of $\text{Zn}_x\text{Cd}_{1-x}\text{Se}$ Nanocrystals Synthesized by One-Pot Method

Shu-Ru Chung,<sup>1</sup> Kuan-Wen Wang,<sup>2</sup> and Hong-Shuo Chen<sup>1,2</sup>

<sup>1</sup> Graduate Institute of Materials Science and Green Energy Engineering, National Formosa University, Yunlin 63201, Taiwan

<sup>2</sup> Institute of Materials Science and Engineering, National Central University, Taoyuan 32001, Taiwan

Correspondence should be addressed to Shu-Ru Chung; [srchung@nfu.edu.tw](mailto:srchung@nfu.edu.tw)

Received 9 May 2013; Accepted 1 October 2013

Academic Editor: Pathik Kumbhakar

Copyright © 2013 Shu-Ru Chung et al. This is an open access article distributed under the Creative Commons Attribution License, which permits unrestricted use, distribution, and reproduction in any medium, provided the original work is properly cited.

We present a facile one-pot synthesis to prepare ternary  $\text{Zn}_x\text{Cd}_{1-x}\text{Se}$  ( $x = 0.2, 0.5, 0.8, \text{ and } 1$ ) nanocrystals (NCs) with high emission quantum yield (QY, 45~89%). The effect of Zn content ( $x$ ) of  $\text{Zn}_x\text{Cd}_{1-x}\text{Se}$  NCs on their physical properties is investigated. The NCs have a particle size of 3.2 nm and face centered cubic structure. However, the actual compositions of the NCs are  $\text{Zn}_{0.03}\text{Cd}_{0.97}\text{Se}$ ,  $\text{Zn}_{0.11}\text{Cd}_{0.89}\text{Se}$ , and  $\text{Zn}_{0.38}\text{Cd}_{0.62}\text{Se}$  when Zn content is 0.2, 0.5, and 0.8, respectively. In terms of the optical properties, the emission wavelength shifts from 512 to 545 nm with increasing Zn content from 0 to 0.8 while the QY changes from 89 to 45, respectively. Partial replacement of Cd by Zn is beneficial to improve the QY of  $\text{Zn}_{0.2}$  and  $\text{Zn}_{0.5}$  NCs. The optical properties of ternary NCs are affected by compositional effect rather than particle size effect.

## 1. Introduction

IIB-VIA group semiconductors with energy gaps covering the visible spectral range are suitable candidates for optoelectronic devices. Semiconductor nanocrystals (NCs), also known as quantum dots (QDs), have been widely investigated in the last decade due to their unique chemical and physical properties [1, 2]. Their particle sizes are in the nanometer range (less than 10 nm in diameter) and have very unusual properties. The continued interests in semiconductor NCs can be attributed to the size-dependent optical and electronic properties displayed by these quantum-confined materials. The small size of these compounds results in the three-dimensional confinement of the bulk charge carriers and the corresponding transformation of the bulk energy bands into discrete molecular energy states. This bulk-to-molecule transition is continuous, so that the band gap of the nanocrystalline material can be tuned to a desired energy by controlling the particle size [1, 2]. Besides, for the NCs with sizes of several nanometers, the huge surface energy is noted because most of the atoms are located on the surface. Therefore, surface modification is used in order

to increase the quantum efficiency of photoluminescence. Hence, a proper handling of the surface is essential to obtain highly luminescent NCs. The adjustable and sharp emission characteristics of these materials make them viable candidates for light emitting diodes (LEDs) [3–6], laser [7, 8], biological labels [9–11], and solar cells [12, 13].

In those applications especially for LEDs and bioimages, the luminous efficiency (or quantum yield, QY) of NCs is one of the most important demands. The QY is defined as the ratio of the number of photons emitted to the number of photons absorbed. Hence, how to improve the QY of NCs is the critical task. The QY of NCs can be improved by the following four ways. (1) Remove the lattice defect by heat treatment under high temperature in order to decrease the probability of trapped electron [14]. (2) Passivate the particle surface by bonding with an organic molecule and to improve the surface stability of NCs by reducing the lone pairs [15]. (3) Modify the surface by inorganic molecules (called core-shell structure) for the sake of increasing the electron-hole recombination efficiency [16, 17]. (4) Form alloyed NCs so as to eliminate the lattice mismatch and stress on the core-shell structures [9, 12].

Much work has been published regarding the optical property of NCs with core-shell structure, and the luminous efficiency of NCs can be enhanced significantly [18–20]. However, these processes are time consuming, and the particle size of NCs increases slightly, resulting in a red shift of emission wavelength. On the other hand, the ternary alloyed systems such as  $Zn_xCd_{1-x}Se$  [9, 21, 22],  $CdSe_xTe_{1-x}$  [10],  $Zn_xCd_{1-x}S$  [12],  $CdS_xTe_{1-x}$  [23], and  $CdS_xSe_{1-x}$  [24] are obtained by a two-step route; that is, the alloyed NCs are formed by a core-shell structure through an annealing process. Therefore, two-step route also has the same disadvantage compared to that of core-shell NCs. Moreover, ternary  $Zn_xCd_{1-x}S$  and  $Zn_xCd_{1-x}Se$  NCs can be also synthesized by using a low temperature molecular precursor approach [25]. Therefore, the current focus on the synthesis of semiconductor NCs is to develop efficient routes for the synthesis of high quality and monodispersed NCs materials.

Because of the interesting optical properties of ternary NCs which can be controlled without changing the particle size, a large number of experiments have been performed on developing a fast procedure to produce high quality NCs in the range of visible light [9, 10, 12, 21–24]. However, little attention has been devoted to the one-step route and high emission QY of green light, as well as the role of Zn atom during synthesis. The highly luminescent ternary NCs, in particular of green emission, are potential ideal materials for white LED and QD lasers, which could solve problems occurring in the promising, but highly strained and time-consuming, CdSe/ZnSe core-shell structure. As we have mentioned above, the most important application of NCs is the white LED, but the QY of green light NCs is quite low [26]. Therefore, the aims of this report are to develop an effective one-pot synthetic strategy to make a series of high-quality ternary  $Zn_xCd_{1-x}Se$  NCs with green light emission and to explore the Zn effect on the physical property of the prepared ternary NCs.

## 2. Experimental

**2.1. Chemicals.** Cadmium oxide (CdO, 99.998%) was purchased from Alfa Aesar. Zinc oxide (ZnO, 99.99%), stearic acid (SA, 99%), selenium powder (Se, 99.999%), trioctylphosphine (TOP, 90%), hexadecylamine (HDA, 90%), and trioctylphosphine oxide (TOPO, 90%) were obtained from Aldrich. Hexane (99.7%) and methanol (99%) were provided by Mallinckrodt Chemicals. All chemicals were used as received without further purification.

**2.2. Preparation of  $Zn_xCd_{1-x}Se$  NCs.** Most details of the synthetic and characterizing methods were similar to the ones reported previously [27–30]. Ternary  $Zn_xCd_{1-x}Se$  NCs were prepared by controlling Zn content and named  $Zn_x$  ( $x = 0, 0.2, 0.5, 0.8, \text{ and } 1$ ). A typical synthesis is as follows. Total amount of 0.3 mmol of CdO and ZnO was mixed with 2.4 mmol of SA, which was used as a complex reagent, in a three-necked flask and then heated to 230°C under argon until a clear solution was formed to prepare the cadmium/zinc-SA precursors. After CdO and ZnO were

completely dissolved, the mixture was allowed to cool to room temperature, and a white solid precipitate was obtained. After cadmium/zinc-SA precursor was formed, the mixture surfactants, TOPO and HDA, 5.82 g of each, were added into three-necked flask and stirred together under Ar at room temperature, and the mixture was heated to 320°C under Ar flow to form an optically clear solution. At this temperature, the Se solution containing 1.5 mmol of Se dissolved in 0.9 mL of TOP and 2.1 mL of hexane was swiftly injected into the reaction flask. The reaction time was about 1 s, and the mixed solution was swiftly cooled down to stop reaction. Samples were precipitated with hot anhydrous methanol for purification process. The precipitate was dissolved in hexane for further measurement.

**2.3. Characterization.** The optical properties of samples were measured by fluorescence spectrophotometer (FL, Hitachi F-7000) and UV-vis spectrometer (UV-vis, Jasco V-670 spectrometer), respectively. Relative QYs of samples were determined by comparing the area under the curve of FL emission for the  $Zn_xCd_{1-x}Se$  NCs with that of fluorescent dye (Rhodamine 6G in methanol). X-ray diffraction (XRD) patterns were recorded by a MacScience Co. Ltd. MO3X-HF22 powder diffractometer with  $Cu K\alpha$  ( $\lambda = 1.542 \text{ \AA}$ ) as the incident radiation. Transmission electron microscope (TEM, JEOL JEM-2010) was used to analyze the morphologies and size distribution of samples. The compositions of ternary NCs were conducted by inductively-coupled plasma atomic emission spectrometry (ICP-AES).

## 3. Results and Discussion

**3.1. Optical Properties.** Figure 1 displays the UV-vis and FL spectra of ternary  $Zn_xCd_{1-x}Se$  NCs. Based on Figure 1(a), the band edge absorption and emission wavelength of CdSe with  $Cd/Se = 1/5$  is 502 and 512 nm, respectively. The inset picture shows that the CdSe NCs have the green light with QY of 58%. Compared with the literature [30], it is interesting to mention that a high QY of CdSe with green light can be prepared within a very short period of time (1 s) in this study. Besides, the FL and UV-vis absorption spectra are extremely sharp with a full width of half maximum (FWHM) about 25 nm and the Stokes shift about 10 nm. Moreover, the emission peak with high symmetry and small FWHM implies that the size distribution of CdSe NCs is uniform. The nucleation occurs immediately as TOPSe is injected into the reaction flask, which can be observed from the changes of solution color. The smaller CdSe NCs with stronger quantum confinement effect are produced owing to higher nucleation rate, and this also makes them have high QYs. The results also indicate that to form a SA-Cd complex is quite important for boosting the nucleation rate of CdSe NCs. It has been reported that primary amines show the most promising results for achieving high FL efficiency for a variety of semiconductor NCs [19, 31, 32], and the function of SA is proven to be helpful for the formation of large-sized CdSe [33]. In addition, the quantum confinement effect decreases for NCs with larger particle sizes, resulting in lower

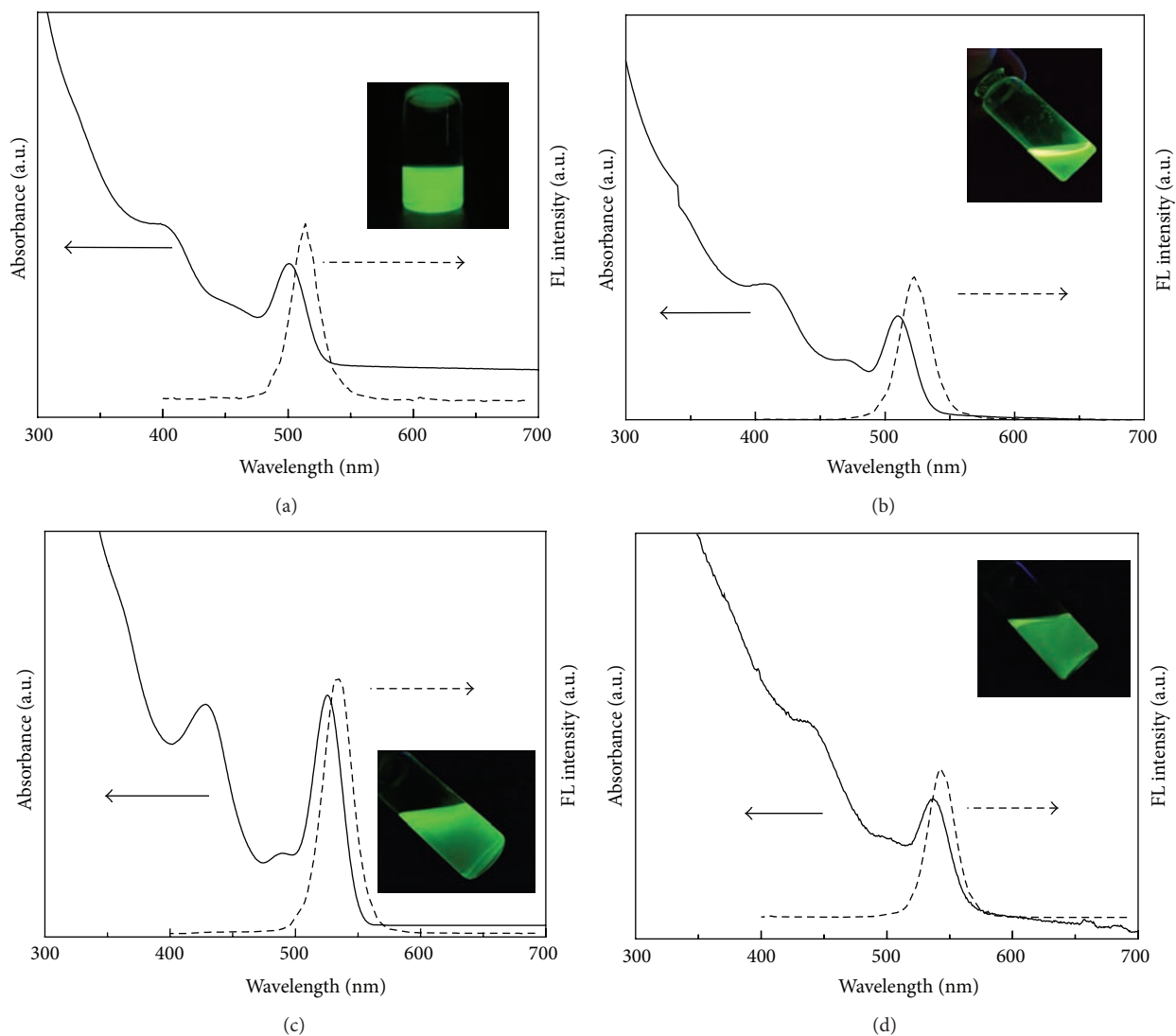


FIGURE 1: Fluorescence and UV-vis spectra of samples. (a)  $Zn_0$ , (b)  $Zn_{0.2}$ , (c)  $Zn_{0.5}$ , and (d)  $Zn_{0.8}$ . Excitation wavelength is 365 nm.

QY. Therefore, prevention of NCs from grain growth during the process is quite important. In our study, primary amine and steric phosphine oxide are used, and Cd-SA complex is preferentially formed to prepare CdSe NCs in a short time. Therefore, CdSe NCs with high QY can be obtained owing to the well-passivated surface of CdSe by those organic ligands and the stronger quantum confinement effect.

On the other hand, according to Figures 1(b), 1(c), and 1(d), the band edge absorption and emission wavelength are 510 and 523 nm, 525 and 534 nm, and 536 and 545 nm for the Zn content increases from 0.2, 0.5 to 0.8, respectively. Moreover, the Stokes shift and the FWHM of those samples is smaller than 13 and 28 nm, respectively. The inset pictures also show that the  $Zn_xCd_{1-x}$ Se NCs have the green light with QY ranging from 89 to 45%. Those results reveal that those samples have a narrow size distribution, a pure green color emission, and a nonlinear optical property. The QY of  $Zn_{0.2}$  and  $Zn_{0.5}$  NCs is 89 and 81% higher than CdSe NCs, while it is only 45% for  $Zn_{0.8}$ . Our results demonstrate that QY

is improved when compared with the samples prepared by previously reported methods [9, 21, 22]. Specifically, a high QY can be achieved by a facile one-pot synthesis. Based on Figure 1, only one emission peak with narrow FWHM can be observed for all samples, implying that either pure CdSe or ternary  $Zn_xCd_{1-x}$ Se NCs are formed. If ZnSe and CdSe nucleated separately, the corresponding FL and absorption peaks should appear. The band gap of ZnSe and CdSe is about 2.8 eV (443 nm) and 1.74 eV (713 nm), respectively. If ZnSe NCs are formed, the emission wavelengths will be less than 443 nm due to the quantum confinement effect. However, we cannot observe the emission peak around or less than 443 nm. This indicates that the ZnSe is formed but with very low QY or the ZnSe is not formed. Because the band gap energy is higher for ZnSe, meaning that it cannot emit green light. Hence, the formation of ZnSe NCs can be ruled out. Although the group II cations diffuse much easier than the group VI anions in II-VI semiconductors [34], the bond strength between Cd and Se is higher than that between Zn

TABLE 1: Physical properties of as-prepared samples.

Theoretical composition	Emission wavelength (nm)	Particle size <sup>a</sup> (nm)	QY (%)	Actual composition <sup>b</sup>
Zn <sub>0</sub>	512	3.1 ± 0.32	58	—
Zn <sub>0.2</sub>	523	3.1 ± 0.27	89	Zn <sub>0.03</sub>
Zn <sub>0.5</sub>	534	3.2 ± 0.31	81	Zn <sub>0.11</sub>
Zn <sub>0.8</sub>	545	3.3 ± 0.28	45	Zn <sub>0.38</sub>
Zn <sub>1</sub>	—	—	—	—

<sup>a</sup>TEM characterization.

<sup>b</sup>ICP-AES characterization.

and Se, implying that CdSe NCs are much easier to form. In order to confirm the stoichiometric ratio of Cd and Zn, the mole fraction of Cd and Zn in the resulting NCs is determined by ICP method. From the ICP results (shown in Table 1), the actual composition of Zn<sub>0.2</sub>, Zn<sub>0.5</sub>, and Zn<sub>0.8</sub> is Zn<sub>0.03</sub>, Zn<sub>0.11</sub>, and Zn<sub>0.38</sub>, respectively, meaning that ternary alloyed Zn<sub>x</sub>Cd<sub>1-x</sub>Se NCs can be prepared successfully under high Zn concentration by one-pot alloying route. For Zn<sub>0.2</sub> sample, Cd is partially replaced by Zn through a doping process. The QY of ternary NCs is higher than that of CdSe when increasing the Zn content from 0.2 to 0.5. When Zn content increases to 0.8, the QY decreases dramatically, implying that even the concentration of Cd is reduced; Zn<sub>x</sub>Cd<sub>1-x</sub>Se NCs with high QY can also be prepared. Qu and Peng [30] mentioned that for the CdSe with an initial Cd/Se of 1/10, its PL QY is higher up to 80%, which is consistent with our results. Based on ICP results we find that the molar fraction of Zn in Zn<sub>x</sub>Cd<sub>1-x</sub>Se NCs is higher for high Zn content sample, so the lower QY of Zn<sub>0.8</sub> sample may be caused by the formation of ZnSe phase. The actual composition of Zn<sub>0.2</sub> sample is Zn<sub>0.03</sub> with QY of 89%, suggesting that when the CdSe is the main phase, the ratio of Cd/Se as well as QY is high [30]. On the other hand, the lower fraction of ZnSe phase is noted for Zn<sub>0.5</sub> sample, and the covalent bond strength can be increased by partially replacing Cd with Zn, resulting in higher QY of ternary NCs.

Figure 2 shows the FL spectra of ternary Zn<sub>x</sub>Cd<sub>1-x</sub>Se NCs with reaction time of 1 s. The emission wavelength of Zn<sub>x</sub>Cd<sub>1-x</sub>Se NCs shifts obviously from 512 to 545 nm when increasing the amount of Zn from 0 to 0.8. When Zn content is 1 (ZnSe), no emission wavelength can be observed, meaning that ZnSe cannot be prepared or the ZnSe NCs are with QY nearly zero under this condition. The observed systematic composition-controlled shift of the emission maximum to longer wavelength is explicable by the formation of Zn<sub>x</sub>Cd<sub>1-x</sub>Se ternary NCs via intermixing wider band gap ZnSe with the narrower band gap CdSe NCs, rather than forming separate CdSe and ZnSe NCs or core-shell structure CdSe/ZnSe, because the emission wavelength of ternary Zn<sub>x</sub>Cd<sub>1-x</sub>Se ( $x = 0.2$  to  $0.8$ ) NCs is located between that of CdSe and ZnSe. Since the band gap of CdSe and ZnSe is 1.74 and 2.8 eV, respectively, it is implied that the ternary Zn<sub>x</sub>Cd<sub>1-x</sub>Se shows a nonlinear optical property, which may be caused by the compositional or particle size effect.

**3.2. Morphology and Structure Analysis.** In order to understand the effect of composition and particle size on emission

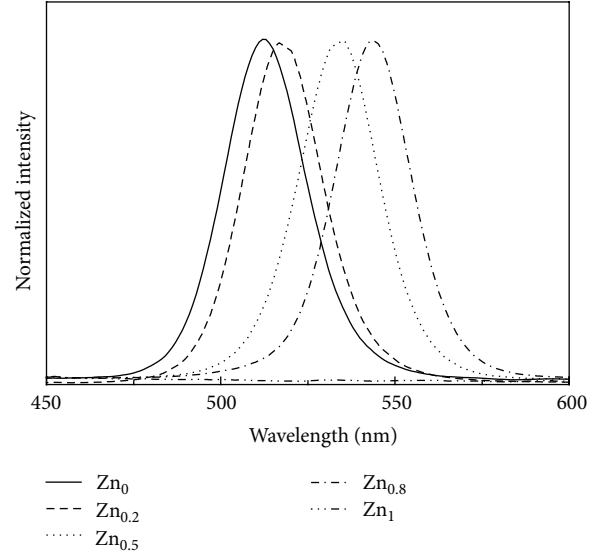


FIGURE 2: FL spectra of samples react for 1 s.

property of NCs, the TEM technique is used. The TEM micrographs of ternary Zn<sub>x</sub>Cd<sub>1-x</sub>Se NCs are shown in Figure 3. The particle size for all samples is almost the same, which is about 3.1, 3.1, 3.2, and 3.3 nm for CdSe, Zn<sub>0.2</sub>, Zn<sub>0.5</sub>, and Zn<sub>0.8</sub>, respectively, suggesting that the nonlinear optical property of ternary Zn<sub>x</sub>Cd<sub>1-x</sub>Se NCs is caused by the compositional instead of particle size effect. Bailey and Nie mentioned that the relation of the anion-cation bonding to their equilibrium positions leads to local structural disordering and a particularly large band gap reduction in CdSeTe-type semiconductor alloys [10], resulting in a nonlinear optical phenomenon. In our study, we believe that a similar mechanism is found in Zn<sub>x</sub>Cd<sub>1-x</sub>Se-type semiconductor alloys when the Zn content is not high enough.

The results of emission wavelengths, particle sizes, QYs, and actual compositions of ternary Zn<sub>x</sub>Cd<sub>1-x</sub>Se NCs are listed in Table 1. A large red shift of Zn<sub>x</sub>Cd<sub>1-x</sub>Se NC is observed with increasing the Zn molar fractions from 0 to 0.38 (emission wavelength is between 512 and 545 nm), and the particle size is almost the same. Zhong et al. mentioned that a large blue shift of Zn<sub>x</sub>Cd<sub>1-x</sub>Se NC is observed with increasing the Zn molar fractions from 0 to 0.67 (emission wavelength is between 615 and 500 nm), and the particle size also increases from 5.2 to 7.5 nm. The optical properties of Zn<sub>x</sub>Cd<sub>1-x</sub>Se NCs with linear optical property and high

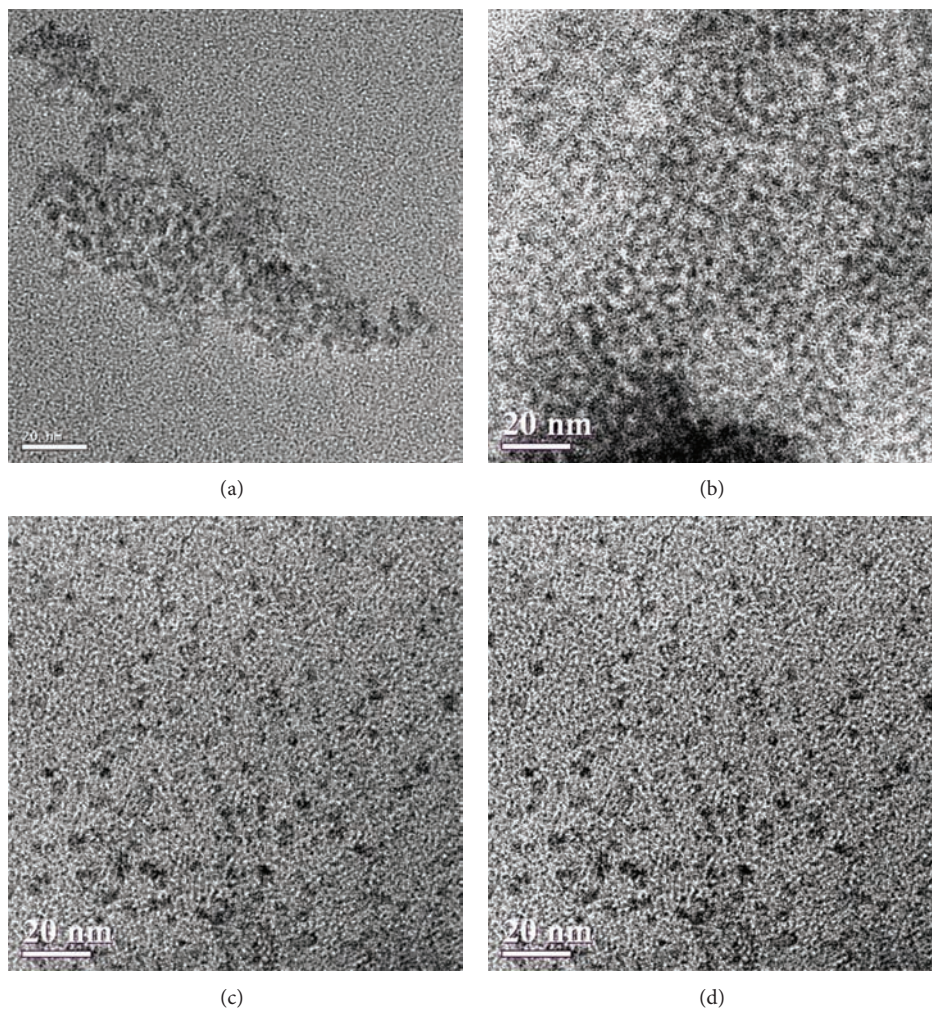


FIGURE 3: TEM images of samples. (a) Zn<sub>0</sub>, (b) Zn<sub>0.2</sub>, (c) Zn<sub>0.5</sub>, and (d) Zn<sub>0.8</sub>.

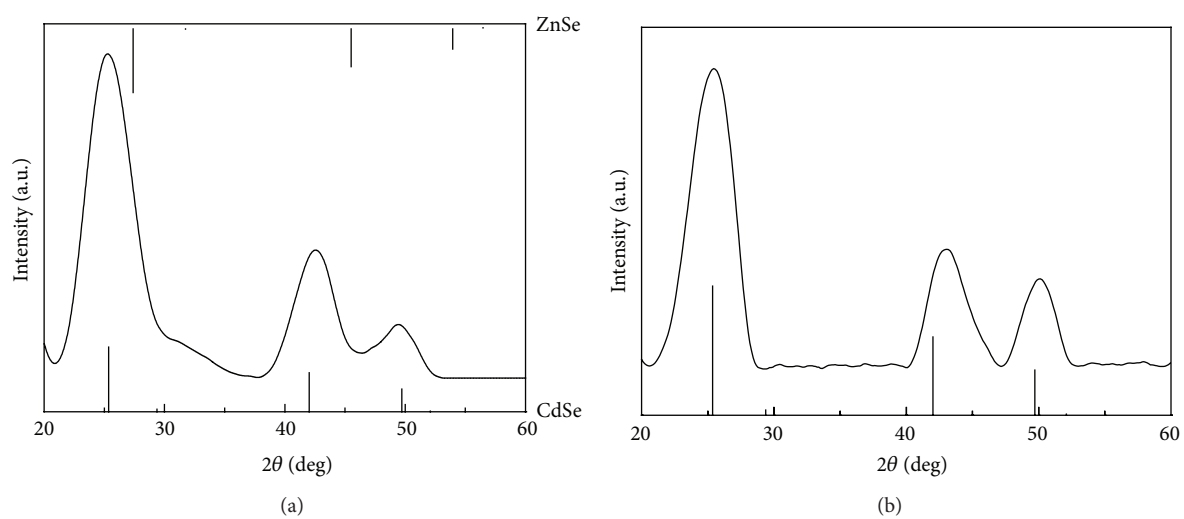


FIGURE 4: XRD patterns of samples. (a) Zn<sub>0.2</sub> and (b) Zn<sub>0.5</sub>.

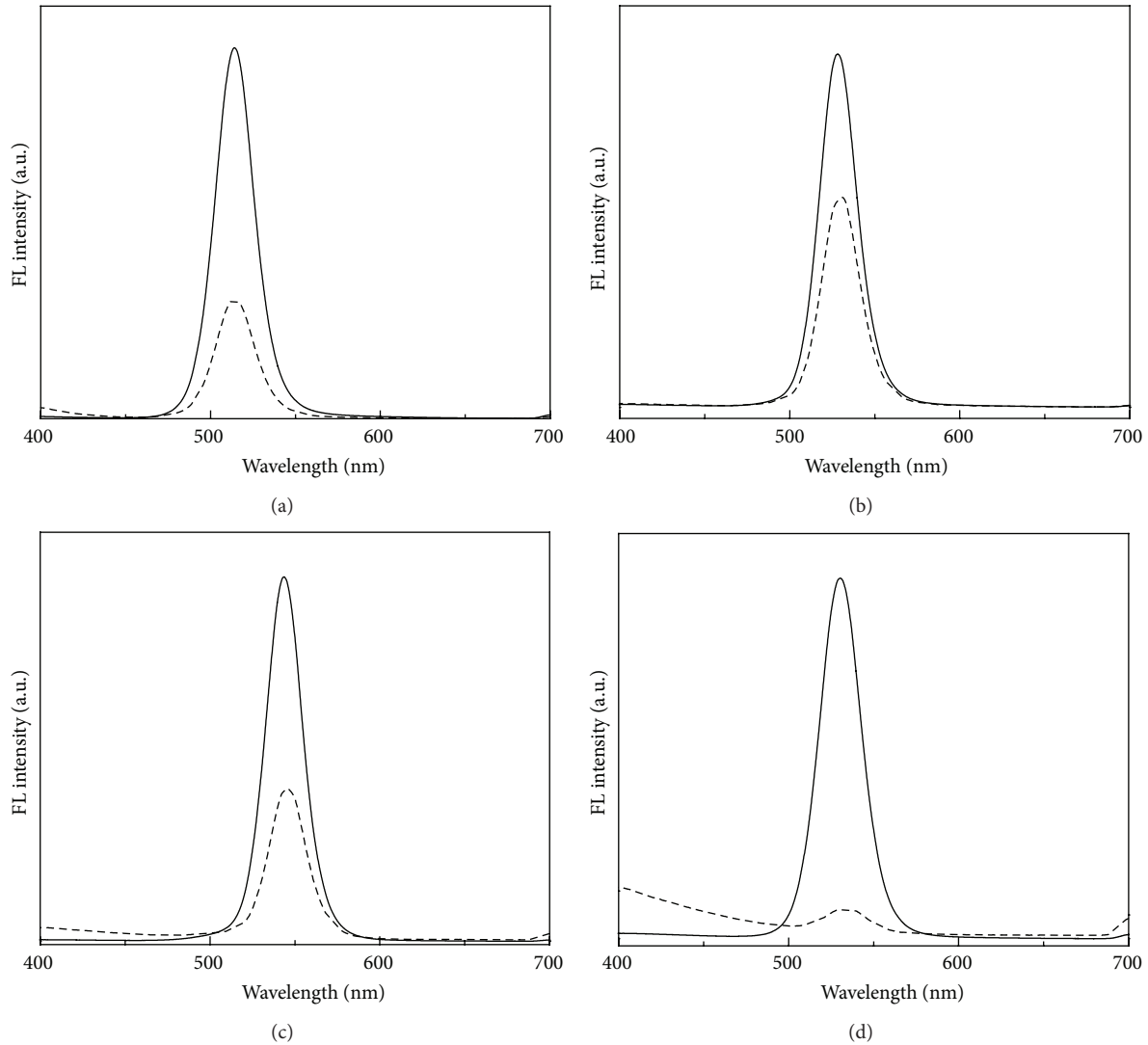


FIGURE 5: FL spectra of samples. (a)  $Zn_0$ , (b)  $Zn_{0.2}$ , (c)  $Zn_{0.5}$ , and (d)  $Zn_{0.8}$ . (Solid line: as-prepared NCs; dash line: aging for 2 months.)

QY are due to larger particle size, high crystallinity, lattice structure, decreased interdiffusion, and spatial composition fluctuation [9]. The emission peak of composition-tunable  $Zn_xCd_{1-x}Se$  NCs moves to short wavelength when increasing the Zn content. On the other hand, Bailey and Nie pointed out that the optical properties of  $CdTe_{1-x}Se_x$  NCs are nonlinear and the emission peaks for  $CdTe_{1-x}Se_x$  NCs are out of the range of that for CdSe and CdTe [10]. According to a theoretical model developed by Bernard and Wei, the nonlinear effect of alloyed NCs is due to the following factors: (1) different atomic size of different ions, (2) different electronegativity values, and (3) different lattice constants [35, 36].

In our study, the emission peaks of ternary  $Zn_xCd_{1-x}Se$  NCs are between those of ZnSe and those of CdSe. However, when the actual Zn mole fraction increases from 0 to 0.38, a significant red shift of  $\sim 35$  nm is observed. This result may be due to the different reactivity and atomic radii of the Zn

and Cd. From ICP results it can be seen very clearly that the Zn content in actual composition of ternary  $Zn_xCd_{1-x}Se$  NCs is much lower than that of the theoretical composition. Therefore, the emission properties of ternary  $Zn_xCd_{1-x}Se$  NCs may be dominated by CdSe under lower Zn content. When the Zn content is higher than a critical value, the emission wavelength of ternary  $Zn_xCd_{1-x}Se$  NCs may either shift to short wavelength or appear as two wavelengths. In this situation, the optical properties of ternary  $Zn_xCd_{1-x}Se$  NCs may be dominated by ZnSe, and the QY is also decreased. In this study, because the actual Zn content in alloy is not high enough, the nonlinear optical properties can be observed.

Figure 4 shows the XRD patterns of  $Zn_{0.2}$  and  $Zn_{0.5}$  sample. A face centered cubic (FCC) structure similar to pure CdSe NC is obtained for  $Zn_{0.2}$ , while a slight peak shift of NC is observed for  $Zn_{0.5}$ . As the Zn content increases, the diffraction peaks shift toward larger angles. The XRD results are also consistent with ICP and confirm again that ternary

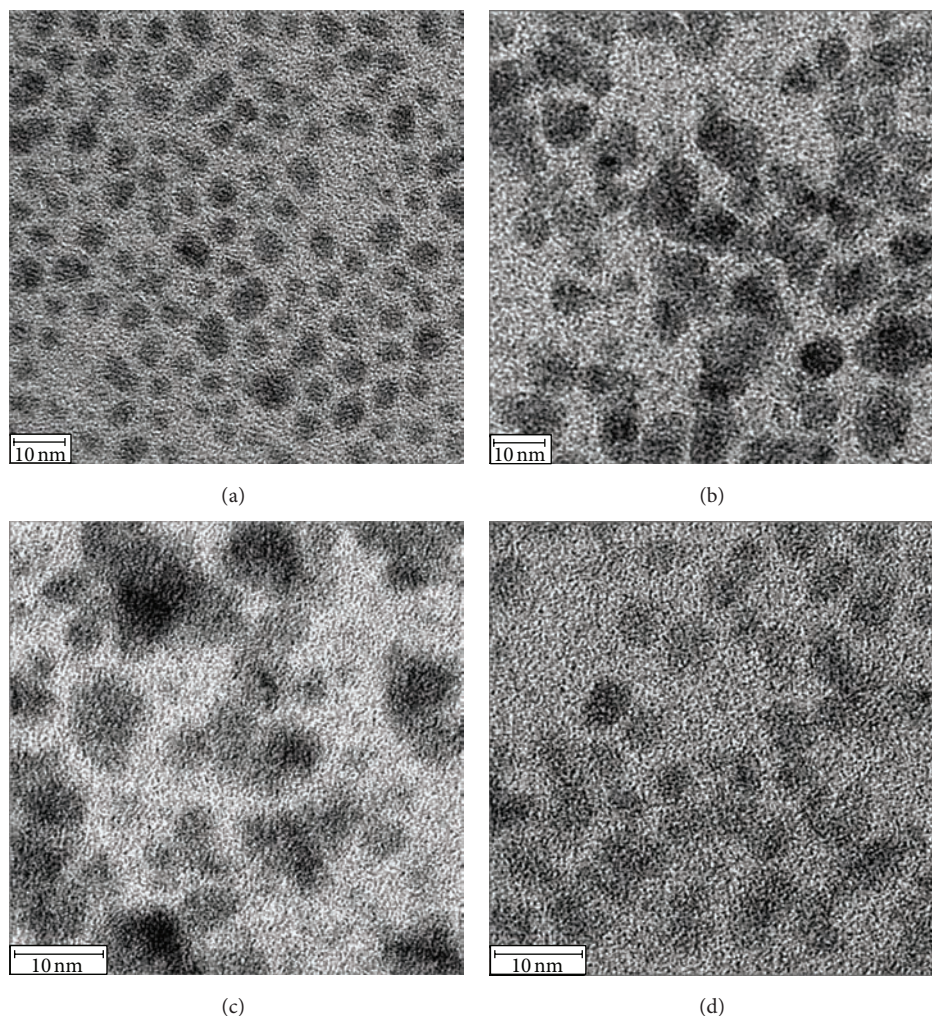


FIGURE 6: TEM images of samples aging for 2 months. (a)  $Zn_0$ , (b)  $Zn_{0.2}$ , (c)  $Zn_{0.5}$ , and (d)  $Zn_{0.8}$ .

alloyed  $Zn_xCd_{1-x}Se$  NCs can be prepared under high Zn content. On the other hand, a doping effect can be found under lower Zn content.

**3.3. Stability of NCs.** In order to investigate the stability of NCs, all of the samples were dissolved in hexane and stored in dark for 2 months. The FL spectra and TEM micrographs of  $Zn_xCd_{1-x}Se$  NCs are shown in Figures 5 and 6, respectively. In Figure 5, the FL intensity for all of the samples decreases after aging for 2 months. It is interesting to find that the peak position of emission wavelengths for all samples is almost the same compared to as-prepared samples, but the intensity of peak for all samples decreases, resulting in a decrease in QY. Moreover, only one emission peak can be observed, and its FWHM increases slightly. For the TEM observation shown in Figure 6, we can find that the size distribution of all samples is not uniform. Moreover, the shape of NCs changes from spherical to elliptical and the size becomes bigger than that of as-prepared one. The QY of samples decreases after aging for 2 months as shown in Table 2. The  $Zn_{0.2}$  shows the best stability in all samples. As

we know that the capping agent such as TOPO and HDA covers the surface of NCs, resulting in improving the QY. The interaction between those surfactants and surface of NCs becomes weak as aging time increases. Therefore, Ostwald ripening occurs, resulting in nonuniform size distribution of NCs because small particles dissolve and deposit on the large particle surface. Moreover, once the Ostwald ripening occurs, the capping agents are not adsorbed on the surface of NC anymore. Therefore, only one emission peak with lower intensity can be observed, and the QY of aging sample decreases due to the concentration of capped-NCs decreases. Larger particle of NCs formed by the Ostwald ripening cannot emit light, so only one emission wavelength appears in Figure 5.

#### 4. Conclusion

An effective and facile one-pot synthetic method has been developed for the formation of highly luminescent, composition tunable, high QY, and high-quality green emitting  $Zn_xCd_{1-x}Se$  NCs. The emission wavelength from 512 to

TABLE 2: Physical properties of samples aging for 2 months.

Theoretical composition	Emission wavelength (nm)	As-prepared QY (%)	After-aged QY (%)	Size range (nm)
Zn <sub>0</sub>	512	58	16	2.8~5.1
Zn <sub>0.2</sub>	523	89	51	2.8~5.5
Zn <sub>0.5</sub>	534	81	26	2.9~5.6
Zn <sub>0.8</sub>	545	45	9	3.0~5.9
Zn <sub>1</sub>	—	—	—	—

545 nm can be tuned by changing the composition of the Zn<sub>x</sub>Cd<sub>1-x</sub>Se NCs from Zn<sub>0</sub> to Zn<sub>0.8</sub>. Besides, not only Stokes shift but also the FWHM of ternary Zn<sub>x</sub>Cd<sub>1-x</sub>Se NCs is very small, implying that a narrow size distribution and saturated color of ternary Zn<sub>x</sub>Cd<sub>1-x</sub>Se NCs can be obtained. The Zn content of ternary Zn<sub>x</sub>Cd<sub>1-x</sub>Se NCs affects their optical properties significantly. When increasing the amount of Zn from 0.2 to 0.8, the emission peak is red-shifted from 523 to 545 nm and the QY decreases from 89 to 45%, respectively. From the TEM analysis, those samples have almost the same particle size, indirectly suggesting that the nonlinear optical property of Zn<sub>x</sub>Cd<sub>1-x</sub>Se is caused by the Zn compositional effect instead of the size effect. The one-pot preparation method reported in this study cannot only reduce the concentration of Cd but can also maintain the QY of NCs. Moreover, this would be a new class of colloidal chemistry method to prepare high quality of green emitting NCs and use them as a phosphor in white LED.

## Acknowledgment

This work was supported by the National Science Council of ROC under Contracts 99-2221-E-150-053 and 100-2221-E-150-063.

## References

- X. Peng, J. Wickham, and A. P. Alivisatos, "Kinetics of II-VI and III-V colloidal semiconductor nanocrystal growth: "focusing" of size distributions," *Journal of the American Chemical Society*, vol. 120, no. 21, pp. 5343–5344, 1998.
- A. P. Alivisatos, "Perspectives on the physical chemistry of semiconductor nanocrystals," *The Journal of Physical Chemistry*, vol. 100, no. 31, pp. 13226–13239, 1996.
- V. L. Colvin, M. C. Schlamp, and A. P. Alivisatos, "Light-emitting diodes made from cadmium selenide nanocrystals and a semiconducting polymer," *Nature*, vol. 370, no. 6488, pp. 354–357, 1994.
- C. Y. Huang, Y. K. Su, Y. C. Chen, P. C. Tsai, C. T. Wan, and W. L. Li, "Hybrid CdSe-ZnS quantum Dot-InGaN-GaN quantum well red light-emitting diodes," *IEEE Electron Device Letters*, vol. 29, no. 7, pp. 711–713, 2008.
- B. O. Dabbousi, J. Rodriguez-Viejo, F. V. Mikulec et al., "(CdSe)ZnS core-shell quantum dots: synthesis and characterization of a size series of highly luminescent nanocrystallites," *Journal of Physical Chemistry B*, vol. 101, no. 46, pp. 9463–9475, 1997.
- J. Ouyang, M. Vincent, D. Kingston et al., "Noninjection, one-pot synthesis of photoluminescent colloidal homogeneously alloyed CdSeS quantum dots," *Journal of Physical Chemistry C*, vol. 113, no. 13, pp. 5193–5200, 2009.
- V. I. Klimov, A. A. Mikhailovsky, S. Xu et al., "Optical gain and stimulated emission in nanocrystal quantum dots," *Science*, vol. 290, no. 5490, pp. 314–317, 2000.
- M. V. Artemyev, U. Woggon, R. Wannemacher, H. Jaschinski, and W. Langbein, "Light trapped in a photonic dot: microspheres act as a cavity for quantum dot emission," *Nano Letters*, vol. 1, no. 6, pp. 309–314, 2001.
- X. Zhong, M. Han, Z. Dong, T. J. White, and W. Knoll, "Composition-tunable Zn<sub>x</sub>Cd<sub>1-x</sub>Se nanocrystals with high luminescence and stability," *Journal of the American Chemical Society*, vol. 125, no. 28, pp. 8589–8594, 2003.
- R. E. Bailey and S. Nie, "Alloyed semiconductor quantum dots: tuning the optical properties without changing the particle size," *Journal of the American Chemical Society*, vol. 125, no. 23, pp. 7100–7106, 2003.
- M. Bruchez Jr., M. Moronne, P. Gin, S. Weiss, and A. P. Alivisatos, "Semiconductor nanocrystals as fluorescent biological labels," *Science*, vol. 281, no. 5385, pp. 2013–2016, 1998.
- X. Zhong, Y. Feng, W. Knoll, and M. Han, "Alloyed Zn<sub>x</sub>Cd<sub>1-x</sub>S nanocrystals with highly narrow luminescence spectral width," *Journal of the American Chemical Society*, vol. 125, no. 44, pp. 13559–13563, 2003.
- T. Hasobe, H. Imahori, P. V. Kamat et al., "Photovoltaic cells using composite nanoclusters of porphyrins and fullerenes with gold nanoparticles," *Journal of the American Chemical Society*, vol. 127, no. 4, pp. 1216–1228, 2005.
- A. L. Linsebigler, G. Lu, and J. T. Yates Jr., "Photocatalysis on TiO<sub>2</sub> surfaces: principles, mechanisms, and selected results," *Chemical Reviews*, vol. 95, no. 3, pp. 735–758, 1995.
- G.-W. Huang, C.-Y. Chen, K.-C. Wu, M. O. Ahmed, and P.-T. Chou, "One-pot synthesis and characterization of high-quality CdSe/ZnX (X = S, Se) nanocrystals via the CdO precursor," *Journal of Crystal Growth*, vol. 265, no. 1-2, pp. 250–259, 2004.
- Y. Chan, J. P. Zimmer, M. Stroh, J. S. Steckel, R. K. Jain, and M. G. Bawendi, "Incorporation of luminescent nanocrystals into monodisperse core-shell silica microspheres," *Advanced Materials*, vol. 16, no. 23-24, pp. 2092–2097, 2004.
- C. Y. Chen, C. T. Cheng, J. K. Yu, S. C. Pu, Y. M. Cheng, and P. T. Chou, "Spectroscopy and femtosecond dynamics of type-II CdSe/ZnTe core-shell semiconductor synthesized via the CdO precursor," *The Journal of Physical Chemistry B*, vol. 108, no. 30, pp. 10687–10691, 2004.
- B. O. Dabbousi, J. Rodriguez-Viejo, F. V. Mikulec et al., "(CdSe)ZnS core-shell quantum dots: synthesis and characterization of a size series of highly luminescent nanocrystallites," *Journal of Physical Chemistry B*, vol. 101, no. 46, pp. 9463–9475, 1997.
- D. V. Talapin, A. L. Rogach, A. Kornowski, M. Haase, and H. Weller, "Highly luminescent monodisperse CdSe and

- CdSe/ZnS nanocrystals synthesized in a hexadecylamine-trioctylphosphine oxide-trioctylphosphine mixture,” *Nano Letters*, vol. 1, no. 4, pp. 207–211, 2001.
- [20] P. Reiss, J. Bleuse, and A. Pron, “Highly luminescent CdSe/ZnSe core/shell nanocrystals of low size dispersion,” *Nano Letters*, vol. 2, no. 7, pp. 781–784, 2002.
- [21] B. Moden, L. Oliviero, J. Dakka, J. G. Santiesteban, and E. Iglesia, “Structural and functional characterization of redox Mn and Co sites in AlPO materials and their role in alkane oxidation catalysis,” *The Journal of Physical Chemistry B*, vol. 108, no. 18, pp. 5552–5563, 2004.
- [22] H. Lee, H. Yang, and P. H. Holloway, “Single-step growth of colloidal ternary ZnCdSe nanocrystals,” *Journal of Luminescence*, vol. 126, no. 2, pp. 314–318, 2007.
- [23] N. P. Gurusinge, N. N. Hewa-Kasakarage, and M. Zamkov, “Composition-tunable properties of  $\text{CdS}_x\text{Te}_{1-x}$  alloy nanocrystals,” *Journal of Physical Chemistry C*, vol. 112, no. 33, pp. 12795–12800, 2008.
- [24] L. A. Swafford, L. A. Weigand, M. J. Bowers II et al., “Homogeneously alloyed  $\text{CdS}_x\text{Se}_{1-x}$  nanocrystals: synthesis, characterization, and composition/size-dependent band gap,” *Journal of the American Chemical Society*, vol. 128, no. 37, pp. 12299–12306, 2006.
- [25] M. W. DeGroot, K. M. Atkins, A. Borecki, H. Rosner, and J. F. Corrigan, “A molecular precursor approach for the synthesis of composition-controlled  $\text{Zn}_x\text{Cd}_{1-x}\text{S}$  and  $\text{Zn}_x\text{Cd}_{1-x}\text{Se}$  nanoparticles,” *Journal of Materials Chemistry*, vol. 18, pp. 1123–1130, 2008.
- [26] X. Zhong, Y. Feng, Y. Zhang, Z. Gu, and L. Zou, “A facile route to violet- to orange-emitting  $\text{Cd}_x\text{Zn}_{1-x}\text{Se}$  alloy nanocrystals via cation exchange reaction,” *Nanotechnology*, vol. 18, no. 38, Article ID 385606, 2007.
- [27] Z. A. Peng and X. G. Peng, “Mechanisms of the shape evolution of CdSe nanocrystals,” *Journal of the American Chemical Society*, vol. 123, no. 7, pp. 1389–1395, 2001.
- [28] Z. A. Peng and X. Peng, “Formation of high-quality CdTe, CdSe, and CdS nanocrystals using CdO as precursor,” *Journal of the American Chemical Society*, vol. 123, no. 1, pp. 183–184, 2001.
- [29] L. Qu, Z. A. Peng, and X. Peng, “Alternative routes toward high quality CdSe nanocrystals,” *Nano Letters*, vol. 1, no. 6, pp. 333–337, 2001.
- [30] L. Qu and X. Peng, “Control of photoluminescence properties of CdSe nanocrystals in growth,” *Journal of the American Chemical Society*, vol. 124, no. 9, pp. 2049–2055, 2002.
- [31] X. G. Peng, M. C. Schlamp, A. V. Kadavanich, and A. P. Alivisatos, “Epitaxial growth of highly luminescent CdSe/CdS core/shell nanocrystals with photostability and electronic accessibility,” *Journal of the American Chemical Society*, vol. 119, no. 30, pp. 7019–7029, 1997.
- [32] M. A. Hines and P. Guyot-Sionnest, “Bright UV-blue luminescent colloidal ZnSe nanocrystals,” *The Journal of Physical Chemistry B*, vol. 102, no. 19, pp. 3655–3657, 1998.
- [33] L. Qu, Z. A. Peng, and X. Peng, “Alternative routes toward high quality CdSe nanocrystals,” *Nano Letters*, vol. 1, no. 6, pp. 333–337, 2001.
- [34] D. Shaw, “Diffusion mechanisms in II-VI materials,” *Journal of Crystal Growth*, vol. 86, no. 1–4, pp. 778–796, 1990.
- [35] J. E. Bernard and A. Zunger, “Electronic structure of ZnS, ZnSe, ZnTe, and their pseudobinary alloys,” *Physical Review B*, vol. 36, no. 6, pp. 3199–3228, 1987.
- [36] S. H. Wei, S. B. Zhang, and A. Zunger, “First-principles calculation of band offsets, optical bowings, and defects in CdS, CdSe, CdTe, and their alloys,” *Journal of Applied Physics*, vol. 87, no. 3, pp. 1304–1311, 2000.

## Research Article

# Morphology and Optical Property of ZnO Nanostructures Grown by Solvothermal Method: Effect of the Solution Pretreatment

Wenhui Zhang,<sup>1,2</sup> Xiahui Chen,<sup>3</sup> Ning Xu,<sup>1</sup> Rong Xiang,<sup>2</sup> Yuan Zhu,<sup>2</sup> and Zikang Tang<sup>2,4</sup>

<sup>1</sup> New Environmental Protection Key Laboratory of Jiangsu Province, Yancheng Institute of Technology, Yancheng 224051, China

<sup>2</sup> State Key Lab of Optoelectronic Materials and Technologies, School of Physics and Engineering, Sun Yat-sen University, Guangzhou 510006, China

<sup>3</sup> School of Microelectronics and Solid-State Electronics, University of Electronic Science and Technology of China, Shahe Campus, Chengdu 610054, China

<sup>4</sup> Physics Department, Hong Kong University of Science and Technology, Clear Water Bay, Kowloon, Hong Kong

Correspondence should be addressed to Wenhui Zhang; [zwhuizi000@sina.com](mailto:zwhuizi000@sina.com)

Received 1 April 2013; Accepted 23 July 2013

Academic Editor: Pathik Kumbhakar

Copyright © 2013 Wenhui Zhang et al. This is an open access article distributed under the Creative Commons Attribution License, which permits unrestricted use, distribution, and reproduction in any medium, provided the original work is properly cited.

Zinc oxide (ZnO) nanostructures with different morphologies such as nanopyramids, nanosheets, and nanoparticles have been grown by a simple solvothermal method. The influence of solution pretreatment on the morphology and optical properties of ZnO nanostructures has been studied. The experimental results revealed the morphology of ZnO transformed from nanopyramids or nanosheets to nanoparticles after solution pretreatment. Raman and photoluminescence spectra are recorded to examine the crystallinity and optical property of the samples.

## 1. Introduction

ZnO has been recognized as one of the most important II–VI compound semiconductor materials in scientific research and technological applications, owing to its wide direct band-gap (3.37 eV), large exciton binding energy (60 meV) at room temperature [1, 2], noncentrosymmetric structures, and various shape-induced functions. Compared to the bulk material, ZnO nanostructures have a wide range of applications including catalysts [3], piezoelectric devices [4], optoelectronic devices [5], photovoltaic cells [6], and gas sensors [7, 8] due to their unique physical and chemical properties. In recent years, lots of research has been focused on the synthesis, characteristics, growth mechanism, device fabrication, and performance improvement of ZnO nanostructures with various morphologies including nanowires [9], nanorods [10], nanobelts [11], nanotubes [12], nanosheets [13, 14], nanopyramids [15, 16], hollow nanospheres [17], and quantum dots [18], which have been fabricated via different methods, such as chemical vapor deposition, sol-gel method, hydrothermal method, and solvothermal method [19–22].

Among these, relatively little is known about the controlled synthesis of the different morphologies of ZnO simply by adjusting the synthetic conditions. In this work, we have investigated the influence of solution pretreatment on morphology and optical properties of ZnO nanostructures grown by solvothermal process.

## 2. Materials and Methods

Zinc acetate dihydrate ( $\text{Zn}(\text{OAc})_2 \cdot 2\text{H}_2\text{O}$ , Sinopharm Chemical Reagent Co., Ltd.), zinc nitrate hydrate ( $\text{Zn}(\text{NO}_3)_2 \cdot 6\text{H}_2\text{O}$ , Sinopharm Chemical Reagent Co., Ltd.), oleylamine (OM, 96%, J&K Scientific Ltd.), and dodecanol (DDL, 98%, Acros Organics) used in the experiments were of analytical purity. Typically, 0.5 mmol  $\text{Zn}(\text{OAc})_2 \cdot 2\text{H}_2\text{O}$  or  $\text{Zn}(\text{NO}_3)_2 \cdot 6\text{H}_2\text{O}$  was added to a mixed solvent composed of 3 mL OM and 6 mL DDL at room temperature. The resulting slurry was heated to 120°C in a vacuum to remove water for solution pretreatment. The resulting mixture was transferred into a Teflon-lined stainless steel autoclave (20 mL) for solvothermal synthesis at 180°C for 2 h in an electric oven. After the

reaction, the autoclave was cooled and the ZnO products were centrifuged, rinsed several times with ethanol in order to remove the residual reactants, and dispersed in cyclohexane.

Powder X-ray diffraction (XRD) analyses were performed on a D-MAX 2200 VPC X-ray diffractometer with Cu  $K\alpha$  irradiation ( $\lambda = 1.5406 \text{ \AA}$ ) at a scanning speed of  $0.014^\circ/\text{sec}$  over the  $2\theta$  range of  $20\text{--}60^\circ$ . The electronic morphology of the samples was examined by Hitachi S-4800 scanning electron microscope (SEM) and FEI Tecnai G2 Spirit transmission electron microscope (TEM). Photoluminescence (PL) spectra of samples were recorded using Jobin-Yvon Lab-Ram high-resolution spectrometer with He-Cd laser with the wavelength 325 nm. Raman spectra of samples were recorded using Jobin-Yvon Lab-Ram high-resolution spectrometer with laser of wavelength 633 nm.

### 3. Results and Discussion

The powder X-ray diffraction (XRD) patterns of the as-synthesized samples are shown in Figure 1. The XRD patterns of the samples using  $\text{Zn}(\text{OAc})_2 \cdot 2\text{H}_2\text{O}$  and  $\text{Zn}(\text{NO}_3)_2 \cdot 6\text{H}_2\text{O}$  as raw materials indicate a pure hexagonal wurtzite-type ZnO phase (JCPDS number 75-1526) and (JCPDS number 05-664) with high crystallinity, respectively.

The SEM images of the as-synthesized samples are shown in Figure 2. When  $\text{Zn}(\text{OAc})_2 \cdot 2\text{H}_2\text{O}$  was used as raw material, the samples without solution pretreatment have a pyramidal morphology with an average size of  $\sim 170 \text{ nm}$  (side-edge length). The trigonal and hexagonal particle shapes observed in the TEM image thus correspond to the side-view projections of the pyramids. After solution pretreatment, the samples were transformed into nanoparticles with the average diameter of  $\sim 27 \text{ nm}$ . When  $\text{Zn}(\text{NO}_3)_2 \cdot 6\text{H}_2\text{O}$  was used as raw material, the samples without solution pretreatment have a nanosheet morphology with an average size of  $\sim 55 \text{ nm}$ . The thickness of nanosheet was about  $15 \text{ nm}$ . After solution pretreatment, the samples were also transformed into nanoparticles with the average diameter of  $\sim 26 \text{ nm}$ . From the above experimental results, a possible mechanism can be deduced. The OM-DDL mixture played a key role in the formation of different ZnO nanostructures. The 001 plane is the most rapid growth rate plane during the crystal planes of hexagonal structure ZnO and is the preferred growth direction. When  $\text{Zn}(\text{OAc})_2 \cdot 2\text{H}_2\text{O}$  was used as raw material, the OM-DDL mixture could result in strong electrostatic interaction with the polar surfaces of the growing ZnO nanocrystals thus resulting in decreasing the surface energy of polar surfaces and hence slowing down the growth rate of the polar planes. This could result in the polar plane being the exposed basal surface of the nanopyramid which grows slowly with well-developed facets [23]. When  $\text{Zn}(\text{NO}_3)_2 \cdot 6\text{H}_2\text{O}$  was used as raw material, the intrinsically anisotropic growth of ZnO along the 001 direction is substantially suppressed and crystal growth then proceeds sideways, which results in the formation of ZnO nanosheets. Pretreatment of solution may reduce suppressing effect in the growth of ZnO nanocrystals, leading to the formation of nanoparticles.

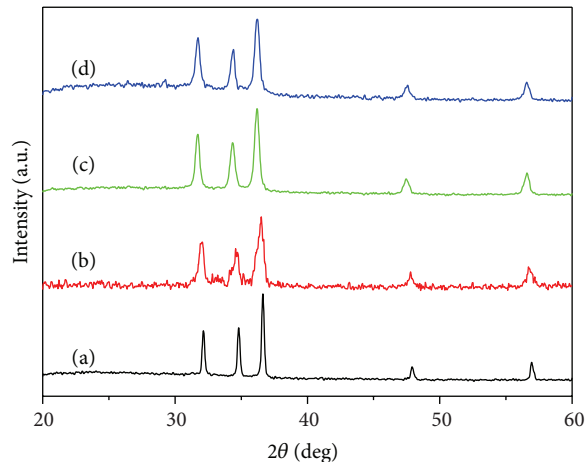


FIGURE 1: XRD patterns of the as-synthesized samples (a) without and (b) with solution pretreatment using  $\text{Zn}(\text{OAc})_2 \cdot 2\text{H}_2\text{O}$  as raw material and (c) without and (d) with solution pretreatment using  $\text{Zn}(\text{NO}_3)_2 \cdot 6\text{H}_2\text{O}$  as raw material.

Raman spectra of ZnO samples using 633 nm laser are shown in Figure 3.  $E_2$  (low) mode at  $99 \text{ cm}^{-1}$  and  $E_2$  (high) mode at  $437 \text{ cm}^{-1}$  dominate in the Raman scattering spectra, indicating that all the samples had perfect crystal quality. The peak at  $331 \text{ cm}^{-1}$  can be attributed to the  $E_2$  (high)- $E_2$  (low) mode of ZnO, which is assigned to the second-order Raman spectrum arising from zone-boundary phonons of the hexagonal ZnO [24, 25].

Figure 4 shows the room temperature PL spectrum of the samples with using 325 nm laser. There are two emission bands in the PL spectrum: a strong and narrow near UV emission at 381 nm and a broad but weak spectral band ranging from 450 to 600 nm. The near UV peak is due to the recombination of electron and hole in an exciton, while the visible emission is due to the presence of various point defects, such as interstitial oxygen and oxygen vacancies. In this work, the visible emission of ZnO nanopyramids and nanosheets is stronger than that of ZnO nanoparticles, suggesting that the content of oxygen vacancy in ZnO nanopyramids and nanosheets is larger than that in ZnO nanoparticles. The observation of such a strong emission band from excitons rather than from defects might imply that the samples hold high crystallinity or low lattice disorder, specially after solution pretreatment.

### 4. Conclusions

ZnO nanostructures have been grown by solvothermal method. The solution pretreatment is a key factor in the morphological control of ZnO nanostructures. The morphology of ZnO transformed from nanopyramids or nanosheets to nanoparticles by solution pretreatment. The process is simple and leads to highly crystalline particles with controllable morphology. The growth mechanism is discussed. ZnO nanopyramids, nanosheets, and nanoparticles exhibit excellent emission properties.

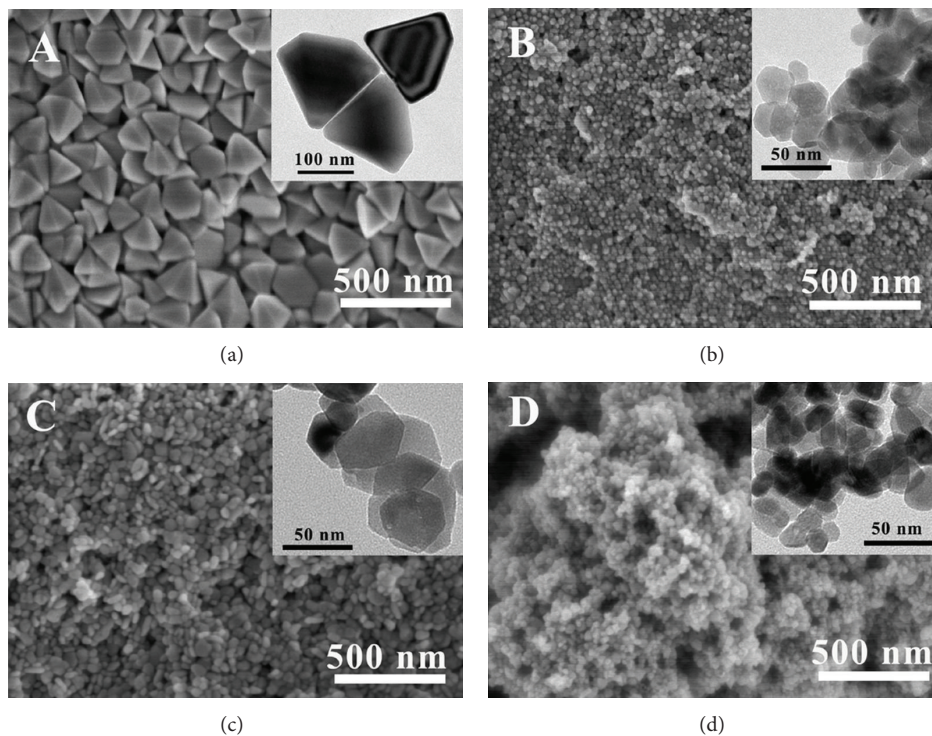


FIGURE 2: SEM images of the samples (a) without and (b) with solution pretreatment using  $\text{Zn}(\text{OAc})_2 \cdot 2\text{H}_2\text{O}$  as raw material and (c) without and (d) with solution pretreatment using  $\text{Zn}(\text{NO}_3)_2 \cdot 6\text{H}_2\text{O}$  as raw material. Inset: TEM images of the corresponding sample.

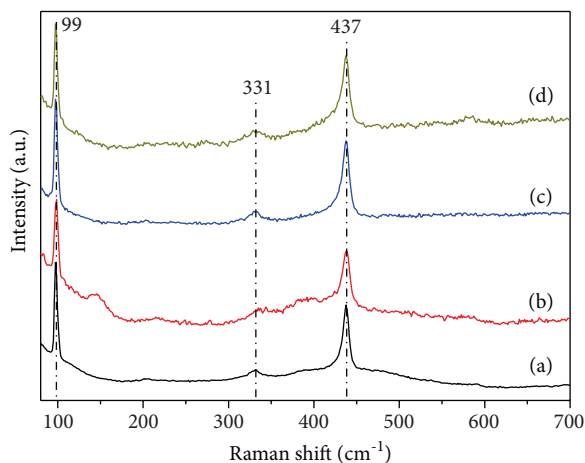


FIGURE 3: Raman spectra of the samples (a) without and (b) with solution pretreatment using  $\text{Zn}(\text{OAc})_2 \cdot 2\text{H}_2\text{O}$  as raw material and (c) without and (d) with solution pretreatment using  $\text{Zn}(\text{NO}_3)_2 \cdot 6\text{H}_2\text{O}$  as raw material.

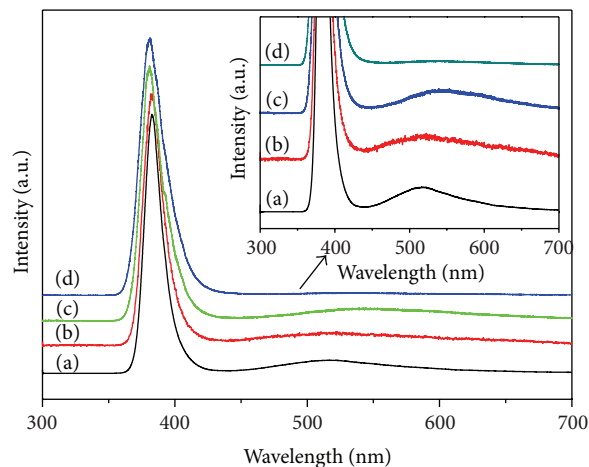


FIGURE 4: PL spectra of the samples (a) without and (b) with solution pretreatment using  $\text{Zn}(\text{OAc})_2 \cdot 2\text{H}_2\text{O}$  as raw material and (c) without and (d) with solution pretreatment using  $\text{Zn}(\text{NO}_3)_2 \cdot 6\text{H}_2\text{O}$  as raw material. Inset: Partial enlarged drawing of PL spectra.

## Acknowledgment

We gratefully acknowledge the financial aids from the China Postdoctoral Science Foundation funded project (Grant no. 2012300004109568) and National Key Technology R&D Program of China (Grant no. 2013BAC13B01).

## References

- [1] M. H. Huang, S. Mao, H. Feick et al., "Room-temperature ultraviolet nanowire nanolasers," *Science*, vol. 292, no. 5523, pp. 1897–1899, 2001.
- [2] P. D. Yang, H. Q. Yan, S. Mao et al., "Controlled growth of ZnO nanowires and their optical properties," *Advanced Functional Materials*, vol. 12, no. 5, pp. 323–331, 2002.

- [3] X. Wang, M. Y. Liao, Y. T. Zhong et al., "ZnO hollow spheres with double-yolk egg structure for high-performance photocatalysts and photodetectors," *Advanced Materials*, vol. 24, no. 25, pp. 3421–3425, 2012.
- [4] Z. L. Wang and J. Song, "Piezoelectric nanogenerators based on zinc oxide nanowire arrays," *Science*, vol. 312, no. 5771, pp. 243–246, 2006.
- [5] J. H. He, J. J. Ke, P. H. Chang et al., "Development of Ohmic nanocontacts via surface modification for nanowire-based electronic and optoelectronic devices: ZnO nanowires as an example," *Nanoscale*, vol. 4, no. 11, pp. 3399–3404, 2012.
- [6] Y. T. Shi, C. Zhu, L. Wang et al., "Optimizing nanosheet-based ZnO hierarchical structure through ultrasonic-assisted precipitation for remarkable photovoltaic enhancement in quasi-solid dye-sensitized solar cells," *Journal of Materials Chemistry*, vol. 22, no. 26, pp. 13097–13103, 2012.
- [7] L. Wang, Y. Kang, X. Liu, S. Zhang, W. Huang, and S. Wang, "ZnO nanorod gas sensor for ethanol detection," *Sensors and Actuators B*, vol. 162, no. 1, pp. 237–243, 2012.
- [8] W. Zhang, W. Zhang, and J. Zhou, "Solvent thermal synthesis and gas-sensing properties of Fe-doped ZnO," *Journal of Materials Science*, vol. 45, no. 1, pp. 209–215, 2010.
- [9] S. Z. Yang, L. F. Wang, X. Z. Tian et al., "The piezotronic effect of Zinc oxide nanowires studied by in situ TEM," *Advanced Materials*, vol. 24, no. 34, pp. 4676–4682, 2012.
- [10] W. Zhang, W. Zhang, and X. Ma, "Tunable ZnO nanostructures for ethanol sensing," *Journal of Materials Science*, vol. 44, no. 17, pp. 4677–4682, 2009.
- [11] Y. Yang, G. Wang, and X. Li, "Water molecule-induced stiffening in ZnO nanobelts," *Nano Letters*, vol. 11, no. 7, pp. 2845–2848, 2011.
- [12] Z. Liang, H. Cui, K. Wang et al., "Morphology-controllable ZnO nanotubes and nanowires: synthesis, growth mechanism and hydrophobic property," *CrystEngComm*, vol. 14, no. 5, pp. 1723–1728, 2012.
- [13] H. Li, Y. Zhang, and J. Wang, "ZnO nanosheets derived from surfactant-directed process: growth mechanism, and application in dye-sensitized solar cells," *Journal of the American Ceramic Society*, vol. 95, no. 4, pp. 1241–1246, 2012.
- [14] H. Yan, Z. Yu, K. Lu, Y. Zhang, and Z. Wei, "Self-assembly of graphenelike ZnO superstructured nanosheets and their application in hybrid photoconductors," *Small*, vol. 7, no. 24, pp. 3472–3478, 2011.
- [15] P. Li, Z. Wei, T. Wu, Q. Peng, and Y. Li, "Au-ZnO hybrid nanopyrramids and their photocatalytic properties," *Journal of the American Chemical Society*, vol. 133, no. 15, pp. 5660–5663, 2011.
- [16] K. X. Yao, X. Liu, L. Zhao, H. C. Zeng, and Y. Han, "Site-specific growth of Au particles on ZnO nanopyrramids under ultraviolet illumination," *Nanoscale*, vol. 3, no. 10, pp. 4195–4200, 2011.
- [17] C. Q. Zhu, B. A. Lu, Q. Su et al., "A simple method for the preparation of hollow ZnO nanospheres for use as a high performance photocatalyst," *Nanoscale*, vol. 4, no. 10, pp. 3060–3064, 2012.
- [18] D. A. Firmansyah, S. Kim, K. Lee, R. Zahaf, Y. H. Kim, and D. Lee, "Microstructure-controlled aerosol-gel synthesis of ZnO quantum dots dispersed in SiO<sub>2</sub> nanospheres," *Langmuir*, vol. 28, no. 5, pp. 2890–2896, 2012.
- [19] J. E. Stehr, S. L. Chen, S. Filippov et al., "Defect properties of ZnO nanowires revealed from an optically detected magnetic resonance study," *Nanotechnology*, vol. 24, no. 1, Article ID 015701, 2013.
- [20] Q. Zhang, C. G. Tian, A. P. Wu et al., "A facile one-pot route for the controllable growth of small sized and well-dispersed ZnO particles on GO-derived graphene," *Journal of Materials Chemistry*, vol. 22, no. 23, pp. 11778–11784, 2012.
- [21] J. Joo, B. Y. Chow, M. Prakash, E. S. Boyden, and J. M. Jacobson, "Face-selective electrostatic control of hydrothermal zinc oxide nanowire synthesis," *Nature Materials*, vol. 10, no. 8, pp. 596–601, 2011.
- [22] L. Sun, H. Shi, W. Li et al., "Lanthanum-doped ZnO quantum dots with greatly enhanced fluorescent quantum yield," *Journal of Materials Chemistry*, vol. 22, no. 17, pp. 8221–8227, 2012.
- [23] N. P. Herring, K. Abouzeid, M. B. Mohamed, J. Pinski, and M. S. El-Shall, "Formation mechanisms of gold-zinc oxide hexagonal nanopyrramids by heterogeneous nucleation using microwave synthesis," *Langmuir*, vol. 27, no. 24, pp. 15146–15154, 2011.
- [24] K. A. Alim, V. A. Fonoberov, M. Shamsa, and A. A. Balandin, "Micro-Raman investigation of optical phonons in ZnO nanocrystals," *Journal of Applied Physics*, vol. 97, no. 12, Article ID 124313, pp. 1–5, 2005.
- [25] A. J. Reddy, M. K. Kokila, H. Nagabhushana et al., "Combustion synthesis, characterization and Raman studies of ZnO nanopowders," *Spectrochimica Acta A*, vol. 81, no. 1, pp. 53–58, 2011.

## Research Article

# Optical Properties and *In Vitro* Biological Studies of Oligonucleotide-Modified Quantum Dots

Valérie A. Gérard,<sup>1</sup> Mark Freeley,<sup>1</sup> Eric Defrancq,<sup>2</sup>  
Anatoly V. Fedorov,<sup>3</sup> and Yurii K. Gun'ko<sup>1,3</sup>

<sup>1</sup> School of Chemistry and CRANN, Trinity College Dublin, Dublin 2, Ireland

<sup>2</sup> Département de Chimie Moléculaire, UMR CNRS 5250, Université Grenoble Alpes, 38000 Grenoble, France

<sup>3</sup> Saint Petersburg National Research University of Information Technologies, Mechanics and Optics, 197101 Saint Petersburg, Russia

Correspondence should be addressed to Yurii K. Gun'ko; [igounko@tcd.ie](mailto:igounko@tcd.ie)

Received 9 May 2013; Accepted 14 August 2013

Academic Editor: Pathik Kumbhakar

Copyright © 2013 Valérie A. Gérard et al. This is an open access article distributed under the Creative Commons Attribution License, which permits unrestricted use, distribution, and reproduction in any medium, provided the original work is properly cited.

Water-soluble semiconducting nanocrystals or quantum dots (QDs) have attracted much interest in recent years due to their tuneable emission and potential applications in photonics and biological imaging. Fluorescence resonance energy transfer (FRET) processes are very important for elucidating biochemical mechanisms *in vitro*, and QDs constitute an excellent substrate for this purpose. In this work, new oligonucleotide-functionalised CdTe-based QDs were prepared, characterised and biologically tested. These QDs demonstrated interesting optical properties as well as remarkable *in vitro* behaviour and potential for a range of biological applications.

## 1. Introduction

Quantum dots (QDs) are semiconductor nanoparticles where the electrons and holes are quantum-confined, which translates into strong photoluminescence (PL) in the visible range. The emission wavelength is directly related to the particle size as larger particles will absorb lower energy, that is, longer wavelength photons [1]. Water-soluble CdTe-based QDs have attracted much interest in recent years for their potential applications in biological imaging especially, which consists in illuminating the cell membrane, the cytoplasm, or selected organelles using a fluorophore [2–14]. Choosing an appropriate combination of staining agents enables one to elucidate cellular structures or mechanisms by visualising them with a fluorescence or confocal microscope. In this area, QDs have a number of advantages over organic dyes. QDs have a continuous absorption spectrum for wavelengths that are shorter than the emission wavelength and a narrow and symmetrical emission which can be tuned to a particular wavelength by changing the particle size. It is therefore possible to excite QDs of various colours with the same source and to spectrally resolve their emissions [15].

The aqueous synthesis of thiol-stabilised CdTe QDs has been reported and optimised over the last years and adapted for different types of ligands [2, 4, 16]. Recently, Tikhomirov and coworkers published a method for producing oligonucleotide-modified CdTe QDs using phosphorothioate-functionalised oligonucleotide sequences [17]. They also demonstrated how the number of strands to be immobilised on a single QD is highly dependent on the QD-binding domain of oligonucleotides as well as the particle diameter. On the other hand, QDs are excellent candidates for the observation of fluorescence resonance energy transfer (FRET) phenomena [1, 17–32] owing to their narrow and symmetrical emission spectra. The sensitive distance dependence of FRET makes it a powerful tool for resolving bio-chemical processes *in vitro* and biosensing [23, 33–41]. In this work, a range of oligonucleotide-modified QDs were produced and fully characterised. The role of hybridisation and melting of double-stranded (ds)-DNA in QD interactions was investigated, and the occurrence of energy transfer was studied with various degrees of spectral overlap between donor and acceptor. Finally, the potential of the

new bionanocomposites for *in vitro* biological imaging was assessed.

## 2. Materials and Methods

**2.1. Materials.** The oligonucleotides with the sequences (5' NH<sub>2</sub>-A<sub>10</sub> TAG GAA TAG TTA TCA (T<sub>6</sub>) 3' and 5' NH<sub>2</sub>-A<sub>10</sub> TGA TAA CTA TTC CTA (T<sub>6</sub>) 3') were prepared according to standard on-support oligonucleotide synthesis. T6 phosphorothioate tail was prepared by using Beaucage reagent during oxidation steps and 5-amino group was introduced at the last step of DNA synthesis by using the corresponding phosphoramidite C6-amino linker from Eurogentec. Al<sub>2</sub>Te<sub>3</sub> was purchased from Cerac Inc. All other chemicals for QD synthesis were purchased from Sigma-Aldrich.

**2.2. Synthesis of Oligonucleotide-Modified CdTe QDs.** We used a modification of the method developed by Gaponik et al. [16] to produce CdTe QDs stabilised with Thioglycolic acid (TGA). Briefly, cadmium perchlorate hydrate Cd(ClO<sub>4</sub>)<sub>2</sub>·6H<sub>2</sub>O (5.5 g) and TGA (1.2 mL) were added to 150 mL degassed Millipore water. The pH of the solution was adjusted to 11 by dropwise addition of a 2 M NaOH solution. 30 μL of 100 μM aqueous solution of oligonucleotide (oligo-1: 5' NH<sub>2</sub>-A<sub>10</sub> TAG GAA TAG TTA TCA (T<sub>6</sub>) 3' or oligo-2: 5' NH<sub>2</sub>-A<sub>10</sub> TGA TAA CTA TTC CTA (T<sub>6</sub>) 3') was added to the solution. To 0.5 g of Al<sub>2</sub>Te<sub>3</sub> 15 mL of H<sub>2</sub>SO<sub>4</sub> was added to generate H<sub>2</sub>Te gas which then bubbled through the Cd/thiol solution. The resulting nonluminescent solution was then heated under reflux. Once the QDs reached the desired size, the reflux was stopped and different fractions were obtained via size-selective precipitation using isopropanol. The final samples were further purified on a Sephadex-G25 column.

**2.3. In Vitro Cellular Assay.** HT1080 cells were cultured in a medium (500 mL Minimum Essential Medium (MEM) supplemented with 0.055 g of sodium pyruvate, 5 mL of a solution of penicillin (2 mM) and streptomycin (2 mM), 5 mL of 1 mM gentamicin, and 100 mL of fetal bovine serum (FBS) at 37°C and in a 5% CO<sub>2</sub> atmosphere. Cells were plated in 35 cm<sup>2</sup> glass-bottomed petri dishes (from iBidi) at a final concentration of 10<sup>5</sup> cells per dish and left to adhere overnight. Half of the cell medium was then removed from all dishes and replaced by serum-free medium. Cells were incubated for another 4 hours. QDs were added to a final concentrations of 10<sup>-7</sup> mol/L in Dulbecco's modified phosphate buffered saline (DPBS) with sodium chloride and magnesium chloride, and cells were incubated for another 4 hours. The QD-containing medium was aspirated out of the dishes and the cells were washed three times with DPBS. The cell cultures were finally imaged using an Olympus FV-1000 confocal microscope.

## 3. Results and Discussion

Complementary sequences of oligonucleotides bearing a T6 phosphorothioate tail at their 3' end and an amino function at their 5' end (5' NH<sub>2</sub>-A<sub>10</sub> TAG GAA TAG TTA TCA (T<sub>6</sub>) 3'

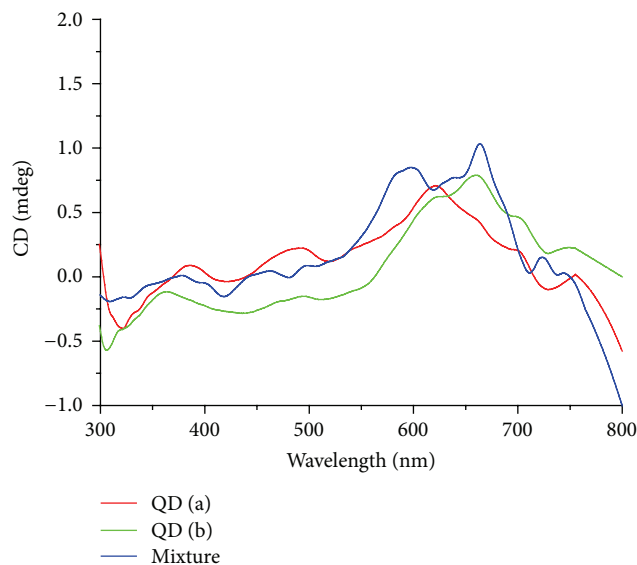


FIGURE 1: CD spectra of QDs modified with complementary oligonucleotide sequences and their mixture in 1:1 ratio.

and 5' NH<sub>2</sub>-A<sub>10</sub> TGA TAA CTA TTC CTA (T<sub>6</sub>) 3') were used to synthesise three series of modified QDs. The procedure was adapted from the work of Tikhomirov et al. [17]. A range of QD sizes were thus produced and enabled to interact through DNA hybridising. The optical properties of the new composites were investigated, as well as their behaviour in *in vitro* cell cultures.

The presence of oligonucleotides on the surface of QDs and their ability to hybridise with the complementary sequence immobilised on other QDs were confirmed by several instrumental techniques. First, circular dichroism (CD) spectra were recorded for QDs modified with complementary oligonucleotides as well as a one-to-one mixture of those. They exhibited a weak signal in the 500–800 nm range, which corresponds to the position of the exciton peak. The corresponding spectra are shown in Figure 1. It was previously reported that plasmonic nanoparticles may induce CD in that region when a chiral molecule, such as an oligonucleotide, is immobilised on their surface and aggregation occurs [42]. It was also demonstrated that QDs did not produce such an effect when oligonucleotides were coupled to the TGA ligand [42]. In the present case, however, oligonucleotides were bound directly to the surface of QDs, which allowed for closer interactions. The T6 phosphorothioate tail was assumed to lay on the surface, and as a result, the chiral moiety was in direct contact with the particle surface. When bound to the ligand, however, electrostatic repulsion between the carboxylic acid groups and the DNA backbone prevented such contact. Furthermore, it may be assumed that CD signal was generated through local chiral distortion of the crystal structure by chiral ligands, such as previously demonstrated for penicillamine-stabilised CdS and CdSe QDs [43–45]. The CD signal was also not significantly altered by the mixing of complementary-modified

TABLE 1: Characterisation of oligonucleotide-modified QDs.

Sample	Oligonucleotide	Absorption (nm)	Emission (nm)	Quantum yield	Diameter (nm)	Zeta potential (mV)
Donor (a)	Oligo-2	525	558	27%	2.7	-44
Acceptor (a)	Oligo-1	556	592	25%	3.7	-29
Donor (b)	Oligo-1	535	560	50%	2.9	-35
Acceptor (b)	Oligo-2	601	644	51%	5.2	-40
Donor (c)	Oligo-2	531	567	6%	2.9	-47
Acceptor (c)	Oligo-1	556	592	25%	3.7	-29

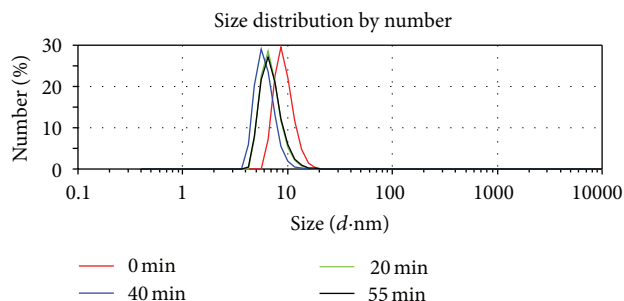


FIGURE 2: DLS measurements of a 1:1 mixture of QDs modified with complementary oligonucleotide sequences and incubated for 0 to 55 min.

QDs, thus confirming the predominant role of surface fragments.

For further assessment of the binding effect of oligonucleotides, a 1:1 mixture of QD-oligo 1 and QD-oligo 2 was scanned by dynamic light scattering (DLS) in order to measure the changes of the hydrodynamic diameter over time. Figure 2 displays the graph of hydrodynamic diameter distribution from 0 to 55 min of incubation.

The initial mixing of both types of QDs resulted in an average diameter of around 10 nm with a polydispersity index (PDI) of 0.431. As incubation time was prolonged, the PDI did not significantly vary; the average diameter, however, slightly decreased to around 7 nm after 20 min and remained in that range afterwards. This indicated that QDs in initial clusters which were formed in the first 20 min interacted more strongly than and packed more tightly with time. The cluster size of 7 nm was consistent with dimeric structures. Subsequently, the role of oligonucleotide hybridisation in the process was ascertained by measuring the hydrodynamic diameter of the same one-to-one mixture with increasing temperature. Results are displayed on Figure 3. For temperatures up to 65°C, the cluster size fluctuated between 10 and 35 nm while the PDI rose to 0.510 on average. These two effects were mainly imputable to thermal agitation. Further heating, however, led to a dramatic increase in average diameter. The measured values were 41 ( $\pm 5$ ) nm at 75°C, 174 ( $\pm 15$ ) nm at 85°C and 326 ( $\pm 50$ ) nm at 90°C. It was therefore concluded that the nanoclusters dissociated when the temperature was higher than the oligonucleotides melting temperature. The QDs moved further apart but remained

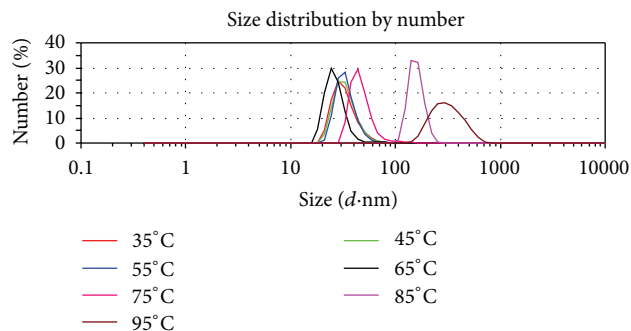


FIGURE 3: DLS measurements of a 1:1 mixture of QDs modified with complementary sequences of oligonucleotides at increasing temperatures.

grouped together as there was no mechanical agitation. Diffusion would lead over time to a reduction in measured size as QDs could eventually be seen as individual particles. The experiment also demonstrated that hybridisation was possible at physiological temperature (37°C), which is important for potential biological applications.

Having ensured the presence and hybridisation ability of complementary oligonucleotides on QD surfaces, we investigated the energy transfer processes in the nanocomposites. Three sets of donor-acceptor pairs were considered. Their full characterisation data are summarised in Table 1.

In the first pair, the donor emission and acceptor absorption perfectly overlapped which was expected to produce very efficient energy transfer. In the second case, the PL emissions were well separated which enabled good discrimination between them. In the third pair, there was near complete overlap between both absorption and emission spectra, allowing for mutual energy transfer. In each pair, the donor and acceptor were functionalised with oligonucleotide sequences complementary to each other.

Energy transfer in each donor-acceptor pair was investigated by measuring the PL emission of various donor-acceptor solutions of different compositions. The donor quenching and acceptor enhancement were plotted against the donor-to-acceptor ratio (Figures 4–6). The donor quenching is defined as the ratio of the donor intensity in the mixed solution to that of the pure donor at the same concentration. Similarly, the acceptor enhancement is defined as the ratio of the acceptor intensity in the mixed solution to that

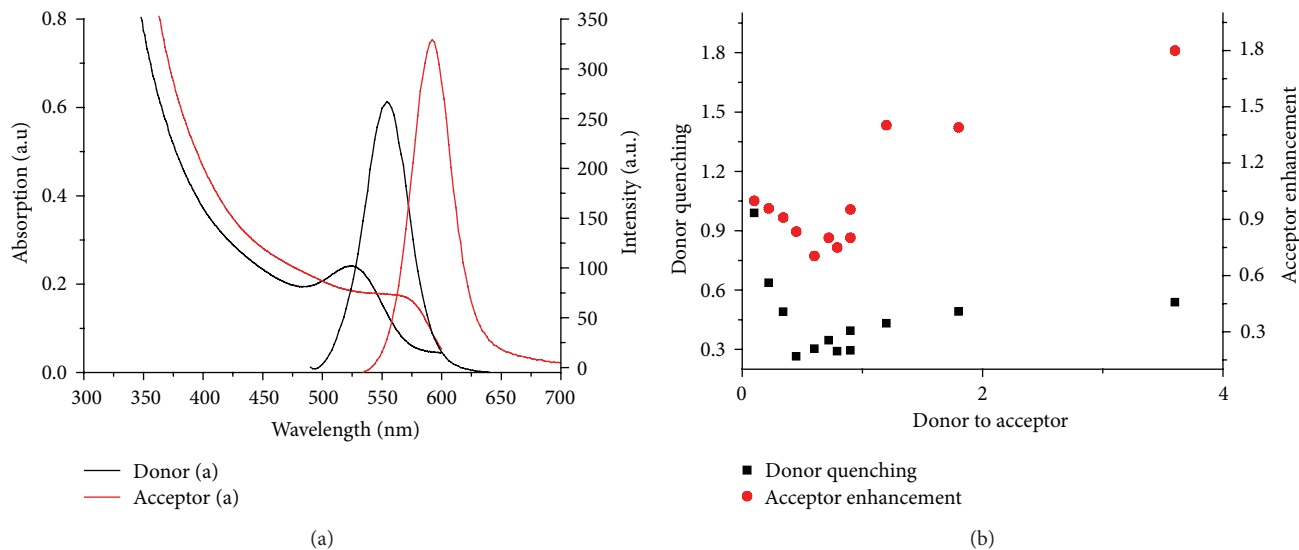


FIGURE 4: (a): Donor (a) and acceptor (a) UV-visible absorption and PL emission spectra. (b): Donor (a) quenching and acceptor (a) enhancement versus donor-to-acceptor ratio.

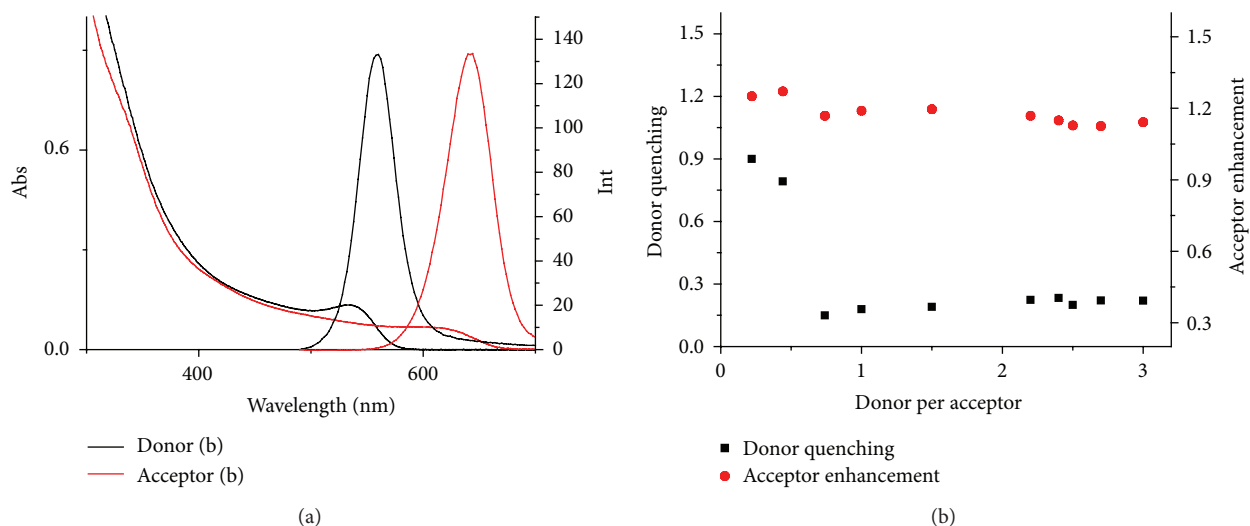


FIGURE 5: (a): Donor (b) and acceptor (b) UV-visible absorption and PL emission spectra. (b): Donor (b) quenching and acceptor (b) enhancement versus donor-to-acceptor ratio.

of the pure acceptor at the same concentration. It should be noted that donor and acceptor QDs can bind to each other in multiple configurations through oligonucleotide hybridisation and that the complementary domain is approximately 5 nm in length (15 base pairs) [46]. In Tikhomirov et al. work [17], the valency of oligonucleotide-modified QDs was measured for QDs prepared with the same method that was followed here. It was shown to depend on the length of the QD-binding domain of the oligonucleotide and the QD diameter. In our case, the QD-binding domain was a T6 tail; therefore, all QDs are estimated to have a valency of two to three for the donors and three to four for the acceptors. In the first pair (donor (a)–acceptor (a)), as shown in Figure 4, the donor was rapidly quenched for ratios up

to 0.5:1 where it reached 30% of the original value and remained stable for ratios up to 1:1. When the acceptors was in excess, all donor QDs could be assumed to bind to acceptor QDs and to be quenched by them. For these lower ratios, clusters of one donor and two or more acceptor could also form. It led to a slight degree of acceptor quenching through acceptor-to-acceptor intraensemble energy transfer due to spectral overlap of the acceptor absorption and emission. Enhancement of the acceptor PL was thus not observed as long as it was in excess. When the donor-to-acceptor ratio was further increased, the donor emission slightly recovered and plateaued at around 40% of the original value. This was attributed to the possibility of donor-to-donor energy transfer due to partial overlap of donor absorption and donor

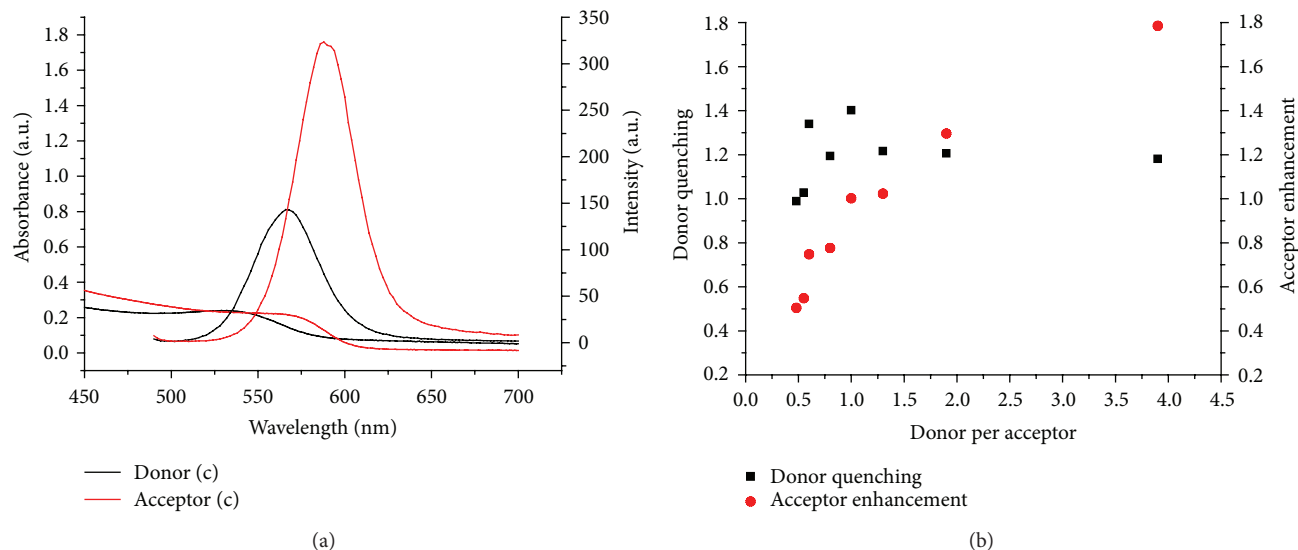


FIGURE 6: (a): Donor (c) and acceptor (c) UV-visible absorption and PL emission spectra. (b): Donor quenching (c) and acceptor enhancement (c) versus donor-to-acceptor ratio.

emission spectra [18]. Meanwhile, the acceptor emission was gradually enhanced up to 160% of its original value, thus confirming the occurrence of the energy transfer.

Considering the donor-acceptor pair (b) with well-separated absorptions and emissions, the interaction pattern appeared slightly different as presented in Figure 5. At low donor-to-acceptor ratios, a similar trend of rapid donor quenching was observed, down to around 20%. The acceptor emission, however, was immediately enhanced to 120% and remained around that level independently of the amount of donor. The high FRET efficiency at low donor-to-acceptor ratio was due to the high quantum yield of both sets of QDs, while the rapid saturation of the acceptor enhancement was attributed to the spectral separation. As more donor was added its emission slightly recovered due to donor-to-donor intraensemble energy transfer but remained below 50%.

Figure 6 shows that in the pair (c), both sets of QDs had almost completely overlapping spectra. This means that either could actually be donor or acceptor. At low donor-to-acceptor ratio, the so-called “acceptor” was quenched and the “donor” emission was enhanced. The species in excess was most likely to surround the other one through oligonucleotide hybridisation, thus transferring more energy than it received. When the ratio reached one-to-one, the “acceptor” emission had fully recovered, while the donor was still 140% of its original value. It should be noted that the “donor” had a rather low quantum yield of 6% and any energy transfer would therefore translate into a high percentage of variation. Its emission then plateaued at 120% while the acceptor emission continuously rose up to 180% as the donor-to-acceptor ratio was increased. Because of the spectral overlap, it became difficult to distinguish the donor emission at high ratio. It is therefore very likely that the donor was quenched but the emission at that particular wavelength was compensated by the acceptor.

In all cases, energy transfer was observed between QDs modified with complementary oligonucleotide sequences, and there was always a range of ratio for which one was quenched and the other was enhanced. Both donor quenching and acceptor enhancement plateaued between 3 and 4 donors per acceptor, consistently with the calculated valency of the acceptors.

To be suitable for *in vitro* FRET experiments, donor and acceptor must have well-separated emission spectra in order to be detected independently, and FRET should result in nearly full quenching of the donor and maximum enhancement of the acceptor. Only the donor-acceptor pair (b) was found to satisfy these two conditions and was therefore tested in live cell cultures. Two cultures of HT-1080 cells from human fibrosarcoma were incubated with donor (b) and acceptor (b), respectively. Both types of QDs were readily uptaken and could be observed as isolated spots in the cytoplasm, green for the donor and red for the acceptor. A third culture was then incubated with donor and acceptor simultaneously, with no prior mixing. This resulted in the partial colocalisation of donor and acceptor, but isolated green and red QDs could still be seen. Preincubation of donor and acceptor in equal concentrations for an hour and subsequent addition to the cell culture, however, resulted in the donor luminescence completely disappearing and the acceptor emission being enhanced. Thus, our QD-based donor-acceptor system clearly demonstrated fluorescent resonant energy transfer (FRET) inside live HT-1080 cells. Example confocal images of all four types of cultures are displayed in Figure 7. It was therefore concluded that preformed assemblies of QDs persisted in cell cultures but that binding did not spontaneously occur in that biological medium. The disappearance of all green emissions confirmed the occurrence of FRET in the system with near complete quenching of the donor QDs.

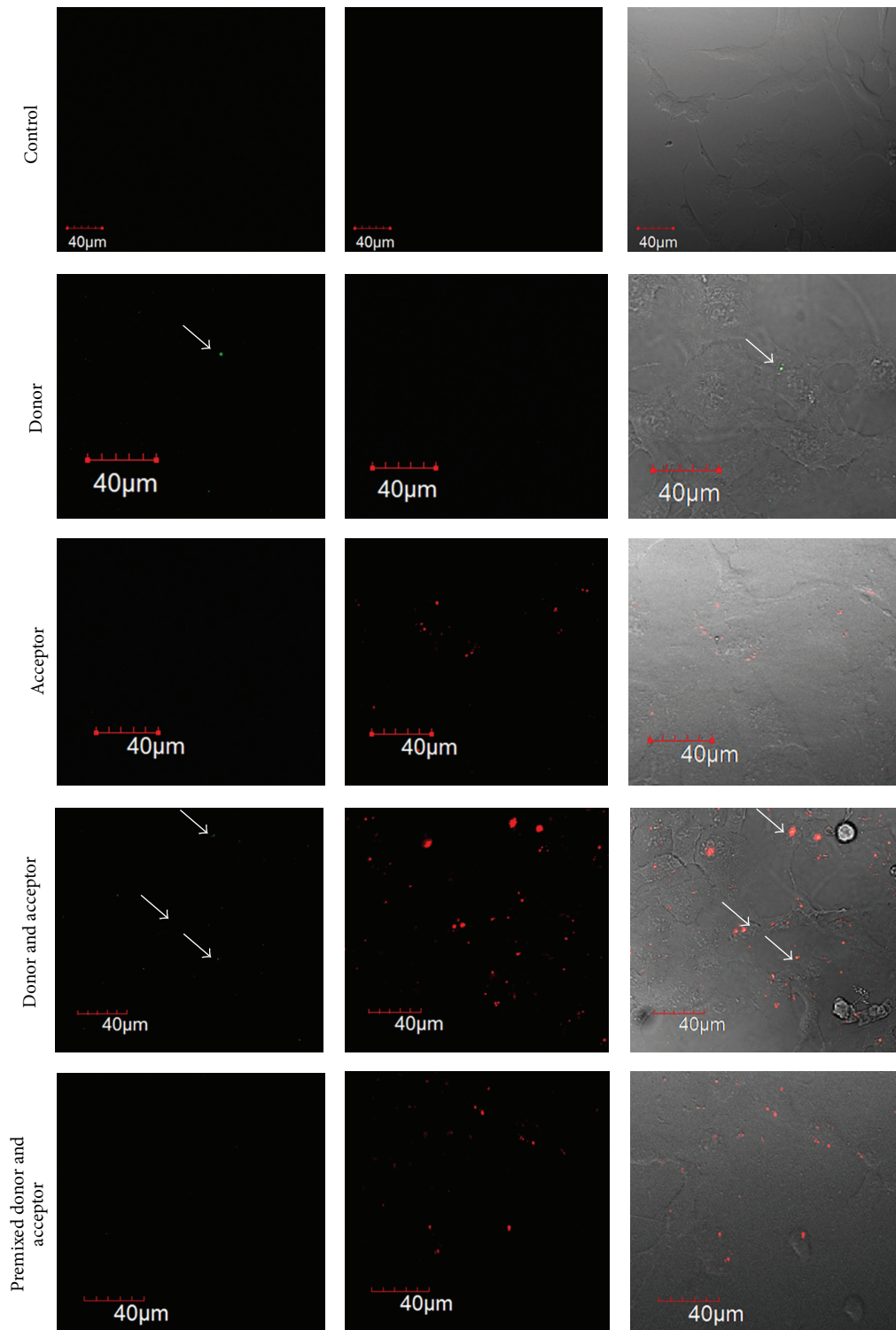


FIGURE 7: Confocal microscope images of HT-1080 cells exhibiting internalised QDs. First row: negative control; second row: donor (b); third row: acceptor (b); fourth row: donor (b) and acceptor (b) added simultaneously; fifth row: donor (b) and acceptor (b) with preincubation. First column: excitation 543 nm, emission 603 nm; second column: excitation 633 nm, emission 668 nm; third column: overlay of green and red channels with bright field. Arrows indicate green QDs.

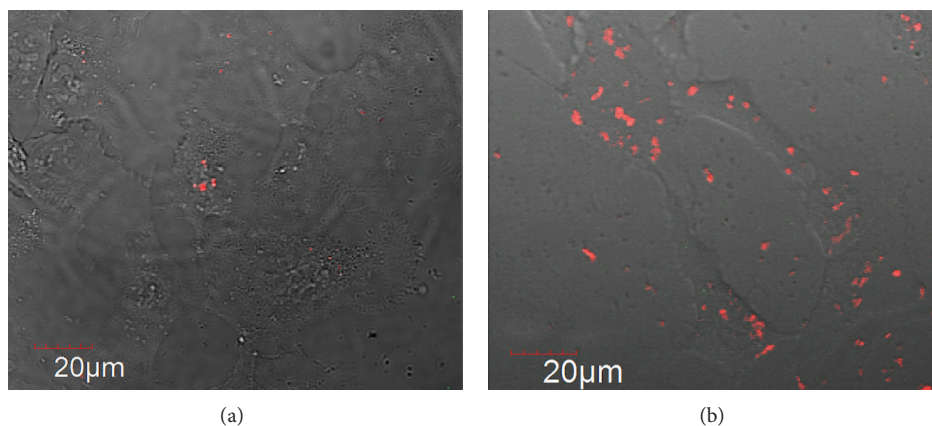


FIGURE 8: Confocal microscope close-up images of HT-1080 cells exhibiting internalised green and red QDs. (a) Without preincubation. (b) With preincubation. Overlay of green and red channels with bright field. Excitation 543 nm, emission 603 nm; excitation 633 nm, emission 668 nm.

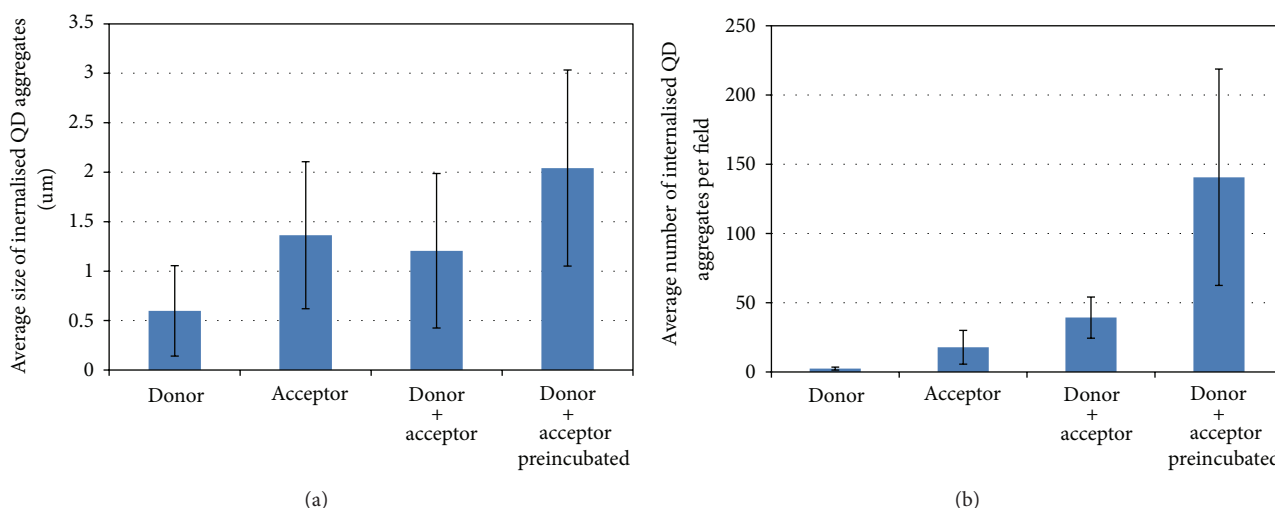


FIGURE 9: Histograms representing the number (b) and size (a) of QD aggregates internalised by cells depending on QD type: donor, acceptor, and 1:1 mixture with or without preincubation.

Prehybridisation of QDs also resulted in a higher degree of aggregation and accumulation in individual cells as illustrated in Figure 8. This was quantified by both the number and size of QD aggregates visible inside cell cytoplasm and represented in Figure 9. The overall higher internalisation was imputable to the formation of larger aggregates. Larger objects tend to be better internalised by cells due to a thermodynamically favoured attachment to the cell membrane [47].

This observation opened to another possible type of application, where DNA-hybridisation processes could be monitored through QD aggregation using a system where FRET does not occur. Similar cellular testing of the donor-acceptor pair (c) provided an example of such system. As predicted by the fluorescence titration described above, neither species was quenched at 1:1 ratio, thus allowing visualising them simultaneously in cells. The presence in cytoplasm of large aggregates containing both red and green QDs confirmed the occurrence of oligonucleotide binding

after preincubation. Confocal microscopy images of cells treated with these QDs are displayed in Figure 10.

Thus, the results above demonstrated that our composites were suitable for studying energy transfer processes or DNA binding/digesting processes in cell cultures *in vitro*.

#### 4. Conclusions

In this work, a series of new oligonucleotide-modified CdTe QDs have been prepared, characterized, and tested *in vitro*. Hybridisation and separation of complementary strands of oligonucleotides were assessed as a function of time and temperature. It was found that the hybridised systems demonstrated variable FRET efficiencies depending on spectral overlap, which could be observed *in vitro* in HT-1080 cell cultures. Further work will include an investigation of specific intracellular oligonucleotide-modified QD interactions in various cell cultures to understand and explain the biological behaviour of these nanomaterials in detail. We believe that

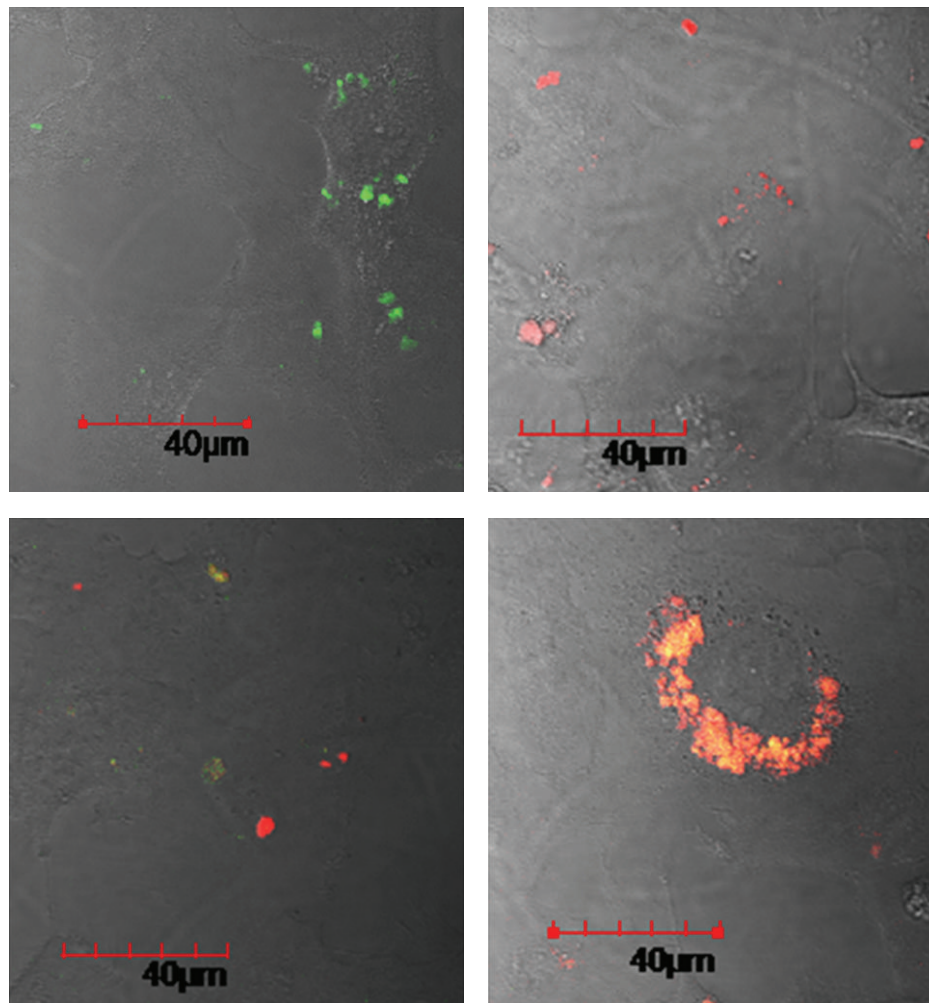


FIGURE 10: Confocal microscope images of HT-1080 cells exhibiting internalised QDs. (a) donor (c), (b) acceptor (c), (c) donor (c) + acceptor (c) added simultaneously, (D) donor (c) + acceptor (c) after a one-hour preincubation. Overlay of bright field with green and red channels.

these QD-oligonucleotide conjugates might find important applications for *in vitro* biological imaging and sensing.

## Acknowledgments

The authors acknowledge financial support from Science Foundation Ireland (Grants SFI 07/IN.1/I1862 and SFI 12/IA/1300) and the Ministry of Education and Science of the Russian Federation (Grant no. 14.B25.31.0002). E. Defrancq thanks the NanoBio program for the facilities of the synthesis platform.

## References

- [1] D. Ramadurai, D. Geerpuram, D. Alexson et al., "Electrical and optical properties of colloidal semiconductor nanocrystals in aqueous environments," *Superlattices and Microstructures*, vol. 40, no. 1, pp. 38–44, 2006.
- [2] S. J. Byrne, S. A. Corr, T. Y. Rakovich et al., "Optimisation of the synthesis and modification of CdTe quantum dots for enhanced live cell imaging," *Journal of Materials Chemistry*, vol. 16, no. 28, pp. 2896–2902, 2006.
- [3] J. Conroy, S. J. Byrne, Y. K. Gun'ko et al., "CdTe nanoparticles display tropism to core histones and histone-rich cell organelles," *Small*, vol. 4, no. 11, pp. 2006–2015, 2008.
- [4] S. J. Byrne, Y. Williams, A. Davies et al., "'Jelly dots': synthesis and cytotoxicity studies of CdTe quantum dot-gelatin nanocomposites," *Small*, vol. 3, no. 7, pp. 1152–1156, 2007.
- [5] E. Jan, S. J. Byrne, M. Cuddihy et al., "High-content screening as a universal tool for fingerprinting of cytotoxicity of nanoparticles," *ACS Nano*, vol. 2, no. 5, pp. 928–938, 2008.
- [6] S. J. Byrne, B. Le Bon, S. A. Corr et al., "Synthesis, characterisation, and biological studies of CdTe quantum dot-naproxen conjugates," *ChemMedChem*, vol. 2, no. 2, pp. 183–186, 2007.
- [7] M. J. Choi, R. Pierson, Y. Chang, H. Guo, and I. K. Kang, "Enhanced intracellular uptake of CdTe quantum dots by conjugation of oligopeptides," *Journal of Nanomaterials*, vol. 2013, Article ID 291020, 8 pages, 2013.
- [8] M. Eriksen, P. Horvath, M. A. Sorensen, S. Semsey, L. B. Oddershede, and L. Jauffred, "A novel complex: a quantum

- dot conjugated to an active T7 RNA polymerase," *Journal of Nanomaterials*, vol. 2013, Article ID 468105, 9 pages, 2013.
- [9] C. P. Liu, S. H. Cheng, N. T. Chen, and L. W. Lo, "Intra/interparticle energy transfer of luminescence nanocrystals for biomedical applications," *Journal of Nanomaterials*, vol. 2012, Article ID 706134, 9 pages, 2012.
- [10] J. Wang, S. Han, D. Ke, and R. Wang, "Semiconductor quantum dots surface modification for potential cancer diagnostic and therapeutic applications," *Journal of Nanomaterials*, vol. 2012, Article ID 129041, 8 pages, 2012.
- [11] S. Jin, Y. Hu, Z. Gu, L. Liu, and H.-C. Wu, "Application of quantum dots in biological imaging," *Journal of Nanomaterials*, vol. 2011, Article ID 834139, 13 pages, 2011.
- [12] C.-W. Peng and Y. Li, "Application of quantum dots-based biotechnology in cancer diagnosis: current status and future perspectives," *Journal of Nanomaterials*, vol. 2010, Article ID 676839, 11 pages, 2010.
- [13] K. Fujioka, N. Manabe, M. Nomura et al., "Detection of thyroid carcinoma antigen with quantum dots and monoclonal IgM antibody (JT-95) system," *Journal of Nanomaterials*, vol. 2010, Article ID 937684, 7 pages, 2010.
- [14] S. Mazumder, R. Dey, M. K. Mitra, S. Mukherjee, and G. C. Das, "Review: biofunctionalized quantum dots in biology and medicine," *Journal of Nanomaterials*, vol. 2009, Article ID 815734, 17 pages, 2009.
- [15] J. Drbohlavova, V. Adam, R. Kizek, and J. Hubalek, "Quantum dots—characterization, preparation and usage in biological systems," *International Journal of Molecular Sciences*, vol. 10, no. 2, pp. 656–673, 2009.
- [16] N. Gaponik, D. V. Talapin, A. L. Rogach et al., "Thiol-capping of CdTe nanocrystals: an alternative to organometallic synthetic routes," *Journal of Physical Chemistry B*, vol. 106, no. 29, pp. 7177–7185, 2002.
- [17] G. Tikhomirov, S. Hoogland, P. E. Lee, A. Fischer, E. H. Sargent, and S. O. Kelley, "DNA-based programming of quantum dot valency, self-assembly and luminescence," *Nature Nanotechnology*, vol. 6, no. 8, pp. 485–490, 2011.
- [18] C. Higgins, M. Lunz, A. L. Bradley et al., "Energy transfer in colloidal CdTe quantum dot nanoclusters," *Optics Express*, vol. 18, no. 24, pp. 24486–24494, 2010.
- [19] A. Gole, N. R. Jana, S. T. Selvan, and J. Y. Ying, "Langmuir-Blodgett thin films of quantum dots: synthesis, surface modification, and fluorescence resonance energy transfer (FRET) studies," *Langmuir*, vol. 24, no. 15, pp. 8181–8186, 2008.
- [20] F. Rad, A. Mohsenifar, M. Tabatabaei et al., "Detection of candidatus phytoplasma aurantifolia with a quantum dots fret-based biosensor," *Journal of Plant Pathology*, vol. 94, no. 3, pp. 525–534, 2012.
- [21] S. Sadhu, K. K. Haldar, and A. Patra, "Size dependent resonance energy transfer between semiconductor quantum dots and dye using FRET and kinetic model," *Journal of Physical Chemistry C*, vol. 114, no. 9, pp. 3891–3897, 2010.
- [22] J. E. Halpert, J. R. Tischler, G. Nair et al., "Electrostatic formation of quantum dot/J-aggregate FRET pairs in solution," *Journal of Physical Chemistry C*, vol. 113, no. 23, pp. 9986–9992, 2009.
- [23] F. Long, C. Gu, A. Z. Gu, and H. Shi, "Quantum dot/carrier-protein/haptens conjugate as a detection nanobioprobe for FRET-based immunoassay of small analytes with all-fiber microfluidic biosensing platform," *Analytical Chemistry*, vol. 84, no. 8, pp. 3646–3653, 2012.
- [24] F. Morgner, S. Stufler, D. Geißler et al., "Terbium to quantum dot FRET bioconjugates for clinical diagnostics: influence of human plasma on optical and assembly properties," *Sensors*, vol. 11, no. 10, pp. 9667–9684, 2011.
- [25] H. Safarpour, M. R. Safarnejad, M. Tabatabaei et al., "Development of a quantum dots FRET-based biosensor for efficient detection of *Polymyxa betae*," *Canadian Journal of Plant Pathology*, vol. 34, no. 4, pp. 507–515, 2012.
- [26] S. Verma, S. Kaniyankandy, and H. N. Ghosh, "Charge separation by indirect bandgap transitions in CdS/ZnSe type-II core/shell quantum dots," *Journal of Physical Chemistry C*, vol. 117, no. 21, pp. 10901–10908, 2013.
- [27] T. Ribeiro, T. J. V. Prazeres, M. Moffitt, and J. P. S. Farinha, "Enhanced photoluminescence from micellar assemblies of cadmium sulfide quantum dots and gold nanoparticles," *Journal of Physical Chemistry C*, vol. 117, no. 6, pp. 3122–3133, 2013.
- [28] M. Wojdyla, S. A. Gallagher, M. P. Moloney et al., "Picosecond to millisecond transient absorption spectroscopy of broadband emitting chiral CdSe quantum dots," *Journal of Physical Chemistry C*, vol. 116, no. 30, pp. 16226–16232, 2012.
- [29] G. Mandal, M. Bardhan, and T. Ganguly, "Occurrence of Förster resonance energy transfer between quantum dots and gold nanoparticles in the presence of a biomolecule," *Journal of Physical Chemistry C*, vol. 115, no. 43, pp. 20840–20848, 2011.
- [30] C.-H. Wang, C.-W. Chen, C.-M. Wei et al., "Resonant energy transfer between CdSe/ZnS type I and CdSe/ZnTe type II quantum dots," *Journal of Physical Chemistry C*, vol. 113, no. 35, pp. 15548–15552, 2009.
- [31] S. M. Emin, N. Sogoshi, S. Nakabayashi, T. Fujihara, and C. D. Dushkin, "Kinetics of photochromic induced energy transfer between manganese-doped zinc-selenide quantum dots and spiropyrans," *Journal of Physical Chemistry C*, vol. 113, no. 10, pp. 3998–4007, 2009.
- [32] S. A. Gallagher, S. Comby, M. Wojdyla et al., "Efficient quenching of TGA-capped CdTe quantum dot emission by a surface-coordinated europium(III) cyclen complex," *Inorganic Chemistry*, vol. 52, no. 8, pp. 4133–4135, 2013.
- [33] P. R. Selvin, "The renaissance of fluorescence resonance energy transfer," *Nature Structural Biology*, vol. 7, no. 9, pp. 730–734, 2000.
- [34] N. T. Chen, S. H. Cheng, C. P. Liu et al., "Recent advances in nanoparticle-based Förster resonance energy transfer for biosensing, molecular imaging and drug release profiling," *International Journal of Molecular Sciences*, vol. 13, no. 12, pp. 16598–16623, 2012.
- [35] Z. Xia and J. Rao, "Biosensing and imaging based on bioluminescence resonance energy transfer," *Current Opinion in Biotechnology*, vol. 20, no. 1, pp. 37–44, 2009.
- [36] D. Geissler, S. Stufler, H. G. Lohmannsroben, and N. Hildebrandt, "Six-color time-resolved Förster resonance energy transfer for ultrasensitive multiplexed biosensing," *Journal of the American Chemical Society*, vol. 135, no. 3, pp. 1102–1109, 2013.
- [37] R. Freeman, J. Girsh, B. Willner, and I. Willner, "Sensing and biosensing with semiconductor quantum dots," *Israel Journal of Chemistry*, vol. 52, no. 11-12, pp. 1125–1136, 2012.
- [38] E. Petryayeva and U. J. Krull, "Quantum dot and gold nanoparticle immobilization for biosensing applications using multidentate imidazole surface ligands," *Langmuir*, vol. 28, no. 39, pp. 13943–13951, 2012.
- [39] W. R. Algar, D. Wegner, A. L. Huston et al., "Quantum dots as simultaneous acceptors and donors in time-gated Förster resonance energy transfer relays: characterization and biosensing,"

- Journal of the American Chemical Society*, vol. 134, no. 3, pp. 1876–1891, 2012.
- [40] C. H. Vannoy, A. J. Tavares, M. O. Noor, U. Uddayasankar, and U. J. Krull, “Biosensing with quantum dots: a microfluidic approach,” *Sensors*, vol. 11, no. 10, pp. 9732–9763, 2011.
- [41] W. Zhong, “Nanomaterials in fluorescence-based biosensing,” *Analytical and Bioanalytical Chemistry*, vol. 394, no. 1, pp. 47–59, 2009.
- [42] V. A. Gérard, Y. K. Gun’ko, E. Defrancq, and A. O. Govorov, “Plasmon-induced CD response of oligonucleotide-conjugated metal nanoparticles,” *Chemical Communications*, vol. 47, no. 26, pp. 7383–7385, 2011.
- [43] M. P. Moloney, Y. K. Gun’ko, and J. M. Kelly, “Chiral highly luminescent CdS quantum dots,” *Chemical Communications*, no. 38, pp. 3900–3902, 2007.
- [44] S. A. Gallagher, M. P. Moloney, M. Wojdyla, S. J. Quinn, J. M. Kelly, and Y. K. Gun’ko, “Synthesis and spectroscopic studies of chiral CdSe quantum dots,” *Journal of Materials Chemistry*, vol. 20, no. 38, pp. 8350–8355, 2010.
- [45] S. D. Elliott, M. P. Moloney, and Y. K. Gun’ko, “Chiral shells and achiral cores in CdS quantum dots,” *Nano Letters*, vol. 8, no. 8, pp. 2452–2457, 2008.
- [46] C. Rivetti and S. Codeluppi, “Accurate length determination of DNA molecules visualized by atomic force microscopy: evidence for a partial B- to A-form transition on mica,” *Ultramicroscopy*, vol. 87, no. 1-2, pp. 55–66, 2001.
- [47] X. Li, “Size and shape effects on receptor-mediated endocytosis of nanoparticles,” *Journal of Applied Physics*, vol. 111, no. 2, Article ID 024702, 4 pages, 2012.

## Review Article

# Core-Shell Structure in Doped Inorganic Nanoparticles: Approaches for Optimizing Luminescence Properties

**Dini Xie, Hongshang Peng, Shihua Huang, and Fangtian You**

*Key Laboratory of Luminescence and Optical Information, Ministry of Education, Institute of Optoelectronic Technology, Beijing Jiaotong University, Beijing 100044, China*

Correspondence should be addressed to Hongshang Peng; [hshpeng@bjtu.edu.cn](mailto:hshpeng@bjtu.edu.cn)

Received 10 May 2013; Revised 2 July 2013; Accepted 18 August 2013

Academic Editor: Pathik Kumbhakar

Copyright © 2013 Dini Xie et al. This is an open access article distributed under the Creative Commons Attribution License, which permits unrestricted use, distribution, and reproduction in any medium, provided the original work is properly cited.

Doped inorganic luminescent nanoparticles (NPs) have been widely used in both research and application fields due to their distinctive properties. However, there is an urgent demand to improve their luminescence efficiency, which is greatly reduced by surface effects. In this paper, we review recent advances in optimizing luminescence properties of doped NPs based on core-shell structure, which are basically classified into two categories: one is by use of surface coating with nonmetal materials to weaken the influence of surface effect and the other is with metal shell via metal enhanced luminescence. Different materials used to coat NPs are surveyed, and their advantages and disadvantages are both commented on. Moreover, problems in current core-shell structured luminescent NPs are pointed out and strategies furthering the optimization of luminescence properties are suggested.

## 1. Introduction

With the development of nanoscience and nanotechnology, more and more researches focus on core-shell nanostructures. A statistical data analysis is presented in Figure 1 to show an accelerated increase of published SCI papers on the theme of “core-shell nanoparticles.” One motivation of using core-shell nanostructures is to achieve multiple functions. Usually, NPs have limited functions owing to the inherent property of constituted materials. Combining two or more kinds of materials into one particle, in the form of core-shell structure, is an effective way to address this issue. For instance, magnetic-luminescent bifunctional nanocomposites can be formed by coating magnetic NPs with a layer of luminescent material as a shell [1–7]. When magnetic NPs are surface modified by a layer of catalytic material, magnetic-catalytic core-shell NPs are obtained [8–16].

Another important motivation of utilizing core-shell nanostructure is to improve properties of NPs, such as luminescence efficiency. There are mainly two directions in

enhancing luminescence properties of nanomaterial: inhibit the negative factors and promote the positive factors.

A great deal of studies including ours has demonstrated that luminescence efficiency and lifetime of materials will be greatly reduced compared with the bulk ones when their size is reduced to nanoscale [17–20]. This is usually ascribed to large surface area of nanomaterials, unsaturated bonds on the surface or high surface energy, which are prone to quench the luminescence of emission centers on or near the surface [21–24]. In view of this, surface coating in the form of a core-shell structure may efficiently eliminate these negative influences of surface effect on luminescence of doped NPs. On the other hand, radiative transition rate and excitation efficiency of luminescent species will be increased when the distance between luminescent species and noble metal is within a certain range [25, 26]. Therefore, luminescent properties of doped NPs can be ameliorated via metal enhanced luminescence if a metal shell is coated around NPs.

This review mainly focuses on recent development of approaches for optimizing luminescence properties of inorganic doped NPs through core-shell structures.

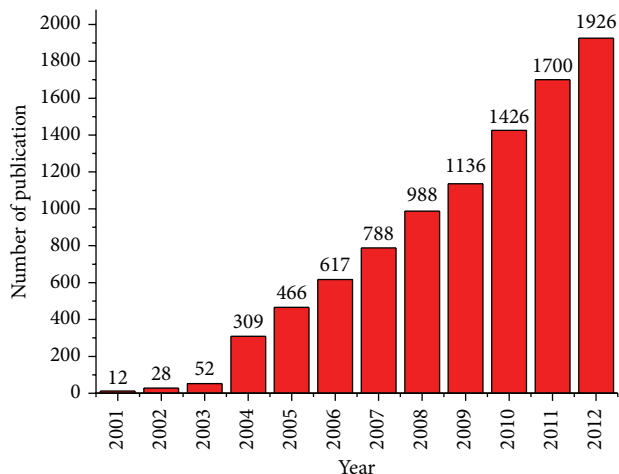


FIGURE 1: Publications per year for core-shell NPs during the period 2001 to 2012. The data was collected from Web of Science Database, using the keyword “core-shell nanoparticles” in the theme.

## 2. Core-Shell Structure to Weaken Surface Effect

For doped NPs, because of their limited sizes, sites occupied by doped ions can no more be considered as equivalent [27]. In NPs, therefore, inhomogeneous linewidth gets broader [28], originally degenerated energy levels may split [22], and selection rules may be loosened. Variations in the position of spectral lines and branching ratios can be observed with selective excitation [29]. Defects and disorders related to breakage of lattice periodicity on the large surface area of nanomaterials may introduce local electronic states into band gap, acting as traps for excitation. Besides, unsaturated bonds on surface render the particle surface very active, so that light ions and radicals may be adsorbed and attached onto the surface. Ions coupled with them would have high multiphonon relaxation rate and act also as traps. In many cases, surface provides an additional quench path for the luminescence of ion centers in NPs, resulting in fast decay and low quantum efficiency (QE) [30].

Wang et al. [31] presented direct evidence of surface quenching effect associated with size-dependent luminescence of upconversion (UC) NPs. The influence of surface quenching on decay curve and QE of ion centers in NPs was discussed by Huang and You [32], considering energy transfer between doped ions and surface quench centers. QE and decay curve under nonselective excitation were calculated numerically by integrating over the sample. Surface effect of nanophosphors was studied by time-resolved spectroscopy by Tian et al. [33], who suggested that surface quenching effects could be negligible when luminescence centers were more than 7 nm away from the surface.

For nondoped quantum dots (QDs), there are similar surface effects. Chou et al. [34] demonstrated that organic molecules on the surface of CdS QDs largely decreased photoluminescence (PL) quantum yield (QY) based on density function theory computation. They proposed that

the interactions between capping molecules and CdS QDs might be attributed to functional groups and CdS clusters.

Core-shell structure is an effective way to weaken surface effect of NPs. According to the nature of adopted core material to that of shell material, core-shell nanostructures are approximately separated into “homogeneous” or “heterogeneous” in this review, corresponding to the same or different materials, respectively.

### 2.1. Heterogeneous Core-Shell Nanostructures

**2.1.1. Silica Coating.** For heterogeneous core-shell nanostructures, the shell can be classified into two categories: silica or nonsilica. Silica has the attributes of good biocompatibility, water solubility, and synthesis, hence, are widely used to coat NPs. Silica can withstand a high annealing temperature, which is helpful to enhance the crystalline of luminescent materials. Moreover, the thickness of silica shell can enlarge the distance between doped ions and surface quenching centers. Therefore, PL properties of doped NPs can be greatly enhanced through the decrease of nonradiative transition after silica coating.

Doped QDs were silica coated by microemulsion or precipitation method [35, 36]. Compared to uncoated ZnS:Mn NPs, silica-coated ZnS:Mn NPs had improved PL intensity as well as good photostability. Rare-earth (RE) doped vanadate could be silica coated by Stöber method [37]. A remarkable luminescence enhancement up to 2.17 times was observed in colloidal  $\text{YVO}_4:\text{Eu}@\text{SiO}_2$  nanocrystals (NCs), compared to that of bare  $\text{YVO}_4:\text{Eu}$  NCs. A significant improvement of luminescence intensity was also observed in  $\text{LaF}_3:\text{Nd}^{3+}@\text{SiO}_2$  core-shell NPs [38]. The phenomenon was additionally ascribed to the change of environment of  $\text{LaF}_3:\text{Nd}^{3+}$  core imposed by the silica shell.

A series of  $\text{Y}_2\text{O}_3:\text{Eu}^{3+}@\text{SiO}_2$  with different silica-coating thicknesses were synthesized by Liu et al. [39]. It was interesting to find that the silica shell not only changed the luminescence intensity of NPs but also led to the redistribution of  ${}^5\text{D}_0\text{-}{}^7\text{F}_j$  branch ratios under  ${}^7\text{F}_j\text{-}{}^5\text{D}_2$  excitation. The increased intensity ratio of  ${}^5\text{D}_0\text{-}{}^7\text{F}_2$  to  ${}^5\text{D}_0\text{-}{}^7\text{F}_j$  ( $j \neq 2$ ) was attributed to the thickening of silica shell, which decreased excitation power density and suppressed reabsorption. The variation of the effective refractive index of the core-shell composites led to the increase of lifetime with shell thickness, while the reduced reabsorption process decreased the lifetime. Therefore, an optimum lifetime appeared as a function of shell thickness.

RE-doped UC NPs is another type of important luminescent NPs largely due to their biological applications with near-infrared (NIR) radiation [40]. The developed core-shell UC NPs are attractive due to their excellent photostability, highly efficient luminescence, and low toxicity with biocompatible shell material. UC luminescence intensity of silica-coated  $\text{NdF}_3$  was reported to about 1.6 times of bare  $\text{NdF}_3$  NPs [41], and the effect of coating on the UC luminescence intensity in RE-doped  $\text{NaYF}_4$  UCNCs was strongly dependent on the volume ratio of the core and shell [42, 43]. In another work, Lü et al. [44] presented that the UC luminescence intensity

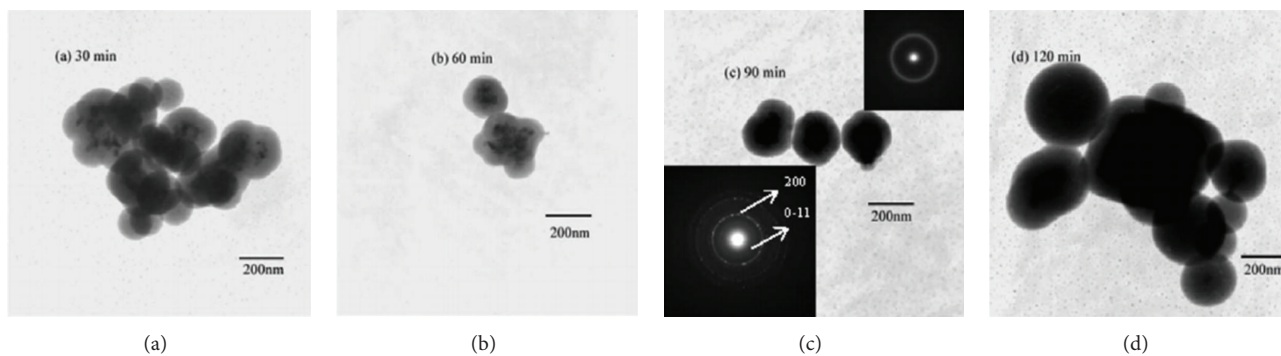


FIGURE 2: Transmission electron microscopy (TEM) photographs of silica-coated  $\text{Y}_2\text{O}_3:\text{Tm}^{3+}, \text{Yb}^{3+}$  NPs for the sintering time of 60 min and the coating time of 30 min (a), 60 min (b), 90 min (c), and 120 min (d), respectively. The upper inset (c) shows the electron diffraction (ED) pattern of noncrystalline silica shells and the lower inset is the corresponding ED pattern of crystalline  $\text{Y}_2\text{O}_3:\text{Tm}^{3+}, \text{Yb}^{3+}$  core [44]. Copyright 2008 American Institute of Physics.

of  $\text{Y}_2\text{O}_3:\text{Tm}^{3+}, \text{Yb}^{3+}$  NPs was also enhanced with the core-shell structures. Comparing with the UC luminescence intensity of bare NPs, the UC luminescence intensities of silica-coated NPs with the sintering time of 60 min and the coating time of 30, 60, 90, and 120 min were enhanced by 1.53, 1.54, 1.40, and 1.16 times, respectively (Figure 2). According to the relative variable ratios of the UC luminescence intensities of silica-coated NPs, a competitive process between two mechanisms was proposed. One mechanism was the role conversion of RE ions on the surface of NPs from the dormant state to the activated state owing to complementary ligand fields from noncrystalline silica shells. The other mechanism was the absorption effects of the shells on incident pump light and the reabsorption effects on the UC luminescence. The role conversion of lanthanide ions was prevailing in thin shelled NPs, whereas the absorption and the reabsorption effects became predominant when a thicker silica shell is coated. Hence, an optimal thickness of silica shell was possible to achieve the maximum UC luminescence.

Although silica has been utilized to coat a variety of doped luminescent NPs, it has an inherent shortcoming: a large lattice mismatch commonly exists between amorphous silica shell and particle core. The consequent interface defects may give rise to additional luminescence quenching. Thus, a preferable core-shell structure to inhibit surface effects should be better lattice matched.

**2.1.2. Nonsilica Coating.** Zhu et al. [45] reported that  $\text{YVO}_4:\text{Eu}^{3+}@\text{YBO}_3$  core-shell heteronanostructures exhibited much stronger PL than  $\text{YVO}_4:\text{Eu}^{3+}$  NCs under the same conditions. Shell ratio (SR) is the molar percentage of the shell material in the core-shell heteronanostructures, which is a critical factor in PL enhancement. The heteronanostructures exhibited the highest PL efficiency when  $\text{SR} = 1/7$ , whose PL intensity was 27% higher than that of the  $\text{YVO}_4:\text{Eu}^{3+}$  NCs. When  $\text{SR} < 1/7$ , PL intensity increased with increasing SR. This was because the surface recombination, surface defects density and surface state density of  $\text{YVO}_4:\text{Eu}^{3+}$  NCs reduced with increasing the  $\text{YBO}_3$  coating. When  $\text{SR} > 1/7$ , PL intensity decreased with increasing molar percentage of

the nonluminescent shell material. Lin et al. [46–48] prepared  $\text{CeF}_3$ ,  $\text{CeF}_3:\text{Tb}^{3+}$ , and  $\text{CeF}_3:\text{Tb}^{3+}@\text{LaF}_3$  core-shell NPs which show characteristic emission of  $\text{Ce}^{3+}$  (5d-4f) and  $\text{Tb}^{3+}$  (f-f) respectively. When the  $\text{CeF}_3:\text{Tb}^{3+}$  NPs were coated with the  $\text{LaF}_3$  shells, the emission intensity was improved by 28% with respect to that of  $\text{CeF}_3:\text{Tb}^{3+}$  core NPs. The energy-loss processes on the surface luminescence centers could be significantly decreased by the  $\text{LaF}_3$  shell which provided a barrier for energy migration to the outer surface of the shell, and thus the luminescence intensity and lifetime of the core-shell NPs were greatly enhanced. Boyer et al. [49] synthesized  $\text{NaGdF}_4:\text{Tb}^{3+}, \text{Ce}^{3+}@\text{NaYF}_4$  NPs that formed colloidal solutions in nonpolar organic solvents and showed green luminescence under ultraviolet (UV) excitation. Core-shell NPs demonstrated higher QY (~30%) under UV light and greater resistance to cerium oxidation when compared to the core-only NPs.

Kömpe et al. [50] obtained  $\text{CePO}_4:\text{Tb}@\text{LaPO}_4$  core-shell NPs with a total QY of 80%, which was quite close to the value of the bulk material. Further recommendations of enhancing QY of NPs included optimizing the thickness of the shell and employing metal salts of extremely high purity. Another work showed that the luminescence properties of  $\text{Ce}^{3+}$  and  $\text{Tb}^{3+}$  ions in doped  $\text{CePO}_4$  and  $\text{LaPO}_4$  core and core-shell NPs did not only differ with respect to their QYs [51]. The  $\text{Ce}^{3+}$  emission in core NPs was red-shifted compared to core-shell particles. Energy transfer from excited states in volume sites to surface sites was responsible for this observation.

A strong linear dependence of the  $\text{NaGdF}_4$  shell thickness on the optical response of the hexagonal  $\text{NaYF}_4:\text{Yb}, \text{Er}@\text{NaGdF}_4$  core-shell UCNCs had been presented by Zhang et al. [52]. During growth of the  $\text{NaGdF}_4$  shells, surface defects of the NCs could be gradually passivated by the shell deposition process, which resulted in the obvious enhancement of the overall UC emission intensity and lifetime and more resistant to quenching by water molecules. Another work reported that  $\text{NaGdF}_4:\text{Yb}, \text{Er}@\text{NaYF}_4$  core-shell NPs with narrow size distribution ( $\sigma < 10\%$ ) were prepared by one pot successive layer-by-layer (SLBL) strategy [53]. Shell thickness of

the obtained NPs could be well controlled from 1 monolayer (ML) ( $\sim 0.36$  nm) to more than 20 ML ( $\sim 8$  nm) by simply tuning the amounts of shell precursors, which resulted in the significant improving on UC luminescence efficiency (up to  $0.51 \pm 0.08\%$ ) and stability (more resistant to quenching by water). It was important to note that nearly 30% luminescence was quenched by water even after over coated with a 16 ML ( $\sim 5.5$  nm) shell. It was assumed that the high-energy stretching vibration of the water molecule could be regarded as a surface oscillator. The interaction between this oscillator and the luminescence center (lanthanide ions) might also be realized without contacting. It meant that the luminescence could be quenched by water with the noncontacting way, which was somewhat like the fluorescence resonance energy transfer (FRET). Chen et al. [54] reported novel  $\alpha$ -(NaYbF<sub>4</sub>:0.5%Tm<sup>3+</sup>)@CaF<sub>2</sub> core-shell NPs with efficient NIR<sub>in</sub>-NIR<sub>out</sub> UC PL and their applications for high-contrast in vitro and deep tissue bioimaging. An epitaxial CaF<sub>2</sub> heteroshell increased the intensity of UC PL from  $\alpha$ -NaYbF<sub>4</sub>:0.5%Tm<sup>3+</sup> NPs 35 times. The QY of NIR UC PL in the  $\alpha$ -(NaYbF<sub>4</sub>:0.5%Tm<sup>3+</sup>)@CaF<sub>2</sub> core-shell NPs was measured to be  $0.60 \pm 0.1\%$  under low-energy excitation of  $0.3$  W/cm<sup>2</sup>.

Core-shell nanostructures with improved luminescence properties have been widely applied in various fields. For more examples and detailed informations on applications of different core-shell NPs, readers are referred to some other excellent reviews by Kalele et al. [55], Selvan et al. [56], Wang et al. [40], and so forth.

**2.2. Homogeneous Core-Shell Nanostructures.** Homogeneous core-shell nanostructures usually refer to doped core-shell nanostructures which adopt the same matrix material for the core and shell, containing dopant ions in the core, while the shell is pure matrix material or doped with other ions. The advantage of homogeneous core-shell nanostructure is the following. There is almost no problem of lattice mismatch between the core and shell, so that there will be fewer defects and quenching centers on the interfaces. In addition, since the shell and core have the same matrix, the shell is possible to transfer energy to the dopant ions in the vicinity of the surface of the core, and the overall absorption and emission intensity will be improved.

Quan et al. [57] observed a 30% PL intensity enhancement in ZnS:Mn@ZnS core-shell NCs comparing with bare ZnS:Mn, which was ascribed to the elimination of the surface defects. Q. Xiao and C. Xiao [58] also reported a similar phenomenon and conclusion in ZnS:Mn@ZnS core-shell NPs. Cao et al. [59] demonstrated that Mn<sup>2+</sup> emission at 580 nm in the ZnS:Mn@ZnS core-shell NPs was seven times stronger than that in the uncoated ZnS:Mn. Their experiment results indicated that both ZnS shell and UV light treatment (samples are exposed to the irradiation of a UV lamp [60, 61]) could passivate nanoparticle surface, remove nonradiative relaxation paths, and thus enhance the overall luminescence quantum yield of uncoated ZnS:Mn. However, UV light treatment could only enhance the luminescence in the uncoated ZnS:Mn NPs but led to no luminescence

enhancement in the coated ones. Some calculations indicated that Mn<sup>2+</sup> ions were not randomly distributed in the particle but preferred to occupy the sites close to the surface. This may be related to the "self-purification" process of nanomaterials [62], whereby Mn<sup>2+</sup> has a tendency to be expelled to the nanoparticle surface [63]. Jiang et al. [64] studied the shell thickness dependence of luminescence intensity in core-shell ZnS:Mn@ZnS NPs. As the ZnS shell on the ZnS:Mn NPs thickened, an increase in the intensity of Mn<sup>2+</sup> emission followed by a steady decline could be observed. The concentration of the luminescence center gradually decreased with shell thickening, which would consequently contribute a reducing effect to the emission intensity.

Qu et al. [65] synthesized LaF<sub>3</sub>:Yb<sup>3+</sup>,Er<sup>3+</sup>@LaF<sub>3</sub> which showed improvement in both the UC emission intensity and the lifetime. The enhancement could be attributed to the LaF<sub>3</sub> shell which could eliminate the nonradiative centers on the surface of LaF<sub>3</sub>:Yb<sup>3+</sup>,Er<sup>3+</sup> NCs. Qian et al. [66] increased the emission intensity of NaYF<sub>4</sub>:Yb,Er@silica core-shell NPs by depositing an undoped NaYF<sub>4</sub> shell on the NaYF<sub>4</sub>:Yb,Er NPs before the silica coating (Figure 3). The total emission intensity of NaYF<sub>4</sub>:Yb,Er@NaYF<sub>4</sub>@silica core-shell NPs increased by 15 times compared to that without the intermediate NaYF<sub>4</sub> shell. The critical shell thickness of NaYF<sub>4</sub> was  $\sim 3$  nm, beyond which no further emission intensity enhancement was observed.

Yi et al. [67] reported a significant UC luminescence enhancement after growing YOF shell on the surface of YOF:Yb,Er core. They observed that the YOF shell enhanced the red emission band at  $\sim 669$  nm but suppressed the green emission band at  $\sim 540$  nm. The emission intensity at  $\sim 669$  nm was increased by  $\sim 18.5$  times after coating. A steady increase in the red/green emissions (R/G) ratio was observed during the growth of the NPs, which was due to host (matrix) effect of YOF.

In a sensitizer-activator UC system containing both sensitizer ions and activator ions [68], sensitizer ions could also be doped in the shell to make additional enhancement of UC luminescence. Vetrone et al. [69] demonstrated the synthesis of a novel NaGdF<sub>4</sub>:Yb,Er@NaGdF<sub>4</sub>:Yb active-core@active-shell architecture with great enhancement of UC luminescence. Yang et al. [70] also reported the synthesis of BaGdF<sub>5</sub>:Yb,Er@BaGdF<sub>5</sub>:Yb active-core@active-shell structured UCNCs with a controllable size from 3 to 10 nm. It was found that after coating, the active shell with altered concentrations of Yb<sup>3+</sup> ions in the shell, the luminescence intensity can be improved several hundred times. In contrast to the inert-shell-coated NPs, the main difference is that the active shell not only protects the luminescent ions from the nonradiative decay but also transfers absorbed radiation to the luminescent core.

Chen et al. [71] reported NaGdF<sub>4</sub>:Nd@NaGdF<sub>4</sub> core-shell near-infrared downconversion NPs with an average size of 15 nm and exceptionally high PL QY. The fact that both the excitation and PL of these NCs were in the biological window of optical transparency, combined with their high QE, spectral sharpness, and photostability, made them quite promising as optical biomaging probes.

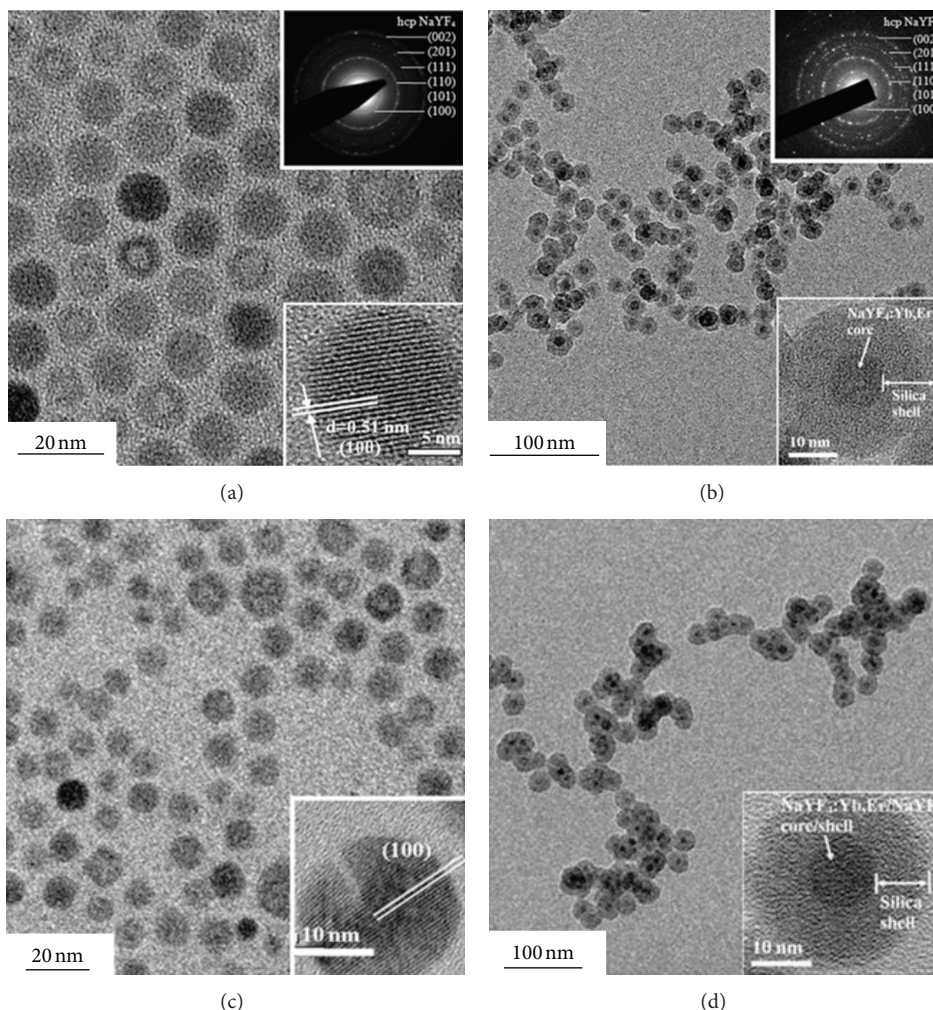


FIGURE 3: TEM images and HRTEM images (bottom inset) of (a) the  $\text{NaYF}_4:\text{Yb,Er}$  NPs, (b) the  $\text{NaYF}_4:\text{Yb,Er}@silica$  NPs, (c) the  $\text{NaYF}_4:\text{Yb,Er}@NaYF_4$  NPs, and (d) the  $\text{NaYF}_4:\text{Yb,Er}@NaYF_4@silica$  NPs. Diffraction patterns (top inset) of (a) the  $\text{NaYF}_4:\text{Yb,Er}$  NPs and (b) the  $\text{NaYF}_4:\text{Yb,Er}@silica$  NPs [66]. Copyright 2009 Materials Research Society.

**2.3. The Possible Problem: Atom/Ion Diffusion in Core-Shell Nanostructures.** As we see, most of the researches of core-shell nanomaterials concentrate on the method of preparing core-shell structures and the improved luminescence properties, but little attention has been devoted to the diffusion of doped ions in the core-shell nanomaterials. Ningthoujam et al. [72] presented the possibility of  $\text{Eu}^{3+}$  diffusion in  $\text{YVO}_4:\text{Eu}^{3+}@YVO_4$  core-shell NPs. In this work,  $\text{YVO}_4:\text{Eu}^{3+}$  NPs and  $\text{YVO}_4:\text{Eu}^{3+}@YVO_4$  core-shell NPs were prepared and heat treated from 500 to 900°C. Surface inhomogeneities around  $\text{Eu}^{3+}$  present on the surface of the  $\text{YVO}_4:\text{Eu}^{3+}$  core could be removed effectively by the undoped  $\text{YVO}_4$  shell and resulted in improved luminescence from core-shell NPs compared to the core NPs. Another reason of luminescence improvement could be that a small fraction of  $\text{Eu}^{3+}$  ions available on the surface of the core migrated into the  $\text{YVO}_4$  shell and led to the increase of  $\text{Eu}^{3+}$ - $\text{Eu}^{3+}$  distance and hence, reduced the extent of concentration quenching.

In view of this, the temperature of ions' diffusion and its influences on properties of core-shell nanomaterials should be investigated in order to achieve best luminescence properties. DiMaio et al. [73] studied the diffusion of  $\text{Eu}^{3+}$  ions in  $\text{LaF}_3:\text{Eu}^{3+}@LaF_3$  core-shell NPs under 650°C. At elevated temperatures, the diffusion of doped ions was significant enough to result in drastic color changes as emissions from higher-energy manifolds were no longer concentration quenched. In another work, Zheng et al. [74] observed  $\text{Mn}^{2+}$  diffusion in  $\text{MnS}@ZnS$  core-shell NCs annealed at relatively lower temperatures (220–300°C). The diffusion of  $\text{Mn}^{2+}$  in  $\text{MnS}@ZnS$  NCs from the  $\text{MnS}$  core to the nanocrystal surface resulted in the PL surface quenching. Therefore, highly efficient luminescent NCs could be obtained by growing a thin  $\text{ZnS}$  shell on a small-sized  $\text{MnS}$  core at low temperature, annealing the resulting NCs for effectively diffusing  $\text{Mn}^{2+}$  into the  $\text{ZnS}$  shell at high temperature to form a  $\text{ZnS}:\text{Mn}$  diffusion layer, and overcoating a thicker  $\text{ZnS}$  shell as a passivating layer.

In a word, atom/ion diffusion should be concerned in the design and construction of core-shell nanostructures, especially when high temperature is required. If doped ions in particle core diffuse across shell to surface, then surface effect cannot be prevented any more and surface quenching of luminescence still remains.

### 3. Core-Shell Structure to Achieve Metal Enhanced Luminescence

The luminescence QE is given by  $QE = k_r / (k_r + k_{nr})$ , where  $k_r$  is the radiative transition rate, and  $k_{nr}$  is the nonradiative transition rate. As aforementioned, core-shell structure can weaken the surface effect and thus reduce nonradiative transition rate, and ultimately improve the effective QE. In addition, enhancement of QE can also be expected if the radiative transition rate is increased, based on the above QE equation.

In 1960s, Strickler and Berg [75] discovered that the vibration dipole radiative decay rate increased as the increase of the refractive index of medium, and Strickler-Berg equation was given to describe the relationship of the two parameters, which indicated that placing luminescent species near the metal surface could be an effective way of improving sensitivity of luminescence detection. In the later 1970s, Drexhage approved that luminescent species distribution close to the surface of a metal such as gold and silver of their luminescent emission intensity was greatly increased compared to the free state luminescent emission intensity [76, 77], and a theoretical explanation was given [78, 79]. The laboratory led by Professor Lakowics of the University of Maryland studied this particular phenomenon of luminescence enhanced effect from both theoretical and experimental aspects and applied it in the field of biosensing and biomedical [80–84]. Metal enhanced luminescence (MEL) is a through-space effect. That is, there would be enhanced luminescence only if there is a certain distance between the luminescent species to the metal surface. The energy of luminescent species under the excited state will transfer to the matrix in the form of nonradiative transition when the distance is below 5 nm. The extent of quenching effect is inversely proportional to the cube of the distance [85]. The radiative transition rate of the luminescent species will rise when the distance is 5–20 nm [25]. This will result in the enhancement of QY, which is more prominent in the low QY luminescent species. In this distance, the enhancement of surface local electromagnetic field activates molecules close to the metal surface and leads to promotion of excitation efficiency, which is also beneficial to enhancement of luminescence QY. Mechanisms of MEL were summarized by Geddes and Lakowicz [26].

The metal-fluorophore interactions result in an increase in the quantum yield (i.e., emission intensity) of the fluorophore and a decrease in the lifetime of fluorophores owing to two phenomena: an enhanced local electric field and an increase in the intrinsic system decay rate. The first factor provides stronger excitation rates but does not modify the fluorescence lifetime of the molecules. The second factor increases the net nanoparticle quantum yield. Excellent

demonstrations of MEL was made by Aslan et al. [86–88], who reported that by growing a layer of silica shell with fluorophores embedded within it on the nanoparticle of Ag, the emission intensity was about 20-fold larger than that of the nanobubbles without Ag core. Zeng et al. [89] also designed Au@SiO<sub>2</sub> core-shell NPs to enhance the efficiency of FRET based on QDs and R-phycoerythrin (RPE) in solution. Li et al. [90] synthesized carbon dots adsorbed Ag@SiO<sub>2</sub> core-shell NPs and obtained a more than four-fold increase of luminescence intensity of carbon dots.

As we mentioned before, there would be enhanced luminescence only if there is a certain distance between the luminescent species to the metal surface. Thus, the thickness of the spacer between the luminescent species and the metal is a critical parameter for the achievement of MEL. Zhang et al. [91] systematically increased the silica spacer thickness to optimize Ag@SiO<sub>2</sub>@Y<sub>2</sub>O<sub>3</sub>:Er nanostructure UC materials, and the average PL intensity reached a maximum value of 4-fold larger than that of the pure Y<sub>2</sub>O<sub>3</sub>:Er at an optimal silica spacer thickness of 30 nm. Ge et al. [92] observed that with the increase of silica dielectric thickness, the green UC emission intensity of Au@SiO<sub>2</sub>@Y<sub>2</sub>O<sub>3</sub>:Yb,Er core-shell NPs increased and reached a maximum of 9.59-fold enhancement when silica thickness is ~40 nm (Figure 4). Yuan et al. [93] synthesized NaYF<sub>4</sub>:Yb,Er@SiO<sub>2</sub> core-shell structures with Ag NPs of two different sizes (15 and 30 nm) attaching to the surface of silica shell. Optimum UC luminescence enhancement was observed over a separation distance of 10 nm, and the maximum enhancement factors of 14.4-fold and 10.8-fold were observed when 15 and 30 nm Ag NPs were respectively used. It was also noted that dependence of the luminescence intensity on the separation distance between the metal NPs and chromophores was stronger for 15 nm Ag NPs compared to 30 nm. As the separation distance increased, both radiative decay and energy transfer processes would slow down, whereas the radiative decay rate changed less rapidly with the separation distance for larger metal NPs compared to smaller NPs.

Li et al. [94] reported that the UC emission intensity of NaYF<sub>4</sub>:Yb,Er,Gd nanorods increased when the nanorods were coupled with gold NPs, but the UC emission intensity suppressed when the nanorods were surrounded by continuous Au shells. Since there was no spacer between the luminescent material and metal, quenching mechanism might compete with the enhancement mechanism close to the surface of nanorods. In the case of an Au shell completely surrounding the UC nanorod, the Au was allocated so compact that additional quenching prevailed. Moreover, the condensed gold shell might block the emission transmittance from the UC nanorods.

### 4. Core-Shell Structure to Further Optimize Luminescence Properties of Nanoparticles

Weakening surface effect is to inhibit the negative factors in luminescence of NPs, while metal enhancement effect can

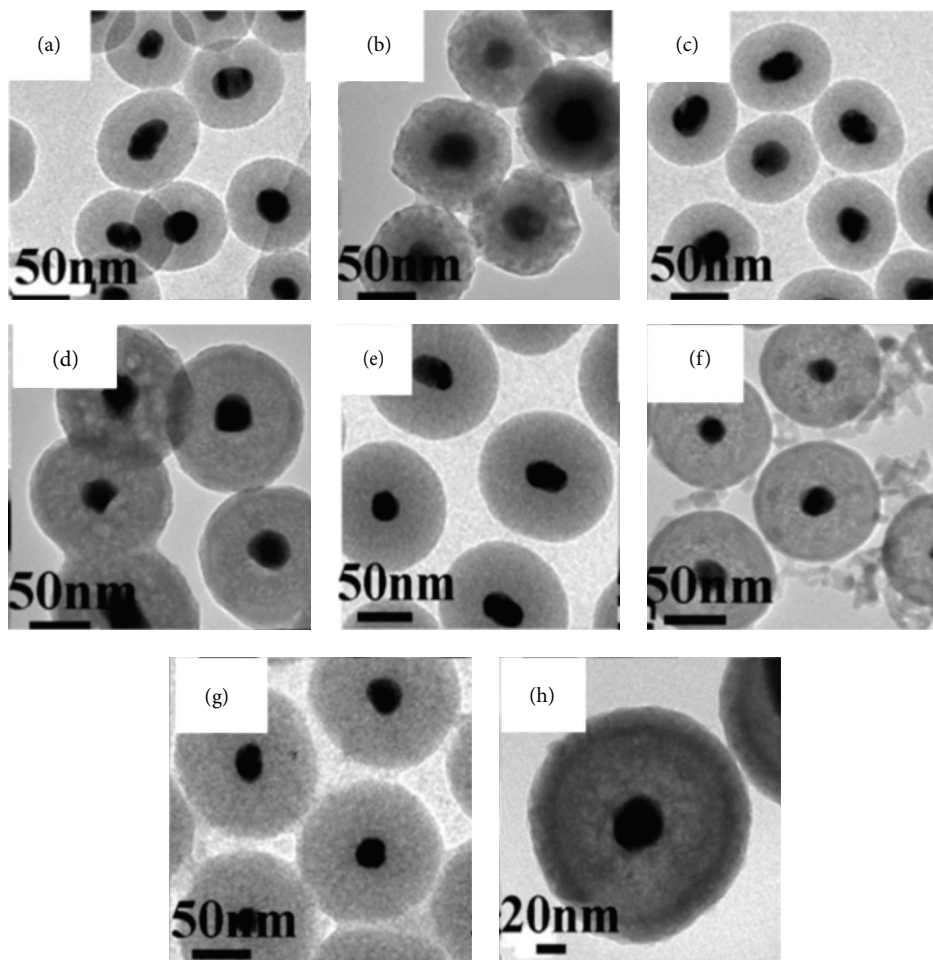


FIGURE 4: TEM images of (a)  $\sim 30$  nm Au/ $\sim 25$  nm SiO<sub>2</sub>, (b)  $\sim 30$  nm Au/ $\sim 25$  nm SiO<sub>2</sub>/ $\sim 12$  nm Y<sub>2</sub>O<sub>3</sub>:Yb<sup>3+</sup>,Er<sup>3+</sup>, (c)  $\sim 30$  nm Au/ $\sim 30$  nm SiO<sub>2</sub>, (d)  $\sim 30$  nm Au/ $\sim 30$  nm SiO<sub>2</sub>/ $\sim 12$  nm Y<sub>2</sub>O<sub>3</sub>:Yb<sup>3+</sup>,Er<sup>3+</sup>, (e)  $\sim 30$  nm Au/ $\sim 40$  nm SiO<sub>2</sub>, (f)  $\sim 30$  nm Au/ $\sim 40$  nm SiO<sub>2</sub>/ $\sim 12$  nm Y<sub>2</sub>O<sub>3</sub>:Yb<sup>3+</sup>,Er<sup>3+</sup>, (g)  $\sim 30$  nm Au/ $\sim 45$  nm SiO<sub>2</sub>, and (h) 30 nm Au/ $\sim 45$  nm SiO<sub>2</sub>/ $\sim 12$  nm Y<sub>2</sub>O<sub>3</sub>:Yb<sup>3+</sup>,Er<sup>3+</sup> [92]. Copyright Ivyspring International Publisher.

promote the positive ones. It is possible to further optimize luminescence properties of core-shell NPs by combining the two paths together and the following points should be noted in design, and preparation of core-shell NPs.

- (a) The noble metal is preferably located within the core. If the metal is located outside, its density should not be too high in order to avoid blocking of transmittance.
- (b) The distance between metal and luminescent species should be controlled within a certain range.
- (c) Lattice mismatch between core and shell should be minimized to prevent interface defects and luminescence quenching.
- (d) Annealing is commonly needed to improve crystalline of NPs and to reduce defects.
- (e) Thermal diffusion of atoms/ions in the shell of NPs should be concerned.

## 5. Conclusions and Outlook

This review seeks to summarize recent developments in optimizing luminescence properties of doped inorganic NPs with core-shell structures. Core-shell nanostructures can effectively prevent the influence of surface effect and reduce the nonradiative transition rate in NPs accordingly. On the other hand, MEL based core-shell structures can increase the radiative transition rate and excitation efficiency. Therefore, it is very promising to further optimize luminescence properties by combining the above two strategies into one core-shell nanostructure, despite the fact that the engineering and synthesis of such a complex nanostructure remain challenging. In addition, some other factors should be carefully considered when synthesizing doped core-shell NPs, such as nanoscale diffusion of atom/ion.

## Acknowledgments

This work was financially supported by NSFC (Grants nos. 61078069 and 10979009), NCET (12-0771), and

the Fundamental Research Funds for the Central Universities (2010JBZ006).

## References

- [1] H. Kim, M. Achermann, L. P. Balet, J. A. Hollingsworth, and V. I. Klimov, "Synthesis and characterization of Co/CdSe core/shell nanocomposites: bifunctional magnetic-optical nanocrystals," *Journal of the American Chemical Society*, vol. 127, no. 2, pp. 544–546, 2005.
- [2] L. Zhang, B. Liu, and S. Dong, "Bifunctional nanostructure of magnetic core luminescent shell and its application as solid-state electrochemiluminescence sensor material," *The Journal of Physical Chemistry B*, vol. 111, no. 35, pp. 10448–10452, 2007.
- [3] Y. Zhang, S. Pan, X. Teng, Y. Luo, and G. Li, "Bifunctional magnetic—luminescent nanocomposites:  $Y_2O_3/Tb$  nanorods on the surface of iron oxide/silica core—shell nanostructures," *The Journal of Physical Chemistry C*, vol. 112, no. 26, pp. 9623–9626, 2008.
- [4] Y. Li, R. Yi, and X. Liu, "Synthesis and properties of Ni/ZnS magnetic luminescent bifunctional nanocomposites," *Journal of Alloys and Compounds*, vol. 486, no. 1–2, pp. L1–L4, 2009.
- [5] J.-C. Zhou, L.-D. Sun, J. Shen, J.-Q. Gu, and C.-H. Yan, "Fluorescent-magnetic nanocrystals: synthesis and property of  $Y_{1-x}V_xO_4:Eu@GdPO_4$  core/shell structure," *Nanoscale*, vol. 3, no. 5, pp. 1977–1983, 2011.
- [6] H. Peng, G. Liu, X. Dong, J. Wang, W. Yu, and J. Xu, "Magnetic, luminescent and core-shell structured  $Fe_3O_4@YF_3:Ce^{3+},Tb^{3+}$  bifunctional nanocomposites," *Powder Technology*, vol. 215, pp. 242–246, 2012.
- [7] C. Zhong, P. Yang, X. Li et al., "Monodisperse bifunctional  $Fe_3O_4@NaGdF_4:Yb/Er@NaGdF_4:Yb/Er$  core-shell nanoparticles," *RSC Advances*, vol. 2, no. 8, pp. 3194–3197, 2012.
- [8] L. Wang, J. Luo, Q. Fan et al., "Monodispersed core-shell  $Fe_3O_4@Au$  nanoparticles," *The Journal of Physical Chemistry B*, vol. 109, no. 46, pp. 21593–21601, 2005.
- [9] C.-H. Jun, Y. J. Park, Y.-R. Yeon et al., "Demonstration of a magnetic and catalytic Co@Pt nanoparticle as a dual-function nanopatform," *Chemical Communications*, no. 15, pp. 1619–1621, 2006.
- [10] W. Chiu, P. Khiew, M. Cloke et al., "Heterogeneous seeded growth: synthesis and characterization of bifunctional  $Fe_3O_4/ZnO$  core/shell nanocrystals," *The Journal of Physical Chemistry C*, vol. 114, no. 18, pp. 8212–8218, 2010.
- [11] G. Chen, S. Desinan, R. Nechache, R. Rosei, F. Rosei, and D. Ma, "Bifunctional catalytic/magnetic Ni@Ru core-shell nanoparticles," *Chemical Communications*, vol. 47, no. 22, pp. 6308–6310, 2011.
- [12] A. J. Wang, Y. F. Li, Z. H. Li, J. J. Feng, Y. L. Sun, and J. R. Chen, "Amperometric glucose sensor based on enhanced catalytic reduction of oxygen using glucose oxidase adsorbed onto core-shell  $Fe_3O_4@silica@Au$  magnetic nanoparticles," *Materials Science and Engineering C*, vol. 32, pp. 1640–1647, 2012.
- [13] S. C. Pang, S. Y. Kho, and S. F. Chin, "Fabrication of magnetite/silica/titania core-shell nanoparticles," *Journal of Nanomaterials*, vol. 2012, Article ID 427310, 6 pages, 2012.
- [14] Z. Wang, L. Shen, and S. Zhu, "Synthesis of core-shell synthesis of core-shell  $Fe_3O_4@SiO_2@TiO_2$  microspheres and their application as recyclable photocatalysts," *International Journal of Photoenergy*, vol. 2012, Article ID 202519, 6 pages, 2012.
- [15] M. Zhu, C. Wang, D. Meng, and G. Diao, "In situ synthesis of silver nanostructures on magnetic  $Fe_3O_4@C$  core-shell nanocomposites and their application in catalytic reduction reactions," *Journal of Materials Chemistry A*, vol. 1, no. 6, pp. 2118–2125, 2013.
- [16] G. Bai, L. Shi, Z. Zhao, Y. Wang, M. Qiu, and H. Dong, "Preparation of a novel  $Fe_3O_4@SiO_2@Ni-La-B$  magnetic core-shell nanocomposite for catalytic hydrogenation," *Materials Letters*, vol. 96, pp. 93–96, 2013.
- [17] H. Peng, H. Song, B. Chen, S. Lu, and S. Huang, "Spectral difference between nanocrystalline and bulk  $Y_2O_3:Eu^{3+}$ ," *Chemical Physics Letters*, vol. 370, no. 3–4, pp. 485–489, 2003.
- [18] H. Peng, H. Song, B. Chen et al., "Temperature dependence of luminescent spectra and dynamics in nanocrystalline  $Y_2O_3:Eu^{3+}$ ," *Journal of Chemical Physics*, vol. 118, no. 7, pp. 3277–3282, 2003.
- [19] H. Peng, S. Huang, F. You, J. Chang, S. Lu, and L. Cao, "Preparation and surface effect analysis of trivalent europium-doped nanocrystalline  $La_2O_3$ ," *The Journal of Physical Chemistry B*, vol. 109, no. 12, pp. 5774–5778, 2005.
- [20] H. Peng, S. Huang, L. Sun, and C. Yan, "Analysis of surface effect on luminescent properties of  $Eu^{3+}$  in  $YVO_4$  nanocrystals," *Physics Letters A*, vol. 367, no. 3, pp. 211–214, 2007.
- [21] S. Berger, L. Schächter, and S. Tamir, "Photoluminescence as a surface-effect in nanostructures," *Nanostructured Materials*, vol. 8, no. 2, pp. 231–242, 1997.
- [22] C.-H. Yan, L.-D. Sun, C.-S. Liao et al., " $Eu^{3+}$  ion as fluorescent probe for detecting the surface effect in nanocrystals," *Applied Physics Letters*, vol. 82, no. 20, pp. 3511–3513, 2003.
- [23] V. Sudarsan, F. C. J. M. van Veggel, R. A. Herring, and M. Raudsepp, "Surface  $Eu^{3+}$  ions are different than "bulk"  $Eu^{3+}$  ions in crystalline doped  $LaF_3$  nanoparticles," *Journal of Materials Chemistry*, vol. 15, no. 13, pp. 1332–1342, 2005.
- [24] M. J. Milla, J. M. Ulloa, and A. Guzmán, "High optical sensitivity to ambient conditions of uncapped InGaAs surface quantum dots," *Applied Physics Letters*, vol. 100, no. 13, Article ID 131601, 2012.
- [25] J. Kümmerlen, A. Leitner, H. Brunner, F. Aussenegg, and A. Wokaun, "Enhanced dye fluorescence over silver island films: analysis of the distance dependence," *Molecular Physics*, vol. 80, no. 5, pp. 1031–1046, 1993.
- [26] C. D. Geddes and J. R. Lakowicz, "Metal-enhanced fluorescence," *Journal of Fluorescence*, vol. 12, no. 2, pp. 121–129, 2002.
- [27] D. K. Williams, H. Yuan, and B. M. Tissue, "Size dependence of the luminescence spectra and dynamics of  $Eu^{3+}:Y_2O_3$  nanocrystals," *Journal of Luminescence*, vol. 83–84, pp. 297–300, 1999.
- [28] B. Mercier, C. Dujardin, G. Ledoux, C. Louis, O. Tillement, and P. Perriat, "Confinement effects in sesquioxides," *Journal of Luminescence*, vol. 119–120, pp. 224–227, 2006.
- [29] J. C. Boyer, F. Vetrone, J. A. Capobianco, A. Speghini, and M. Bettinelli, "Variation of fluorescence lifetimes and judd-ofelt parameters between  $Eu^{3+}$  doped bulk and nanocrystalline cubic  $Lu_2O_3$ ," *The Journal of Physical Chemistry B*, vol. 108, no. 52, pp. 20137–20143, 2004.
- [30] J. A. Nelson, E. L. Brant, and M. J. Wagner, "Nanocrystalline  $Y_2O_3:Eu$  phosphors prepared by alkalide reduction," *Chemistry of Materials*, vol. 15, no. 3, pp. 688–693, 2003.
- [31] F. Wang, J. Wang, and X. Liu, "Direct evidence of a surface quenching effect on size-dependent luminescence of upconversion nanoparticles," *Angewandte Chemie—International Edition*, vol. 49, no. 41, pp. 7456–7460, 2010.

- [32] S. Huang and F. You, "Influence of surface quenching on luminescence dynamics of ion centers in nanocrystals," *Journal of Luminescence*, vol. 129, no. 12, pp. 1692–1694, 2009.
- [33] L. J. Tian, Y. J. Sun, Y. Yu, X. G. Kong, and H. Zhang, "Surface effect of nano-phosphors studied by time-resolved spectroscopy of  $Ce^{3+}$ ," *Chemical Physics Letters*, vol. 452, no. 1–3, pp. 188–192, 2008.
- [34] H.-L. Chou, C.-H. Tseng, K. C. Pillai, B.-J. Hwang, and L.-Y. Chen, "Surface related emission in CdS quantum dots. DFT simulation studies," *The Journal of Physical Chemistry C*, vol. 115, no. 43, pp. 20856–20863, 2011.
- [35] A. S. Ethiraj, N. Hebalkar, S. K. Kulkarni et al., "Enhancement of photoluminescence in manganese-doped ZnS nanoparticles due to a silica shell," *Journal of Chemical Physics*, vol. 118, no. 19, pp. 8945–8953, 2003.
- [36] B. Dong, L. Cao, G. Su, W. Liu, H. Qu, and D. Jiang, "Synthesis and characterization of the water-soluble silica-coated ZnS:Mn nanoparticles as fluorescent sensor for  $Cu^{2+}$  ions," *Journal of Colloid and Interface Science*, vol. 339, no. 1, pp. 78–82, 2009.
- [37] Y. Wang, W. Qin, J. Zhang, C. Cao, S. Lü, and X. Ren, "Photoluminescence of colloidal  $YVO_4:Eu/SiO_2$  core/shell nanocrystals," *Optics Communications*, vol. 282, no. 6, pp. 1148–1153, 2009.
- [38] P. Bo, C. Kai, G. Chao, and W. Wei, "The influence of  $SiO_2$  shell on fluorescent properties of  $LaF_3:Nd^{3+}/SiO_2$  core/shell nanoparticles," *Journal of Nanomaterials*, vol. 2010, Article ID 238792, 5 pages, 2010.
- [39] T. Liu, W. Xu, X. Bai, and H. Song, "Tunable silica shell and its modification on photoluminescent properties of  $Y_2O_3:Eu_3@SiO_2$  nanocomposites," *Journal of Applied Physics*, vol. 111, no. 6, Article ID 064312, 2012.
- [40] M. Wang, G. Abbineni, A. Clevenger, C. Mao, and S. Xu, "Upconversion nanoparticles: synthesis, surface modification and biological applications," *Nanomedicine: Nanotechnology, Biology, and Medicine*, vol. 7, no. 6, pp. 710–729, 2011.
- [41] X.-F. Yu, L.-D. Chen, M. Li et al., "Highly efficient fluorescence of  $NdF_3/SiO_2$  core/shell nanoparticles and the applications for in vivo NIR detection," *Advanced Materials*, vol. 20, no. 21, pp. 4118–4123, 2008.
- [42] J. Shan and Y. Ju, "Controlled synthesis of lanthanide-doped  $NaYF_4$  upconversion nanocrystals via ligand induced crystal phase transition and silica coating," *Applied Physics Letters*, vol. 91, no. 12, Article ID 123103, 2007.
- [43] R. Abdul Jalil and Y. Zhang, "Biocompatibility of silica coated  $NaYF_4$  upconversion fluorescent nanocrystals," *Biomaterials*, vol. 29, no. 30, pp. 4122–4128, 2008.
- [44] Q. Lü, F. Guo, L. Sun, A. Li, and L. Zhao, "Silica/titania-coated  $Y_2O_3: Tm^{3+}, Yb^{3+}$  nanoparticles with improvement in upconversion luminescence induced by different thickness shells," *Journal of Applied Physics*, vol. 103, no. 12, Article ID 123533, 2008.
- [45] H. Zhu, H. Hu, Z. Wang, and D. Zuo, "Synthesis of  $YVO_4:Eu^{3+}/YBO_3$  heteronanostructures with enhanced photoluminescence properties," *Nanoscale Research Letters*, vol. 4, no. 9, pp. 1009–1014, 2009.
- [46] Z. L. Wang, Z. W. Quan, P. Y. Jia et al., "A facile synthesis and photoluminescent properties of redispersible  $CeF_3, CeF_3:Tb^{3+}$ , and  $CeF_3:Tb^{3+}/LaF_3$  (core/shell) nanoparticles," *Chemistry of Materials*, vol. 18, no. 8, pp. 2030–2037, 2006.
- [47] C. Li, X. Liu, P. Yang, C. Zhang, H. Lian, and J. Lin, " $LaF_3, CeF_3, CeF_3:Tb^{3+}$ , and  $CeF_3:Tb^{3+}@LaF_3$  (core-shell) nanoplates: hydrothermal synthesis and luminescence properties," *The Journal of Physical Chemistry C*, vol. 112, no. 8, pp. 2904–2910, 2008.
- [48] S. Gai, P. Yang, X. Li et al., "Monodisperse  $CeF_3, CeF_3:Tb^{3+}$ , and  $CeF_3:Tb^{3+}@LaF_3$  core/shell nanocrystals: synthesis and luminescent properties," *Journal of Materials Chemistry*, vol. 21, no. 38, pp. 14610–14615, 2011.
- [49] J.-C. Boyer, J. Gagnon, L. A. Cuccia, and J. A. Capobianco, "Synthesis, characterization, and spectroscopy of  $NaGdF_4: Ce^{3+}, Tb^{3+}/NaYF_4$  core/shell nanoparticles," *Chemistry of Materials*, vol. 19, no. 14, pp. 3358–3360, 2007.
- [50] K. Kömpe, H. Borchert, J. Storz et al., "Green-emitting  $CePO_4: Tb/LaPO_4$  core-shell nanoparticles with 70% photoluminescence quantum yield," *Angewandte Chemie—International Edition*, vol. 42, no. 44, pp. 5513–5516, 2003.
- [51] K. Kömpe, O. Lehmann, and M. Haase, "Spectroscopic distinction of surface and volume ions in cerium(III)- and terbium(III)-containing core and core/shell nanoparticles," *Chemistry of Materials*, vol. 18, no. 18, pp. 4442–4446, 2006.
- [52] F. Zhang, R. Che, X. Li et al., "Direct imaging the upconversion nanocrystal core/shell structure at the subnanometer level: shell thickness dependence in upconverting optical properties," *Nano Letters*, vol. 12, no. 6, pp. 2852–2858, 2012.
- [53] X. Li, D. Shen, J. Yang et al., "Successive layer-by-layer strategy for multi-shell epitaxial growth: shell thickness and doping position dependence in upconverting optical properties," *Chemistry of Materials*, vol. 25, no. 1, pp. 106–112, 2012.
- [54] G. Chen, J. Shen, T. Y. Ohulchanskyy et al., " $(\alpha-NaYbF_4: Tm^{3+})/CaF_2$  core/shell nanoparticles with efficient near-infrared to near-infrared upconversion for high-contrast deep tissue bioimaging," *ACS Nano*, vol. 6, no. 9, pp. 8280–8287, 2012.
- [55] S. Kalele, S. W. Gosavi, J. Urban, and S. K. Kulkarni, "Nanoshell particles: synthesis, properties and applications," *Current Science*, vol. 91, no. 8, pp. 1038–1052, 2006.
- [56] S. T. Selvan, T. T. Y. Tan, D. K. Yi, and N. R. Jana, "Functional and multifunctional nanoparticles for bioimaging and biosensing," *Langmuir*, vol. 26, no. 14, pp. 11631–11641, 2010.
- [57] Z. Quan, Z. Wang, P. Yang, J. Lin, and J. Fang, "Synthesis and characterization of high-quality ZnS,  $ZnS:Mn^{2+}$ , and  $ZnS:Mn^{2+}/ZnS$  (Core/Shell) luminescent nanocrystals," *Inorganic Chemistry*, vol. 46, no. 4, pp. 1354–1360, 2007.
- [58] Q. Xiao and C. Xiao, "Synthesis and photoluminescence of water-soluble  $Mn:ZnS/ZnS$  core/shell quantum dots using nucleation-doping strategy," *Optical Materials*, vol. 31, no. 2, pp. 455–460, 2008.
- [59] L. Cao, J. Zhang, S. Ren, and S. Huang, "Luminescence enhancement of core-shell  $ZnS:Mn/ZnS$  nanoparticles," *Applied Physics Letters*, vol. 80, no. 23, pp. 4300–4302, 2002.
- [60] C. Jin, J. Yu, L. Sun et al., "Luminescence of  $Mn^{2+}$  doped ZnS nanocrystallites," *Journal of Luminescence*, vol. 66–67, no. 1–6, pp. 315–318, 1995.
- [61] J. Yu, H. Liu, Y. Wang et al., "Irradiation-induced luminescence enhancement effect of  $ZnS:Mn^{2+}$  nanoparticles in polymer films," *Optics Letters*, vol. 22, no. 12, pp. 913–915, 1997.
- [62] G. M. Dalpian and J. R. Chelikowsky, "Self-purification in semiconductor nanocrystals," *Physical Review Letters*, vol. 96, no. 22, Article ID 226802, 2006.
- [63] P. H. Borse, D. Srinivas, R. F. Shinde, S. K. Date, W. Vogel, and S. K. Kulkarni, "Effect of  $Mn^{2+}$  concentration in ZnS nanoparticles on photoluminescence and electron-spin-resonance spectra," *Physical Review B*, vol. 60, no. 12, pp. 8659–8664, 1999.

- [64] D. Jiang, L. Cao, G. Su et al., "Shell thickness dependence of luminescence intensity in core/shell ZnS:Mn/ZnS nanoparticles," *Materials Chemistry and Physics*, vol. 115, no. 2-3, pp. 795–798, 2009.
- [65] Y. Qu, M. Li, L. Zhang, and L. Zhao, "Preparation and characterization of upconversion luminescent  $\text{LaF}_3:\text{Yb}^{3+}, \text{Er}^{3+}/\text{LaF}_3$  core/shell nanocrystals," *Applied Surface Science*, vol. 258, no. 1, pp. 34–37, 2011.
- [66] L. P. Qian, D. Yuan, G. S. Yi, and G. M. Chow, "Critical shell thickness and emission enhancement of  $\text{NaYF}_4:\text{Yb}, \text{Er}/\text{NaYF}_4/\text{silica}$  core/shell/shell nanoparticles," *Journal of Materials Research*, vol. 24, no. 12, pp. 3559–3568, 2009.
- [67] G. Yi, Y. Peng, and Z. Gao, "Strong red-emitting near-infrared-to-visible upconversion fluorescent nanoparticles," *Chemistry of Materials*, vol. 23, no. 11, pp. 2729–2734, 2011.
- [68] C. Liu, L. Zhang, Q. Zheng, F. Luo, Y. Xu, and U. Weng, "Advances in the surface engineering of upconversion nanocrystals," *Science of Advanced Materials*, vol. 4, no. 1, pp. 1–22, 2012.
- [69] F. Vetrone, R. Naccache, V. Mahalingam, C. G. Morgan, and J. A. Capobianco, "The active-core/active-shell approach: a strategy to enhance the upconversion luminescence in lanthanide-doped nanoparticles," *Advanced Functional Materials*, vol. 19, no. 18, pp. 2924–2929, 2009.
- [70] D. Yang, C. Li, G. Li, M. Shang, X. Kang, and J. Lin, "Colloidal synthesis and remarkable enhancement of the upconversion luminescence of  $\text{BaGdF}_5:\text{Yb}^{3+}/\text{Er}^{3+}$  nanoparticles by active-shell modification," *Journal of Materials Chemistry*, vol. 21, no. 16, pp. 5923–5927, 2011.
- [71] G. Chen, T. Y. Ohulchanskyy, S. Liu et al., "Core/shell  $\text{NaGdF}_4:\text{Nd}^{3+}/\text{NaGdF}_4$  nanocrystals with efficient near-infrared to near-infrared downconversion photoluminescence for bioimaging applications," *ACS Nano*, vol. 6, no. 4, pp. 2969–2977, 2012.
- [72] R. S. Ningthoujam, L. R. Singh, V. Sudarsan, and S. Dorendrajit Singh, "Energy transfer process and optimum emission studies in luminescence of core-shell nanoparticles:  $\text{YVO}_4:\text{Eu}-\text{YVO}_4$  and surface state analysis," *Journal of Alloys and Compounds*, vol. 484, no. 1-2, pp. 782–789, 2009.
- [73] J. DiMaio, B. Kokuoz, T. L. James, T. Harkey, D. Monofsky, and J. Ballato, "Photoluminescent characterization of atomic diffusion in core-shell nanoparticles," *Optics Express*, vol. 16, no. 16, pp. 11769–11775, 2008.
- [74] J. Zheng, W. Ji, X. Wang et al., "Improved photoluminescence of  $\text{MnS}/\text{ZnS}$  core/shell nanocrystals by controlling diffusion of Mn ions into the ZnS shell," *The Journal of Physical Chemistry C*, vol. 114, no. 36, pp. 15331–15336, 2010.
- [75] S. J. Strickler and R. A. Berg, "Relationship between absorption intensity and fluorescence lifetime of molecules," *The Journal of Chemical Physics*, vol. 37, no. 4, pp. 814–822, 1962.
- [76] K. H. Drexhage, "Influence of a dielectric interface on fluorescence decay time," *Journal of Luminescence*, vol. 1-2, pp. 693–701, 1970.
- [77] K. H. Drexhage, "Interaction of light with monomolecular dye layers," in *Progress in Optics*, E. Wolf, Ed., North-Holland, Amsterdam, The Netherlands, 1974.
- [78] J. Gersten and A. Nitzan, "Spectroscopic properties of molecules interacting with small dielectric particles," *The Journal of Chemical Physics*, vol. 75, no. 3, pp. 1139–1152, 1981.
- [79] D. A. Weitz, S. Garoff, J. I. Gersten, and A. Nitzan, "The enhancement of Raman scattering, resonance Raman scattering, and fluorescence from molecules adsorbed on a rough silver surface," *The Journal of Chemical Physics*, vol. 78, no. 9, pp. 5324–5338, 1983.
- [80] J. R. Lakowicz, "Radiative decay engineering: biophysical and biomedical applications," *Analytical Biochemistry*, vol. 298, no. 1, pp. 1–24, 2001.
- [81] J. R. Lakowicz, Y. Shen, S. D'Auria et al., "Radiative decay engineering: 2. Effects of silver island films on fluorescence intensity, lifetimes, and resonance energy transfer," *Analytical Biochemistry*, vol. 301, no. 2, pp. 261–277, 2002.
- [82] J. R. Lakowicz, "Radiative decay engineering 3. Surface plasmon-coupled directional emission," *Analytical Biochemistry*, vol. 324, no. 2, pp. 153–169, 2004.
- [83] I. Gryczynski, J. Malicka, Z. Gryczynski, and J. R. Lakowicz, "Radiative decay engineering 4. Experimental studies of surface plasmon-coupled directional emission," *Analytical Biochemistry*, vol. 324, no. 2, pp. 170–182, 2004.
- [84] J. R. Lakowicz, "Radiative decay engineering 5: metal-enhanced fluorescence and plasmon emission," *Analytical Biochemistry*, vol. 337, no. 2, pp. 171–194, 2005.
- [85] A. Campion, A. Gallo, C. Harris, H. Robota, and P. Whitmore, "Electronic energy transfer to metal surfaces: a test of classical image dipole theory at short distances," *Chemical Physics Letters*, vol. 73, no. 3, pp. 447–450, 1980.
- [86] K. Asian, J. R. Lakowicz, H. Szmajcinski, and C. D. Geddes, "Metal-enhanced fluorescence solution-based sensing platform," *Journal of Fluorescence*, vol. 14, no. 6, pp. 677–679, 2004.
- [87] K. Aslan, M. Wu, J. R. Lakowicz, and C. D. Geddes, "Fluorescent core-shell  $\text{Ag}@\text{SiO}_2$  nanocomposites for metal-enhanced fluorescence and single nanoparticle sensing platforms," *Journal of the American Chemical Society*, vol. 129, no. 6, pp. 1524–1525, 2007.
- [88] K. Aslan, M. Wu, J. R. Lakowicz, and C. D. Geddes, "Metal enhanced fluorescence solution-based sensing platform 2: fluorescent core-shell  $\text{Ag}@\text{SiO}_2$  nanoballs," *Journal of Fluorescence*, vol. 17, no. 2, pp. 127–131, 2007.
- [89] Q. Zeng, Y. Zhang, X. Liu et al., "Au/ $\text{SiO}_2$  core/shell nanoparticles enhancing fluorescence resonance energy transfer efficiency in solution," *Chemical Communications*, vol. 46, no. 35, pp. 6479–6481, 2010.
- [90] C. Li, Y. Zhu, X. Zhang, X. Yang, and C. Li, "Metal-enhanced fluorescence of carbon dots adsorbed  $\text{Ag}@\text{SiO}_2$  core-shell nanoparticles," *RSC Advances*, vol. 2, no. 5, pp. 1765–1768, 2012.
- [91] F. Zhang, G. B. Braun, Y. Shi et al., "Fabrication of  $\text{Ag}@\text{SiO}_2@ \text{Y}_2\text{O}_3:\text{Er}$  nanostructures for bioimaging: tuning of the upconversion fluorescence with silver nanoparticles," *Journal of the American Chemical Society*, vol. 132, no. 9, pp. 2850–2851, 2010.
- [92] W. Ge, X. Zhang, M. Liu, Z. Lei, R. Knize, and Y. Lu, "Distance dependence of gold-enhanced upconversion luminescence in  $\text{Au}/\text{SiO}_2/\text{Y}_2\text{O}_3:\text{Yb}^{3+}, \text{Er}^{3+}$  nanoparticles," *Theranostics*, vol. 3, pp. 282–288, 2013.
- [93] P. Yuan, Y. H. Lee, M. K. Gnanasammandham, Z. P. Guan, Y. Zhang, and Q. H. Xu, "Plasmon enhanced upconversion luminescence of  $\text{NaYF}_4:\text{Yb}, \text{Er}/\text{SiO}_2@ \text{Ag}$  core-shell nanocomposites for cell imaging," *Nanoscale*, vol. 4, pp. 5132–5137, 2012.
- [94] Z. Q. Li, S. Chen, J. J. Li et al., "Plasmon-enhanced upconversion fluorescence in  $\text{NaYF}_4:\text{Yb}/\text{Er}/\text{Gd}$  nanorods coated with Au nanoparticles or nanoshells," *Journal of Applied Physics*, vol. 111, no. 1, Article ID 014310, 7 pages, 2012.

## Research Article

# Luminescent Properties of $Y_2O_3:Eu^{3+}$ Nanocrystals Prepared by Molten Salt Synthesis

Lijun Luo, Fenfen Hu, Li Xiong, Xiaofan Li, Meili Zhou, and Zhengliang Wang

*The Engineering Laboratory of Polylactic Acid-Based Functional Materials of Yunnan Province, School of Chemistry and Biotechnology, Yunnan University of Nationalities, Kunming, Yunnan 650500, China*

Correspondence should be addressed to Zhengliang Wang; wangzhengliang@foxmail.com

Received 27 March 2013; Accepted 8 July 2013

Academic Editor: Suprakas Sinha Ray

Copyright © 2013 Lijun Luo et al. This is an open access article distributed under the Creative Commons Attribution License, which permits unrestricted use, distribution, and reproduction in any medium, provided the original work is properly cited.

A series of red phosphors  $Y_2O_3:Eu^{3+}$  were prepared by the molten salt method with different surfactants. Their structures, morphologies, and the photoluminescent properties were investigated at room temperature. The particles size of  $Y_2O_3:Eu^{3+}$  can be controlled by adjusting the kinds of surfactants. The phosphor  $Y_2O_3:Eu^{3+}$  prepared with NP-10 [polyoxyethylene (10) nonyl phenyl ether] shows regular morphology and higher crystallinity, and its average particle size is about 200 nm. Bright red light can be observed by naked eyes from the red phosphor under 254 nm excitation.

## 1. Introduction

In recent years, luminescent nanocrystals (NCs) doped with rare earth ions were paid more attentions because of their interesting luminescent properties. They can be as components in displays [1], light emitting diodes [2], biological assays [3], and optoelectronic devices [4]. Cubic  $Y_2O_3:Eu^{3+}$  is one of the most important commercial red phosphors, which can be used in fluorescent lights, cathode ray tubes (CRTS), plasma display panel (PDP), and field emission display (FED) [5–9]. Many methods for synthesis of  $Y_2O_3:Eu^{3+}$  phosphor have been reported, including solution combustion method [10], sol-gel method [11], spray pyrolysis method [12], hydrothermal method [13], and precipitation method [14, 15].

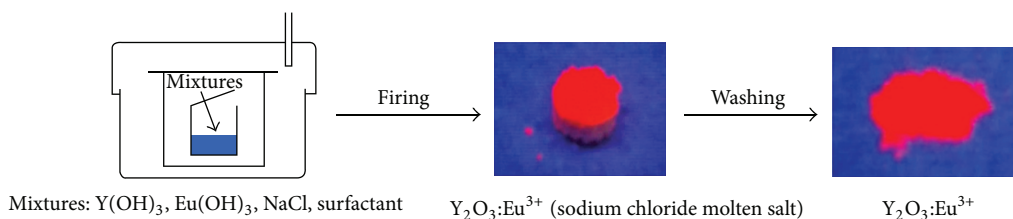
Wet chemical methods have been widely developed to prepare the luminescent materials [16–18], since these processes have advantages of good homogeneity through mixing the starting materials at the molecular level in solution, a lower calcination temperature and a shorter heating time. However, sol-gel process often requires expensive (and environmentally unfriendly) organic precursors and solvents. Then a low-temperature technique, molten salt synthesis (MSS), is beginning to attract a great deal of interest. MSS is one of the simplest and most versatile approaches available to obtain single-phase powders at lower temperatures with

shorter reaction times and little residual impurities as compared with conventional solid-state reactions [19]. The ionic fluxes molten salts possess high reactivity toward different inorganic species and relatively low melting points, which is convenient for preparation of inorganic materials. An the reaction medium, the inorganic molten salts exhibit favorable physicochemical properties such as a greater oxidizing potential, and high mass transfer, high thermal conductivity, as well as relatively lower viscosities and densities, as compared to conventional solvents [20]. Furthermore, MSS is one of the most effective ways to prepare nanoscale shape-controlled materials [21–23].

In the present study, a series of red emission phosphors  $Y_2O_3:Eu^{3+}$  were prepared by MSS with NaCl as the molten salt. Different surfactants such as polyoxyethylene (10) nonyl phenyl ether (NP-10), polyoxyethylene (5) nonyl phenyl ether (NP-5), octyl phenol together ethylene (10) ether oxygen (OP-10), and sodium dodecyl benzene sulfonate (LAS) were used to control the particles size of  $Y_2O_3:Eu^{3+}$ .

## 2. Experimental

**2.1. Preparation of  $Y_2O_3:Eu^{3+}$ .**  $Y(NO_3)_3 \cdot 6H_2O$  and  $Eu(NO_3)_3 \cdot 6H_2O$  were obtained from Aladdin Reagent limited company, China; NaOH, NaCl, and  $C_2H_5OH$  were obtained from



SCHEME 1: The setup for  $Y_2O_3:Eu^{3+}$  prepared by MMS with different surfactants.

Guangzhou Chemical Reagent Factory; poly oxyethylene (10) nonyl phenyl ether (NP-10), polyoxyethylene (5) nonyl phenyl ether (NP-5), octyl phenol together ethylene (10) ether oxygen (OP-10), sodium dodecyl benzene sulfonate (LAS) were purchased from Guangzhou Chi Hung Trade LTD. Co. All chemical reagents are of analytical reagent grade. Distilled water was used throughout.

The process to prepare  $Y_2O_3:Eu^{3+}$  nanocrystals with NP-10 (Y-NP10) is as follows: the raw materials  $Y(NO_3)_3 \cdot 6H_2O$  (4.75 mmol),  $Eu(NO_3)_3 \cdot 6H_2O$  (0.25 mmol), and NaOH (15 mmol) were mixed for 30 min in agate mortar, and then NaCl (10 g) and NP-10 (1 g) were put in the mixture and were ground for 10 min. At last, the mixture was heated at  $850^\circ C$  for 4 h. The final product was the solidified melt, which was washed with distilled water and ethanol at room temperature, and then the product was dried overnight in air at  $110^\circ C$ . The process for  $Y_2O_3:Eu^{3+}$  prepared by MMS is shown in Scheme 1.

The methods for synthesis  $Y_2O_3:Eu^{3+}$  with NP-5 (Y-NP5) and  $Y_2O_3:Eu^{3+}$  with OP10 (Y-OP10) and  $Y_2O_3:Eu^{3+}$  with LAS (Y-LAS) are similar with that of Y-NP10 mentioned above.

**2.2. Measurements.** The structure of the final product was examined by X-ray powder diffraction (XRD) using  $Cu K\alpha$  radiation on Rigaku D/Max 2200 vpc X-ray diffractometer. The size and morphology of  $Y_2O_3:Eu^{3+}$  were observed by a scanning electron microscopy (SEM) on LEO-1530 electron microscope. The luminescent spectra of the sample were recorded on an FLS920 fluorescence spectrophotometer.

### 3. Results and Discussion

The XRD patterns of  $Y_2O_3:Eu^{3+}$  prepared by MSS with different surfactants were shown in Figure 1. Curve (a) is very consistent with JCPDS43-1036 [ $Y_2O_3$ ]. This reveals that the phosphor Y-NP5 shares the cubic structure with the single phase, and  $Eu^{3+}$  ions have been effectively built into the  $Y_2O_3$  host lattices and occupied the  $Y^{3+}$  sites. Other three curves are similar with curve (a), the result shows that the single phase  $Y_2O_3:Eu^{3+}$  can be prepared by MSS with different surfactants.

The SEM images of as-prepared samples Y-NP5, Y-NP10, Y-OP10, and Y-LAS are shown in Figure 2.  $Y_2O_3:Eu^{3+}$  NCs have been successfully prepared by MSS method with NP-5. The particles are about 100 nm (Figure 2(a)). The result shows that the introduction of the surfactant NP-5 can effectively prevent  $Y_2O_3$  NCs growth. However their crystallinity is lower. Y-NP10 shows good crystallinity, and its size is about

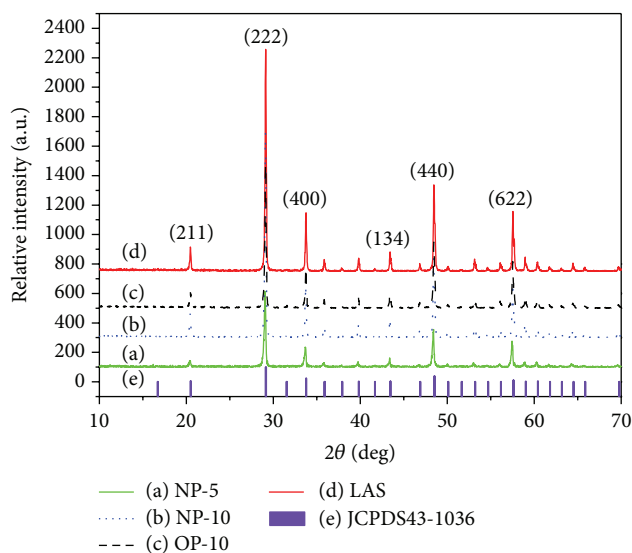


FIGURE 1: The XRD patterns of Y-NP5, Y-NP10, Y-OP10, and Y-LAS.

200 nm. We also prepared  $Y_2O_3:Eu^{3+}$  with other surfactants. Y-OP10 and Y-LAS particles sizes are about 500 nm and 1  $\mu m$ , respectively.

The excitation spectra of Y-NP5, Y-NP10, Y-OP10, and Y-LAS are shown in Figure 3. The excitation spectra of these samples exhibit similar features; the broad excitation band from 230 nm to 290 nm is attributable to the charge transfer (CT) band from the  $2p$  orbital of  $O^{2-}$  to the  $4f$  orbital of  $Eu^{3+}$ . The sharp lines in 350–550 nm range are intraconfigurational  $4f-4f$  transitions of  $Eu^{3+}$  ions in the host lattices.

Figure 4 is the emission spectra of  $Y_2O_3:Eu^{3+}$  prepared by MSS with different surfactants under 254 nm excitation. The strongest peak is at 611 nm, which is due to  $^5D_0 \rightarrow ^7F_2$  transition in  $C_2$  symmetry for  $Eu^{3+}$ . The other  $f-f$  transitions of  $Eu^{3+}$ , such as  $^5D_0 \rightarrow ^7F_1$  in 570–720 nm and  $^5D_1 \rightarrow ^7F_1$  transitions in 520–570 nm are very weak. Y-NP10 shows intense red emission. Bright red light can be observed from this phosphor under 254 nm excitation (seeing Scheme 1). Its CIE (Commission Internationale de l'Éclairage, International Commission on Illumination) chromaticity coordinates are calculated to be  $x = 0.592$ ,  $y = 0.359$ .

### 4. Conclusion

In summary,  $Y_2O_3:Eu^{3+}$  NCs were prepared by MSS with different surfactants. The structures, morphologies, and

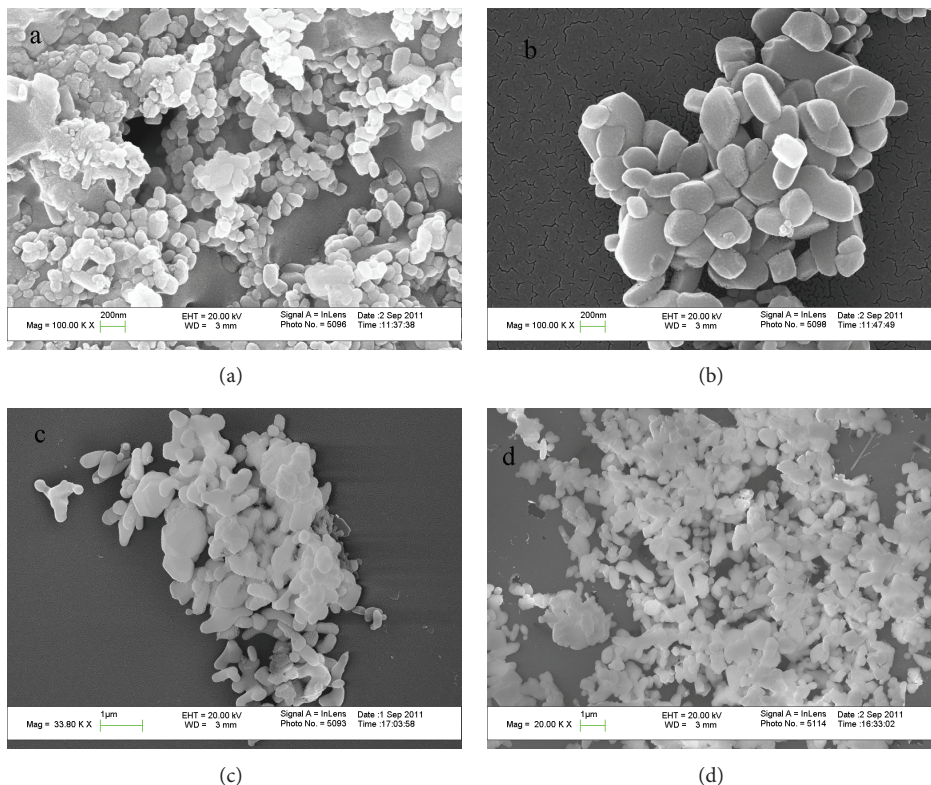


FIGURE 2: SEM images of Y-NP5, Y-NP10, Y-OP10, and Y-LAS.

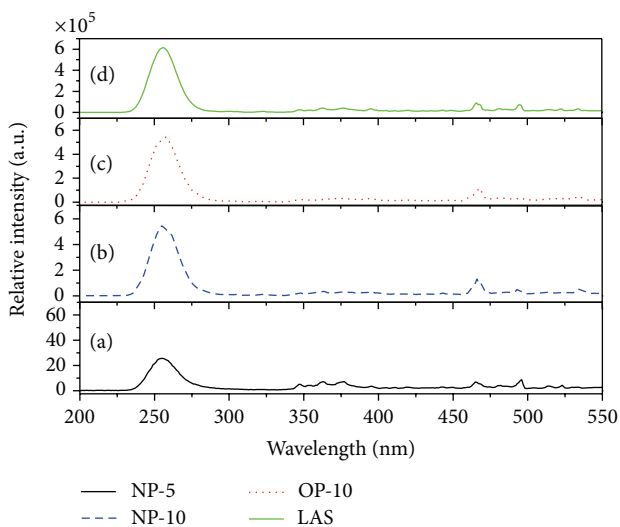


FIGURE 3: The excitation ( $\lambda_{em} = 611 \text{ nm}$ ) of Y-NP5, Y-NP10, Y-OP10, and Y-LAS.

the photoluminescent properties of the phosphors were studied. The particles size of  $\text{Y}_2\text{O}_3:\text{Eu}^{3+}$  can be controlled by adjusting the kinds of surfactants. The sample Y-NP10 shows regular morphology and intense red emission under UV excitation. Bright red light can be observed by naked eyes from this phosphor under 254 nm excitation.

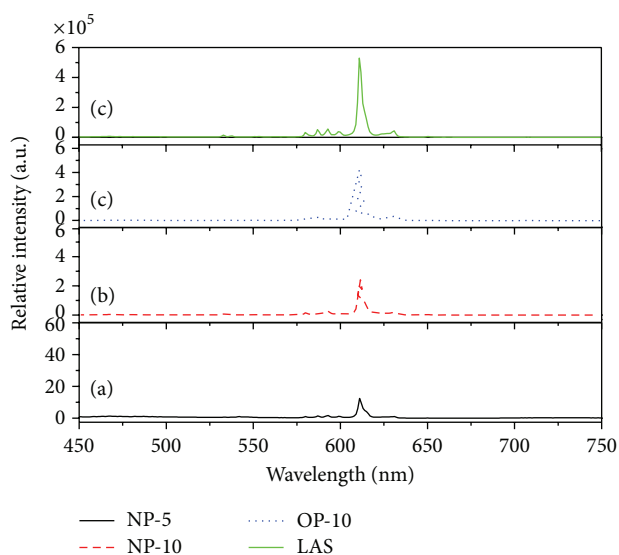


FIGURE 4: The emission spectra ( $\lambda_{ex} = 350 \text{ nm}$ ) of Y-NP5, Y-NP10, Y-OP10, and Y-LAS.

### Acknowledgments

This work was financially supported by the National Natural Science Foundation of China (21001092), the program of Innovative Research Team (in Science and Technology) at

the University of Yunnan Province (2011UY09), and Yunnan Provincial Innovation Team (2011HC008).

## References

- [1] T. Jüstel, H. Nikol, and C. Ronda, "New developments in the field of luminescent materials for lighting and displays," *Angewandte Chemie*, vol. 110, pp. 3250–3271, 1998.
- [2] A. L. Rogach, N. Gaponik, J. M. Lupton et al., "Light-emitting diodes with semiconductor nanocrystals," *Angewandte Chemie*, vol. 47, no. 35, pp. 6538–6549, 2008.
- [3] M. Dahan, T. Laurence, F. Pinaud et al., "Time-gated biological imaging by use of colloidal quantum dots," *Optics Letters*, vol. 26, no. 11, pp. 825–827, 2001.
- [4] K. E. Gonsalves, G. Carlson, S. P. Rangarajan, M. Benaissa, and M. José-Yacamán, "Synthesis and characterization of a nanostructured gallium nitride-PMMA composite," *Journal of Materials Chemistry*, vol. 6, no. 8, pp. 1451–1453, 1996.
- [5] R. G. Pappalardo and R. B. Hunt, "Dye-laser spectroscopy of commercial  $Y_2O_3:Eu^{3+}$  phosphors," *Journal of the Electrochemical Society*, vol. 132, pp. 721–730, 1985.
- [6] C. R. Ronda, "Phosphors for lamps and displays: an applicational view," *Journal of Alloys and Compounds*, vol. 225, no. 1-2, pp. 534–538, 1995.
- [7] T. Justel, H. Nikol, and C. Ronda, "New development in the field of luminescent materials for lighting and displays," *Angewandte Chemie*, vol. 37, pp. 3084–3103, 1998.
- [8] X. Jing, T. Ireland, C. Gibbons et al., "Control of  $Y_2O_3:Eu$  spherical particle phosphor size, assembly properties, and performance for FED and HDTV," *Journal of the Electrochemical Society*, vol. 146, no. 12, pp. 4654–4658, 1999.
- [9] C.-H. Kim, I.-E. Kwon, C.-H. Park et al., "Phosphors for plasma display panels," *Journal of Alloys and Compounds*, vol. 311, no. 1, pp. 33–39, 2000.
- [10] W. W. Zhang, M. Xu, W. P. Zhang et al., "Site-selective spectra and time-resolved spectra of nanocrystalline  $Y_2O_3:Eu^{3+}$ ," *Chemical Physics Letters*, vol. 376, no. 3-4, pp. 318–323, 2003.
- [11] G. S. Wu, Y. Lin, X. Y. Yuan, T. Xie, B. C. Cheng, and L. D. Zhang, "A novel synthesis route to  $Y_2O_3:Eu$  nanotubes," *Nanotechnology*, vol. 15, no. 5, pp. 568–571, 2004.
- [12] K. Y. Jung and K. H. Han, "Densification and photoluminescence improvement of  $Y_2O_3$  phosphor particles prepared by spray pyrolysis," *Electrochemical and Solid-State Letters*, vol. 8, no. 2, pp. H17–H20, 2005.
- [13] X. Wang and Y. Li, "Synthesis and characterization of lanthanide hydroxide single-crystal nanowires," *Angewandte Chemie*, vol. 41, no. 24, pp. 4790–4793, 2002.
- [14] G. Wakefield, E. Holland, P. J. Dobson, and J. L. Hutchison, "Luminescence properties of nanocrystalline  $Y_2O_3:Eu$ ," *Advanced Materials*, vol. 13, pp. 1557–1560, 2001.
- [15] A. P. Jadhav, C. W. Kim, H. G. Cha et al., "Effect of different surfactants on the size control and optical properties of  $Y_2O_3:Eu^{3+}$  nanoparticles prepared by coprecipitation method," *Journal of Physical Chemistry C*, vol. 113, no. 31, pp. 13600–13604, 2009.
- [16] G. S. Wu, Y. Lin, X. Y. Yuan, T. Xie, B. C. Cheng, and L. D. Zhang, "A novel synthesis route to  $Y_2O_3:Eu$  nanotubes," *Nanotechnology*, vol. 15, no. 5, pp. 568–571, 2004.
- [17] A. Kumar and J. Kumar, "Perspective on europium activated fine-grained metal molybdate phosphors for solid state illumination," *Journal of Materials Chemistry*, vol. 21, no. 11, pp. 3788–3795, 2011.
- [18] J. Yang and J. Lin, "Sol-gel synthesis of nanocrystalline  $Yb^{3+}/Ho^{3+}$ -doped  $Lu_2O_3$  as an efficient green phosphor," *Journal of the Electrochemical Society*, vol. 157, pp. K273–K278, 2010.
- [19] B. Yan and F. Lei, "Molten salt synthesis, characterization and luminescence of  $ZnWO_4:Eu^{3+}$  nanophosphors," *Journal of Alloys and Compounds*, vol. 507, no. 2, pp. 460–464, 2010.
- [20] S. V. Volkov, "Chemical reactions in molten salts and their classification," *Chemical Society Reviews*, vol. 19, no. 1, pp. 21–28, 1990.
- [21] J.-H. Park, D.-H. Lee, H.-S. Shin, and B.-K. Lee, "Transition of the particle-growth mechanism with temperature variation in the molten-salt method," *Journal of the American Ceramic Society*, vol. 79, no. 4, pp. 1130–1132, 1996.
- [22] C.-Y. Xu, Q. Zhang, H. Zhang, L. Zhen, J. Tang, and L.-C. Qin, "Synthesis and characterization of single-crystalline alkali titanate nanowires," *Journal of the American Chemical Society*, vol. 127, no. 33, pp. 11584–11585, 2005.
- [23] Y. Mao, T.-J. Park, F. Zhang, H. Zhou, and S. S. Wong, "Environmentally friendly methodologies of nanostructure synthesis," *Small*, vol. 3, no. 7, pp. 1122–1139, 2007.

## Research Article

# Effect of Calcination Temperature on Structural Properties and Photocatalytic Activity of Ceria Nanoparticles Synthesized Employing Chitosan as Template

Angela B. Sifontes,<sup>1</sup> Maibelin Rosales,<sup>2</sup> Franklin J. Méndez,<sup>1</sup>  
Olycen Oviedo,<sup>2</sup> and Tamara Zoltan<sup>2</sup>

<sup>1</sup>Laboratorio de Físico-Química de Superficies, Centro de Química, Instituto Venezolano de Investigaciones Científicas I.V.I.C., Caracas 1020-A, Venezuela

<sup>2</sup>Laboratorio de Fotoquímica, Centro de Química, Instituto Venezolano de Investigaciones Científicas I.V.I.C., Caracas 1020-A, Venezuela

Correspondence should be addressed to Tamara Zoltan; tzoltan@ivic.gob.ve

Received 11 April 2013; Accepted 22 May 2013

Academic Editor: Suprakas Sinha Ray

Copyright © 2013 Angela B. Sifontes et al. This is an open access article distributed under the Creative Commons Attribution License, which permits unrestricted use, distribution, and reproduction in any medium, provided the original work is properly cited.

Ceria nanoparticles were synthesized employing chitosan as template and thermal treatment at different temperatures (350, 650, and 960°C). The effect of calcination temperature on structural properties and photocatalytic activity of ceria nanopowder was also tested. Degradation of an azo dye, Congo Red (CR) as a model aqueous pollutant, was investigated by means of photocatalysis of ceria nanoparticles under visible light irradiation. The influence of catalyst amount, initial CR concentrations, and degradation reaction kinetics were studied. The results were compared with commercial CeO<sub>2</sub> at the same degradation conditions.

## 1. Introduction

The application of heterogeneous semiconductor photocatalysts in water treatment has recently drawn considerable attention because of the successful use of solar energy, which is a natural abundant energy source [1]. Of all semiconductor photocatalysts employed in water purification, TiO<sub>2</sub>, with a bandgap energy of 3.2 eV, was found to exhibit high photocatalytic activity under UV light irradiation. Besides the most commonly used TiO<sub>2</sub> catalyst, cubic fluorite cerium dioxide (CeO<sub>2</sub>), a semiconductor with a bandgap energy similar to that of titania, [2] also shows promising photocatalytic activity for the degradation of various organic dye pollutants such as Methylene Blue (MB), Methyl Orange (MO), and Reactive Black 5 (RB5). CeO<sub>2</sub> has also been successfully employed in water splitting for H<sub>2</sub> production and phenol and chlorinated phenol photodegradation under UV illumination. Although photocatalytic activity of CeO<sub>2</sub> has thoroughly been investigated, the broad bandgap energy of this material limits its

further application in the visible light region. In this regard, many methodologies have been carried out for the modification of CeO<sub>2</sub>, in order to enhance its photocatalytic activity in the visible region: doping with metals and preparation of composite materials, among others. Nonetheless, so far there are no reports of increased photoactivity in the visible region, changing their morphology through calcination temperature.

Photocatalytic properties of the materials are primarily dependent on various factors such as particle size, phase modification, structural defects/distortion (lattice), and chemical nonstoichiometry [3]. Commonly, reducing the particle size of a catalyst results in an increase of the surface area and changing its morphology, thus providing a larger number of reactive edge sites [4, 5]. It has been reported that, in general, an increase in the temperature of calcination provides a high crystallinity [6], a decrease in the surface area [7] and, for mixed materials or doped semiconductors, an absorption shift toward the visible spectrum [8, 9]. In this

sense, it has been reported that the direct relationship that exists between great surface areas and high catalytic efficiency is not always fulfilled in photocatalytic materials [10]. The justification for such behavior is based on that the energy absorption processes and the subsequent migration of electrons in the valence band (and recombination) are not simply a result of physical adsorption phenomena in the material surface. In this way, you can see that a detailed study of the electronic and morphological characteristics of new synthetic materials provide information about their potential use as photocatalysts.

Crystalline ceria nanoparticles can be synthesized by different methods, such as sonochemical [11], thermal decomposition [12] hydrothermal synthesis [13], coprecipitation [14], flame spray pyrolysis [15], combustion synthesis, and solvothermal oxidation [16]. These methodologies often require high pressure, or salt-solvent mediated high temperature, or surface capping agent. Moreover, the introduction of surfactants or templates complicated the manufacture, consumed more energy, and was not environmental friendly [17]. In addition, the sizes obtained of ceria particles are relatively large [18]. Therefore, the search for alternatives that allow the productions of cerium nanoparticles using "green" pathways, simple and low cost, is essential.

Dyes and pigments represent one problematic group; they are emitted into wastewaters from various industrial branches, mainly from the dye manufacturing and textile finishing and also from food colouring, cosmetics, paper, and carpet industries [19]. Congo red [1-naphthalene sulfonic acid, 3, 30-(4,40-biphenylenebis (azo)) bis (4-amino-) disodium salt, CR: Figure 1] is a benzidine-based anionic diazo dye, that is, a dye with two azo groups. CR is toxic to organisms and it is a suspected carcinogen and mutagen. Synthetic dyes, such as CR, are difficult to biodegrade due to their complex aromatic structures, which provide them physicochemical, thermal, and optical stability [20, 21]. Physicochemical or chemical treatment of such wastewaters is, however, possible: color removal by ultrafiltration [22], ozonation [23], coagulation [24], adsorption process [18], and so forth. The use of Advanced Oxidation Processes (AOPs), photochemically induced employing pure semiconductors [25], mixed or sensitized [26], has been widely used in recent years for the efficient degradation of CR.

Therefore, it is important to find alternatives to the degradation of reactive azo dyes in an aqueous solution and destruction of several classes of organic dyes. Most conventional treatment processes are effective in water treatment, but they only transfer the contaminants from one medium to another or generate waste that requires further treatment and disposal [19–21]. In this sense, photocatalytic reactions on irradiated semiconductor powders have a good potential for the removal of organic and inorganic waste materials from water [27]. The aim of this work was to use a prepared CeO<sub>2</sub> nanoparticles, through a simple synthetic method, environmentally benign, and low cost using chitosan as template, Ammonium Cerium (IV) Nitrate [(NH<sub>4</sub>)<sub>2</sub>Ce(NO<sub>3</sub>)<sub>6</sub>] and ammonium hydroxide [28]. Furthermore, the effect of calcination temperature of the synthesized material on size, morphology, as well as in optical properties, and the

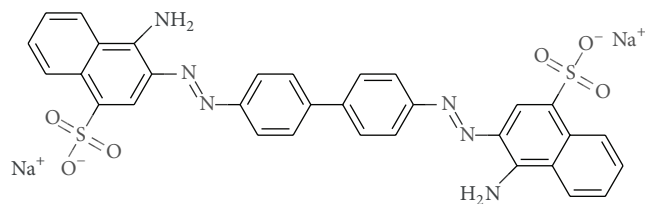


FIGURE 1: Molecular structure of Congo Red.

photocatalytic efficiency of the degradation of CR dissolved in water was evaluated.

## 2. Experimental

**2.1. Reagents and Materials.** Cerium salt compound: (NH<sub>4</sub>)<sub>2</sub>Ce(NO<sub>3</sub>)<sub>6</sub> (Sigma-Aldrich, purity ≥ 98.5%), Chitosan (Sigma-Aldrich, purity ≥ 99%), and NH<sub>4</sub>OH (Sigma-Aldrich, 28.0–30.0% NH<sub>3</sub>) were used as the starting materials. Congo Red (purity ≥ 97.0%), Acetic Acid (purity ≥ 99.7%), and BaSO<sub>4</sub> (purity > 99.99%) were purchase for Sigma-Aldrich and were used without further purification.

**2.2. Synthesis and Characterization of Photocatalysts.** Ceria nanoparticles were prepared using chitosan as template and a precursor Ce salt compound. Preparation was carried out following the procedure described by our group [28]. 1.6 g of chitosan was dissolved in 80 mL of CH<sub>3</sub>COOH (3%, v/v) and 10.41 g of (NH<sub>4</sub>)<sub>2</sub>Ce(NO<sub>3</sub>)<sub>6</sub> was dissolved in 20 mL of distilled water. The cerium aqueous solution was added to the chitosan solution, under stirring and this Ce-chitosan solution was added to a NH<sub>4</sub>OH solution (50%, v/v). The gel spheres formed were taken out from NH<sub>4</sub>OH solution and dried at room temperature for 96 h. The ceria hybrid spheres were calcined at 350, 650, and 960°C in air flow for 6 h with a heating rate of 5°C/min, to obtain light yellow CeO<sub>2</sub> nanoparticles.

The textural properties of the metal oxides were characterized by N<sub>2</sub> adsorption porosimetry (Micromeritics, ASAP 2010). The samples were first degassed at 300°C under vacuum for more than 24 h until the sample passed the degassing test. Nitrogen adsorption isotherms were measured at liquid N<sub>2</sub> temperature (77 K) and N<sub>2</sub> pressures ranging from 10<sup>-6</sup> to 1.0 P/P<sub>0</sub>. Surface areas were calculated according to Brunauer-Emmett-Teller (BET) method and the pore size distribution was obtained according to the Barret-Joyner-Halenda (BJH) method from the adsorption data [30].

The morphology and average diameter of particles were examined employing a Scanning Electron Microscopy Hitachi S-2400 instrument. The evaluation by transmission electron microscopy was performed on a Hitachi CM-10 instrument operated at 120 kV.

All the samples were characterized by diffuse reflectance spectroscopy (DRS). UV-Vis DR spectra were recorded at room temperature in the range of 200–700 nm employing a Lambda 35 UV-Vis spectrophotometer (Perkin Elmer) equipped with an integrating sphere assembly, using BaSO<sub>4</sub>

as the reflectance reference sample. The absorption spectra were obtained by analyzing the reflectance measurement with Kubelka-Munk (KM) emission function:  $F(R_{\infty})$ . Optical bandgap energy ( $E_g$ ) can be determined from the plot between  $E = 1240/\lambda_{Abs}$  and  $[F(R_{\infty})h\nu]^{1/2}$  where  $E$  is the photonic energy in eV and  $h\nu$  is the energy of an incident photon.

**2.3. Photocatalytic Activity for the Degradation of Congo Red (CR).** The photocatalytic activities of the catalysts were evaluated by degradation of CR in aqueous solution. The photocatalysis experiments were performed in a batch reactor using an illuminator Cole Palmer 41720-series, with an emission maximum in UV 350–500 nm (3.5 mW/cm<sup>2</sup>, 49,400 Lux/seg), keeping a distance of 10 cm between the lamp surface and the solution, varying the time periods of exposure at 25°C under continuous shaking. In a typical experiment, the reaction suspension consisting of CR aqueous solution (50 mg L<sup>-1</sup>, 100 mL) and catalyst (0.05 g) was stirred with a magnetic bar. In all cases, the mixture was kept in the dark for 24 h to ensure that the adsorption-desorption equilibrium was reached before irradiation. After light irradiation, the sample was withdrawn from the suspensions every 10 min during the irradiation; 0.5 mL of the analytical solution was taken from the mixture and immediately centrifuged. The concentration of the RC in the analytical solution was determined spectrophotometrically at 498 nm. A calibration plot based on Beer-Lambert's law was established by relating the absorbance to the concentration.

### 3. Results and Discussion

X-ray diffraction (XRD) and transmission electron microscopy (TEM) were used to study the microstructure of metal oxides. Both techniques revealed the crystalline character of the CeO<sub>2</sub> powder, showing broad diffraction peaks (XRD) and diffraction rings (TEM) that are the characteristic patterns of nanocrystalline materials.

The XRD patterns of the as-prepared powder and heat-treated ceria nanoparticles at different temperatures (350, 650, and 960°C) are shown in Figure 2. The calcined samples exhibit XRD peaks that correspond to the (111), (200), (220), (311), (222), and (400) planes, which revealed well-developed reflections of cerium oxide (ICDD PDF No. 81-0792), space group  $Fm\bar{3}m$  (225), showing that the synthesized samples were pure CeO<sub>2</sub> with cubic fluorite structure [16]. No peak of any other phase was detected. The intensities and positions of the diffraction peaks were in agreement with the literature data.

The lattice parameter of cerium oxide nanoparticles was measured using X-ray diffraction (XRD) (Table 1). The constant "a" of the cubic fluorite-type CeO<sub>2</sub> grains can be determined through the spacing of the  $hkl$  lattice planes ( $d_{hkl}$ ) and taking into account Bragg's law [31]. The results were checked with Celref software.

SEM and TEM analysis allowed us to investigate the morphology and structure of the synthetic materials.

Ceria materials were produced by the calcination of precipitates (hybrid spheres) at 350, 650, and 960°C. SEM

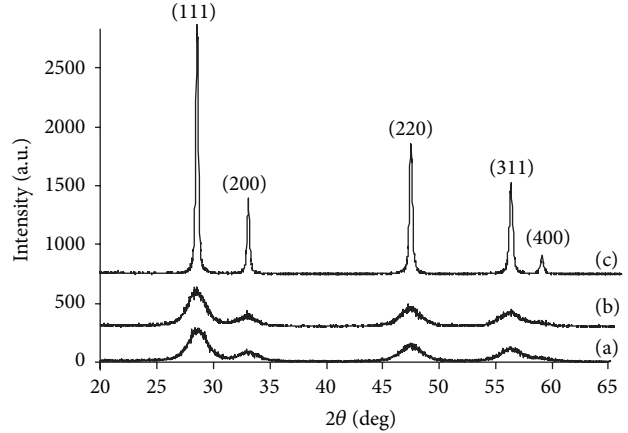


FIGURE 2: XRD patterns of synthesized CeO<sub>2</sub> nanoparticles prepared at different calcination temperatures, (a) 350°C, (b) 650°C, and (c) 960°C.

TABLE 1: Summary of crystallite size and lattice parameter for CeO<sub>2</sub> particles prepared at different calcination temperature.

Temperature (°C)	Lattice parameter (nm)	TEM crystallite size (nm)	$S_{BET}$ (m <sup>2</sup> /g)
350	0.5470	4	105.12
650	0.5424	17	13.02
960	0.5411	61	8.02

and TEM micrographs of calcinated materials are show in Figure 3; it can observed that the particles synthesized show the topography of foams with high porosity.

Figure 3 also shows TEM images with corresponding selected area electron diffraction pattern (SAED). The crystalline size has been directly estimated using such images. It can also be observed that calcined nanoparticles exhibited roughly spherical shape. Moreover, an increase in the calcination temperature led to the appreciable growth in the crystallite size.

The SAED pattern shows continuous ring patterns without any additional diffraction spots and rings of secondary phases, revealing their highly crystalline structure. As summarized in Table 2, measured interplanar spacings ( $d_{hkl}$ ) from SAED patterns are in good agreement with the values in the standard data (JCPDS: 34-0394). All the rings could be precisely indexed to the cubic CeO<sub>2</sub> phase; this observation is in agreement with XRD results. The diffraction pattern was further examined for all possible forms of cerium oxide for matches to the unknown ring.

Surface physical properties including pore characteristics, surface area, surface morphology, and textural aspects of synthesized materials have been studied and the results are summarized in Table 3.

The data summarized in Table 3 clearly shows the formation of mesopores in the cerium nanoparticles synthesized through use of chitosan template. Furthermore, it was found that the surface area decreased with increasing calcination temperature, showing phase sintering cerium oxide with

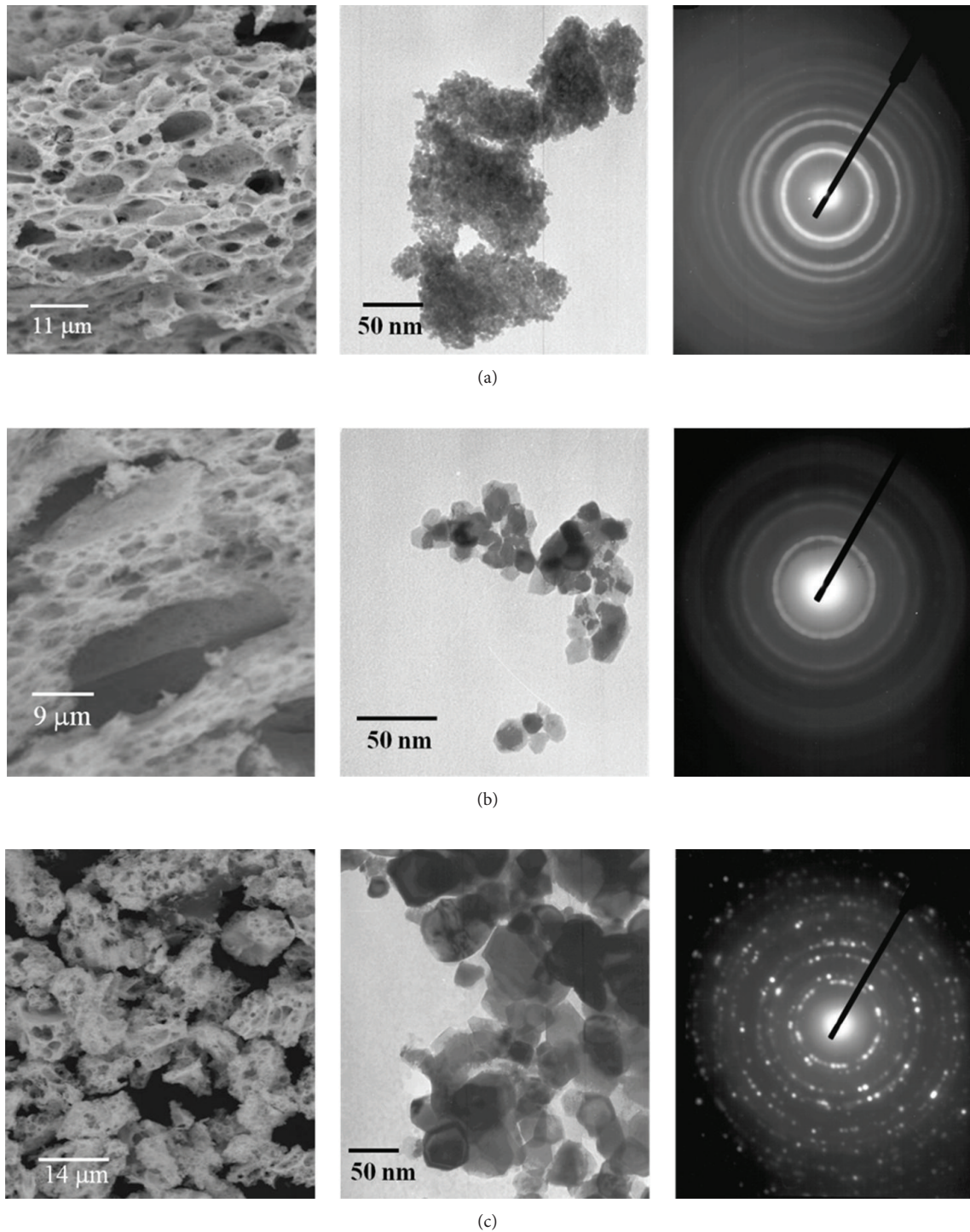


FIGURE 3: SEM, TEM, and electron diffraction pattern of  $\text{CeO}_2$  nanoparticles at different calcination temperatures, (a)  $350^\circ\text{C}$ , (b)  $650^\circ\text{C}$ , and (c)  $960^\circ\text{C}$ .

increased high temperature crystallinity. Thus, the use of the chitosan template clearly results in a substantial increase in the surface area, and hence, the present method provides a synthesis method of easy and low cost for obtaining nanoparticles of cerium with high surface area and mesoporous.

#### 4. UV-Vis Diffuse Reflectance Analysis

UV-vis diffuse reflectance spectroscopy (UV-vis DRS) was used to probe the band structure or molecular energy levels in the materials since UV-vis light excitation creates

TABLE 2: Measured interplanar spacing ( $d$ ) from selected area diffraction pattern in Figure 3, compared with reference values (standard data JCPDS: 34-0394) of different cerium oxide forms.

Calcined sample CeO <sub>2</sub> (Å)			Standard data JCPDS: 34-0394 (Å)				
350°C	650°C	960°C	CeO <sub>2</sub>	CeO	CeO <sub>2-x</sub>	Ce <sub>2</sub> O <sub>3</sub>	Ce
3.119	3.099	3.124	3.124 (111)	2.938 (111)	3.39 (222)	2.945 (0111)	2.97 (111)
2.696	2.687	2.705	2.706 (200)	2.544 (200)	2.06 (044)	2.254 (1012)	2.57 (200)
1.917	1.904	1.913	1.913 (220)	1.799 (220)	1.65 (543)	1.945 (1120)	1.82 (220)
1.632	1.623	1.631	1.632 (311)	1.534 (311)		1.733 (1013)	1.55 (311)
1.562	1.556	1.561	1.561 (222)			1.637 (1122)	

TABLE 3: Summary of the surface area, pore diameter, and pore volume for CeO<sub>2</sub> materials prepared at different calcination temperature.

Temperatures (°C)	S <sub>BET</sub> (m <sup>2</sup> /g)	Pore volume (cm <sup>3</sup> /g)	Pore diameter (nm)
350	105.12	0.065	7
650	13.02	0.023	13
960	8.02	0.020	15

photogenerated electrons and holes [32]. The DRS spectra of CeO<sub>2</sub> powders calcined at different temperatures (350, 650, and 960°C) are shown in Figure 4. DRS measurements were used to obtain information about absorption spectra and bandgap of catalysts or map the electronic structure of the metal ions by measuring d-d, f-d transitions, and oxygen-metal ion charge transfer bands. It has been reported that bulk CeO<sub>2</sub> show absorption maxima around 300 nm in its DRS [33].

According to Bensalem et al. [34], the spacing of the electronic levels and the energy bandgap ( $E_g$ ) is highly dependent on the particle size. An UV absorption edge at about 500 nm occurs for ceria caused by Ce<sup>+4</sup>←O<sup>2-</sup> charge transfer [33–35]. When CeO<sub>2</sub> is synthesized at increasing calcination temperatures, a blue shift from 500 nm to 411, 375, and 364 nm is observed (respectively, for 350, 650, and 960°C). For the samples calcined this shift of the absorbance towards shorter wavelengths can be explained as a consequence of either the quantum size effect originated by the diminution of ceria particle size, or the existence of larger contribution of Ce<sup>+4</sup>←O<sup>2-</sup> charge transfer transitions, which yields a relatively broad band with a maximum at ca. 380 nm [33–35]. However, the calculations for the quantum size effect establish that there are no significant variations in the chemical composition in the structure of metal oxide as a result of particle size reduction [36]. In our case, the influence due to the presence of different states of oxidation of CeO<sub>2</sub>, the presence of a significant fraction of Ce atoms (either in the state +3 or +4) on the outer surface which generates oxygen vacancies and defects, has a higher influence on the  $E_g$ , expected by quantum size effect. In this sense, the presence of Ce<sup>+3</sup> species has been verified using EPR and Raman analysis. Neto and Schmal [37] show that increases in the calcination temperature, as well as in the synthesis condition, leads to an increase in the concentration of Ce<sup>+3</sup> species and therefore an increase in oxygen vacancies.

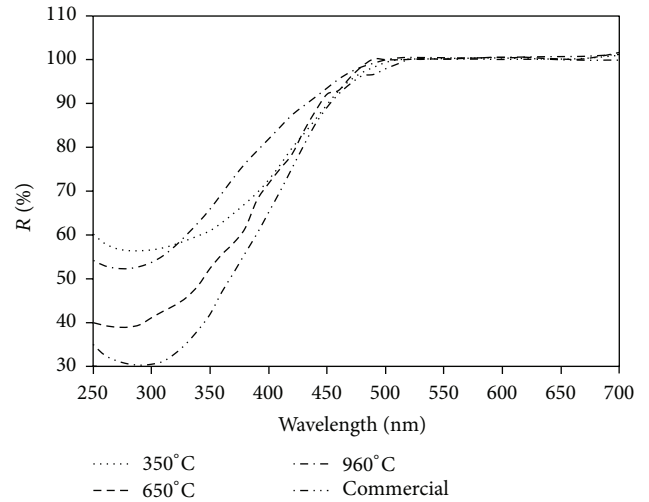


FIGURE 4: UV-vis diffuse reflectance spectra of CeO<sub>2</sub> samples after calcination at 350°C (· · ·), 650°C (- - -), and 960°C (- · -) and commercial (- · · ·).

The  $E_g$  of synthesized samples in this work was calculated by Kubelka-Munk function  $F(R)$  which is related to the diffuse reflectance,  $R$ , of the sample according to the following equation [38]:

$$F(R) = \frac{(1 - R)^2}{2R}, \quad (1)$$

where “ $R$ ” is the absolute value of reflectance. The  $E_g$  of the CeO<sub>2</sub> nanoparticles were calculated from their diffuse-reflectance spectra by plotting the square of the Kubelka-Munk function  $F(R)^2$  versus energy in electron volts (Figure 5). The linear region of the curve was extrapolated to  $F(R)^2 = 0$  to get the direct  $E_g$ . The optical bandgap for all samples were determined by the above method. The  $E_g$  and calculated absorption maxima of calcinated samples are given in Table 4.

Table 4 clearly shows an increase in  $E_g$  (decrease in the absorption edge) due to the increase in the crystal size. It is reported that CeO<sub>2</sub> nanocrystals show a bandgap energy ( $E_g$ ) between 2.7 and 3.4 eV and absorb strongly in the UV region with the absorption threshold near to 400 nm (25 000 cm<sup>-1</sup>). As shown in Table 4, the bandgap energies for samples calcined at different temperatures were 3.02, 3.31, and 3.41 eV for 350, 650, and 960°C, respectively.

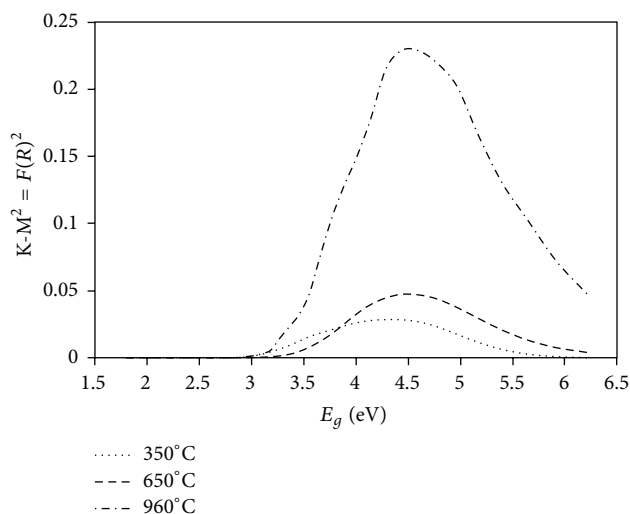


FIGURE 5: Bandgap measurements of CeO<sub>2</sub> samples after calcination at 350°C (· · ·), 650°C (---), and 960°C (- · -).

TABLE 4: The band gap energy and crystal size of CeO<sub>2</sub> samples calcined at different temperatures.

Temperature (°C)	$E_g$ (eV)	Absorption edge (nm)	Crystallite size (nm)
350	3.02	411.4	4
650	3.31	373.3	17
960	3.41	364.3	61
Commercial	3.19*	389.4	—

\* Reported [29].

It can be seen that the value obtained in this work for the  $E_g$  value for the sample calcined at 350°C is lower than that reported by us previously [28]. This behavior can be explained in terms of the measurement system in the first report that the  $E_g$  was calculated from the spectrum of UV-vis absorption, whereas in this study DRS spectrum was used. In the literature, different  $E_g$  values have been found for nanoparticles of similar sizes when using different measurement systems [29, 39]. This is attributed to the fact that diffuse reflectance spectroscopy (DRS) takes advantage of the enhanced scattering phenomenon in powder materials, making this technique more suitable to characterize nanomaterials than UV-vis absorption spectroscopy. Consequently, light scattering effects in the absorption spectra of powder samples dispersed in liquid media can be avoided using DRS. [40].

The relationship between the crystal size and the bandgap energy is shown in Figure 6.

The  $E_g$  of CeO<sub>2</sub> is usually reported to be higher with lowering of particle size, owing to the quantum confinement effect [41]. However, the ceria samples synthesized in this work using chitosan as a template showed the opposite behavior. This could be due to formation of larger size agglomerates, feasibly as a consequence of the use of chitosan as template. Previous reports make mention of the lower bandgap energy

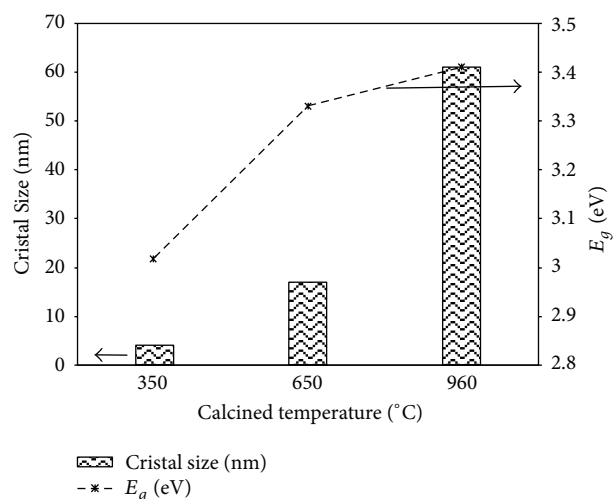


FIGURE 6: Correlation among the crystal size and the energy bandgap of CeO<sub>2</sub> samples after calcination at 350°C, 650°C, and 960°C.

$E_g$  for CeO<sub>2</sub> nanorods as compared to that of CeO<sub>2</sub> nanoparticles as well, indicating the influence of crystallite size as well as the overall particle size on bandgap energy [29]. However, the incorporation of nonmetals, carbon, and nitrogen (from chitosan) in the ceria structure could also contribute to the lowering of bandgap. Heating rates in the calcination would also contribute to the presence of these elements (C and N).

## 5. Photocatalytic Activity

The photocatalytic activity of the CeO<sub>2</sub> samples calcined at different temperatures was evaluated by the photodegradation of CR at room temperature under UV and visible light irradiation. The efficiency of the materials synthesized in the photodegradation (%D) of CR was determined using the following expression [42]:

$$\%D = \frac{C_0 - C}{C_0} \times 100, \quad (2)$$

where  $C_0$  is the initial concentration of CR and  $C$  is the remaining concentration of CR after irradiation in the desired time interval.

Figure 7 clearly shows that irradiation in the presence of CeO<sub>2</sub> nanoparticles leads to an increase in the degradation efficiency of CR. Materials prepared in this work all have an onset of absorption at wavelengths below 420 nm. Therefore, radiation of wavelength less than 420 nm is suitable for the transfer of electrons from the valance band to the conductance band. It can be seen that the rate of CR photodegradation increased gradually with time, reaching efficiency values of 41, 51, and 64% after 15 h to calcinated temperatures samples: 350, 650 and 960 respectively. After 24 hours of irradiation was obtained 62, 71, and 91% degradation for the samples calcined at 350, 650, and 960°C respectively, showing that higher calcination temperatures lead to higher efficiencies in the photodegradation of RC.

The photocatalytic efficiency (activity) of each CeO<sub>2</sub> catalyst for the degradation of Congo Red was quantified in two

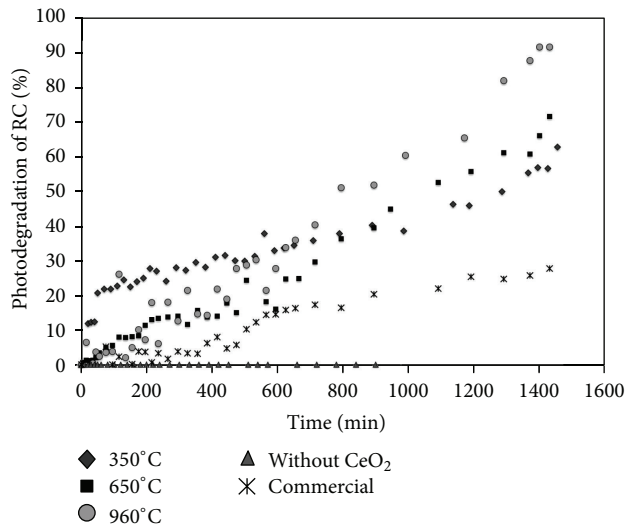


FIGURE 7: Degradation efficiency of CR (50 mg/L) catalyzed by CeO<sub>2</sub> nanoparticles (0.5 g/L) calcined at different temperatures: 350°C, 650°C, and 960°C and commercial.

ways: measurement of Congo Red half-life time under standard conditions and Langmuir-Hinshelwood kinetic analysis.

Surface catalyzed reactions can often be adequately described by a unimolecular Langmuir-Hinshelwood (L-H) mechanism, in which an adsorbed reactant with fractional surface coverage  $\theta$  is consumed at an initial rate given by

$$r = -\frac{dC}{dt} = k_r\theta = \frac{k_r K_{LH} C}{1 + K_{LH} C + K_w C_w}, \quad (3)$$

where  $r$  is the oxidation rate of the reactant ( $\text{mg L}^{-1} \text{min}^{-1}$ ),  $C$  the concentration of the reactant ( $\text{mg L}^{-1}$ ),  $t$  the illumination time,  $k_r$  the constant of reaction rate ( $\text{mg L}^{-1} \text{min}^{-1}$ ),  $K_{LH}$  the adsorption constant of the reactant ( $\text{L mg}^{-1}$ ),  $K_w$  the solvent adsorption constant, and  $C_w$  its concentration. As  $C_w \gg C$  and  $C_w$  remains practically constant, the part of the catalyst covered by water is unalterable over the whole range of concentration. In this work, all experimental conditions were the same. Therefore,  $C$  will only be variable in the initial reactions:

$$r = -\frac{dC}{dt} = \frac{k_r K_{LH} C}{1 + K_{LH} C}. \quad (4)$$

When the chemical concentration  $C_i$  is a millimolar solution ( $C_0$  small) the equation can be simplified to an apparent first-order equation:

$$\ln\left(\frac{C}{C_0}\right) = k_r K t = -k_{app} t, \quad (5)$$

where  $k_{app}$  is the apparent pseudo-first-order reaction rate constant and  $t$  is the reaction time. The variation in the  $\ln(C/C_0)$  as a function of the irradiation time  $t$  is given in Figure 8.

The straight lines obtained by plotting  $\ln(C_0/C)$  versus time of irradiation indicate that the degradation of Congo

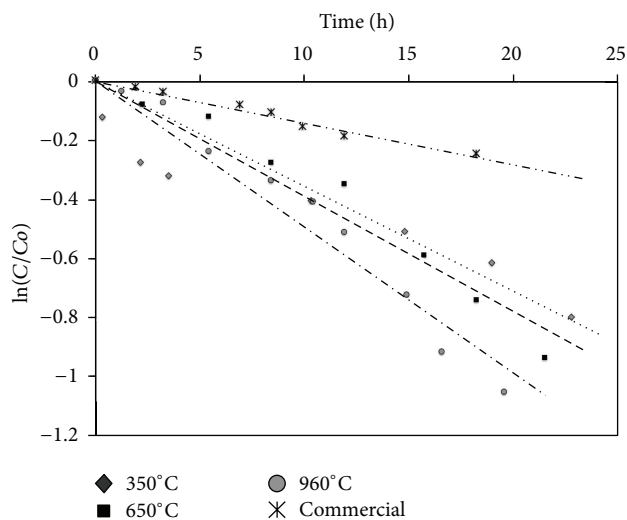


FIGURE 8: Apparent first order kinetic model for CR photodegradation by CeO<sub>2</sub> samples after calcination at 350°C (· · ·), 650°C (---), and 960°C (- - -) and commercial (- · - ·), with a reaction time of 22 h.

Red satisfactorily fits the model L-H. This behavior allows to infer about the existence of an equilibrium between the phenomena of adsorption and photodegradation reactions. The kinetic data obtained in Figure 8 regarding to the pseudo-first-order rate constant,  $k_{app}$ , and the half-life,  $t_{1/2}$ , for the photocatalytic degradation of RC are listed in Table 5.

From Table 5 it can be seen that an increase in the calcination temperature leads to an increase in the rate of photodegradation of CR by cerium nanoparticles. This increase in the activity can be explained in terms of the morphological differences among the synthesized materials, since it has been reported that the photocatalytic activity of metal oxides is strongly dependent on their morphological properties [42]. Table 3 shows that the calcined material at 960 presents a greater crystallinity and particle size in comparison with the materials calcined at 350 to 650 and taking into account that a greater crystallinity of the material gives less surface defects which can act as recombination centers of electron-hole pair, explains the fact most photocatalytic activity of the calcined material at high temperatures [43]. This may be corroborated considering the low reaction rate of the commercial cerium that has a low crystallinity.

Some semiconductor materials, such as titania, it has been reported that the specific surface area and crystallinity are two contradictory factors that influence the photocatalytic activity. In that sense, amorphous semiconductor material with high surface area is generally associated with a large amount of crystal defects or weak crystallization, which favors recombination processes of electrons and holes photogenerated, causing a poor photoactivity [44]. Therefore, a large surface area is required, but not a decisive factor. For example, amorphous TiO<sub>2</sub> powders generally exhibit a large specific surface area, but poor photocatalytic activity or negligible due to recombination of electrons and positive holes photoexcited defects (i.e., imperfections, impurities, dangling

TABLE 5: Apparent constant and half-life for the Langmuir-Hinshelwood model and specific photoactivity for Congo Red photodegradation by CeO<sub>2</sub> nanoparticles calcined at different temperatures.

Temperature (°C)	$k_{app}$ (h <sup>-1</sup> )	$t_{1/2}$ (h)	Specific photoactivity $k_{app}/S_{BET}$ ( $\bar{k}$ in g m <sup>-2</sup> h <sup>-1</sup> )
350	0.0356	19.47	$0.34 \times 10^{-3}$
650	0.0390	17.77	$2.99 \times 10^{-3}$
960	0.0495	14.00	$6.17 \times 10^{-3}$
Commercial	0.0141	49.16	—

bonds, or microvoids) located on the surface and in the bulk of the particles [9]. In this regard, examining the values obtained for specific photocatalytic activity (Table 5) can be seen that a high crystallinity provides higher photocatalytic activity, indicating that the crystallinity is another important requirement that must be taken into account in the design (and study) of new photocatalytic materials.

## 6. Conclusion

In summary, in this work cerium oxide nanoparticles using chitosan as template were synthesized and characterized. After subsequent heat treatment, an increase in degree in crystallinity and the particle size was observed as a result of temperature increase. DRS studies showed that an increase in the calcination temperature produces a blue shift in the absorption maxima of the absorption spectrum and a decrease of  $E_g$  being a consequence of the increase in particle size. Studies on the photocatalytic degradation of CR demonstrated that the calcined materials at higher temperatures, exhibited greater activity as a result of larger particle size and high crystallinity. Thus, we can conclude that variation by calcination temperatures allows obtaining materials with optical and morphological properties that enable their efficient use as photocatalysts.

## References

- N. Wetchakun, S. Chaiwichain, B. Inceesungvorn et al., "BiVO<sub>4</sub>/CeO<sub>2</sub> nanocomposites with high visible-light-induced photocatalytic activity," *ACS Applied Materials and Interfaces*, vol. 4, no. 7, pp. 3718–3723, 2012.
- G. Magesh, B. Viswanathan, R. P. Viswanath, and T. K. Varadarajan, "Photocatalytic behavior of CeO<sub>2</sub>-TiO<sub>2</sub> system for the degradation of methylene blue," *Indian Journal of Chemistry A*, vol. 48, no. 4, pp. 480–488, 2009.
- F. Zhang, S.-W. Chan, J. E. Spanier et al., "Cerium oxide nanoparticles: size-selective formation and structure analysis," *Applied Physics Letters*, vol. 80, no. 1, pp. 127–129, 2002.
- B. M. Reddy and A. Khan, "Nanosized CeO<sub>2</sub>-SiO<sub>2</sub>, CeO<sub>2</sub>-TiO<sub>2</sub>, and CeO<sub>2</sub>-ZrO<sub>2</sub> mixed oxides: influence of supporting oxide on thermal stability and oxygen storage properties of ceria," *Catalysis Surveys from Asia*, vol. 9, no. 3, pp. 155–171, 2005.
- S. Deshpande, S. Patil, S. V. Kuchibhatla, and S. Seal, "Size dependency variation in lattice parameter and valency states in nanocrystalline cerium oxide," *Applied Physics Letters*, vol. 87, no. 13, Article ID 133113, pp. 1–3, 2005.
- S. Mozia, "Application of temperature modified titanate nanotubes for removal of an azo dye from water in a hybrid photocatalysis-MD process," *Catalysis Today*, vol. 156, no. 3-4, pp. 198–207, 2010.
- A. Bumajdad, M. I. Zaki, J. Eastoe, and L. Pasupulety, "Microemulsion-based synthesis of CeO<sub>2</sub> powders with high surface area and high-temperature stabilities," *Langmuir*, vol. 20, no. 25, pp. 11223–11233, 2004.
- Y. Yang and C. Tian, "Effects of calcining temperature on photocatalytic activity of Fe-doped sulfated titania," *Photochemistry and Photobiology*, vol. 88, no. 4, pp. 816–823, 2012.
- J. Fan, L. Zhao, J. Yu, and G. Liu, "The effect of calcination temperature on the microstructure and photocatalytic activity of TiO<sub>2</sub>-based composite nanotubes prepared by an in situ template dissolution method," *Nanoscale*, vol. 4, no. 20, pp. 6597–6603, 2012.
- J. Yu, W. Wang, B. Cheng, B. Huang, and X. Zhang, "Preparation and photocatalytic activity of multi-modally macro/mesoporous titania," *Research on Chemical Intermediates*, vol. 35, no. 6-7, pp. 653–665, 2009.
- R.-J. Qi, Y.-J. Zhu, G.-F. Cheng, and Y.-H. Huang, "Sonochemical synthesis of single-crystalline CeOHCO<sub>3</sub> rods and their thermal conversion to CeO<sub>2</sub> rods," *Nanotechnology*, vol. 16, no. 11, pp. 2502–2506, 2005.
- M. A. Gabal, S. A. K. Elroby, and A. Y. Obaid, "Synthesis and characterization of nano-sized ceria powder via oxalate decomposition route," *Powder Technology*, vol. 229, pp. 112–118, 2012.
- C. Liu, L. Luo, and X. Lu, "Preparation of mesoporous Ce<sub>1-x</sub>Fe<sub>x</sub>O<sub>2</sub> mixed oxides and their catalytic properties in methane combustion," *Kinetics and Catalysis*, vol. 49, no. 5, pp. 676–681, 2008.
- M. Jalilpour and M. Fathalilou, "Effect of aging time and calcination temperature on the cerium oxide nanoparticles synthesis via reverse co-precipitation method," *International Journal of the Physical Sciences*, vol. 7, no. 6, 2012.
- C. Chaisuk, A. Wehatoranawee, S. Preampiyawat, S. Netiphat, A. Shotipruk, and O. Mekasuwandumrong, "Preparation and characterization of CeO<sub>2</sub>/TiO<sub>2</sub> nanoparticles by flame spray pyrolysis," *Ceramics International*, vol. 37, no. 5, pp. 1459–1463, 2011.
- M. Zawadzki, "Preparation and characterization of ceria nanoparticles by microwave-assisted solvothermal process," *Journal of Alloys and Compounds*, vol. 454, no. 1-2, pp. 347–351, 2008.
- M. Sun, G. Zou, S. Xu, and X. Wang, "Nonaqueous synthesis, characterization and catalytic activity of ceria nanorods," *Materials Chemistry and Physics*, vol. 134, no. 2-3, pp. 912–920, 2012.
- S. Kaur, S. Rani, and R. K. Mahajan, "Adsorption kinetics for the removal of hazardous dye congo red by biowaste materials as adsorbents," *Journal of Chemistry*, vol. 2013, Article ID 628582, 12 pages, 2013.
- I. D. Mall, V. C. Srivastava, N. K. Agarwal, and I. M. Mishra, "Removal of congo red from aqueous solution by bagasse fly ash and activated carbon: kinetic study and equilibrium isotherm analyses," *Chemosphere*, vol. 61, no. 4, pp. 492–501, 2005.
- S. P. Meshram, D. T. Tayade, P. D. Ingle, P. D. Jolhe, B. B. Diwate, and S. B. Biswas, "Ultrasonic cavitation induced degradation of Congo red in aqueous solutions," *Chemical Engineering Research Bulletin*, vol. 14, no. 2, 2010.
- H. Chen and J. Zhao, "Adsorption study for removal of Congo red anionic dye using organo-attapulgitite," *Adsorption*, vol. 15, no. 4, pp. 381–389, 2009.

- [22] H. P. Srivastava, G. Arthanareeswaran, N. Anantharaman, and V. M. Starov, "Performance of modified poly(vinylidene fluoride) membrane for textile wastewater ultrafiltration," *Desalination*, vol. 282, pp. 87–94, 2011.
- [23] P. Gharbani, S. M. Tabatabaie, and A. Mehrizad, "Removal of Congo red from textile wastewater by ozonation," *International Journal of Environmental Science and Technology*, vol. 5, no. 4, pp. 495–500, 2008.
- [24] S. M. Tsui and W. Chu, "Quantum yield study of the photodegradation of hydrophobic dyes in the presence of acetone sensitizer," *Chemosphere*, vol. 44, no. 1, pp. 17–22, 2001.
- [25] J. Wang, Y. Guo, B. Liu et al., "Detection and analysis of reactive oxygen species (ROS) generated by nano-sized  $\text{TiO}_2$  powder under ultrasonic irradiation and application in sonocatalytic degradation of organic dyes," *Ultrasonics Sonochemistry*, vol. 18, no. 1, pp. 177–183, 2011.
- [26] H. Zhu, R. Jiang, L. Xiao et al., "Photocatalytic decolorization and degradation of Congo Red on innovative crosslinked chitosan/nano-CdS composite catalyst under visible light irradiation," *Journal of Hazardous Materials*, vol. 169, no. 1–3, pp. 933–940, 2009.
- [27] R. K. Wahi, W. W. Yu, Y. Liu et al., "Photodegradation of Congo Red catalyzed by nanosized  $\text{TiO}_2$ ," *Journal of Molecular Catalysis A*, vol. 242, no. 1–2, pp. 48–56, 2005.
- [28] A. B. Sifontes, G. Gonzalez, J. L. Ochoa, L. M. Tovar, T. Zoltan, and E. Cañizales, "Chitosan as template for the synthesis of ceria nanoparticles," *Materials Research Bulletin*, vol. 46, no. 11, pp. 1794–1799, 2011.
- [29] D. Valechha, S. Lokhande, M. Klementova, J. Subrt, S. Rayalu, and N. Labhsetwar, "Study of nano-structured ceria for catalytic CO oxidation," *Journal of Materials Chemistry*, vol. 21, no. 11, pp. 3718–3725, 2011.
- [30] E. P. Barrett, L. G. Joyner, and P. P. Halenda, "The determination of pore volume and area distributions in porous substances. I. Computations from nitrogen isotherms," *Journal of the American Chemical Society*, vol. 73, no. 1, pp. 373–380, 1951.
- [31] V. K. Ivanov, A. E. Baranchikov, O. S. Polezhaeva, G. P. Kopitsa, and Y. D. Tretyakov, "Oxygen nonstoichiometry of nanocrystalline ceria," *Russian Journal of Inorganic Chemistry*, vol. 55, no. 3, pp. 325–327, 2010, Translation of Zhurnal Neorganicheskoi Khimii.
- [32] K. Madhusudan Reddy, C. V. Gopal Reddy, and S. V. Manorama, "Preparation, characterization, and spectral studies on nanocrystalline anatase  $\text{TiO}_2$ ," *Journal of Solid State Chemistry*, vol. 158, no. 2, pp. 180–186, 2001.
- [33] S. Damyanova, C. A. Perez, M. Schmal, and J. M. C. Bueno, "Characterization of ceria-coated alumina carrier," *Applied Catalysis A*, vol. 234, no. 1–2, pp. 271–282, 2002.
- [34] A. Bensalem, J. C. Muller, and F. Bozon-Verduraz, "Faraday communications. From bulk  $\text{CeO}_2$  to supported cerium-oxygen clusters: a diffuse reflectance approach," *Journal of the Chemical Society, Faraday Transactions*, vol. 88, no. 1, pp. 153–154, 1992.
- [35] F. Yakuphanoglu and M. Arslan, "The fundamental absorption edge and optical constants of some charge transfer compounds," *Optical Materials*, vol. 27, no. 1, pp. 29–37, 2004.
- [36] A. Corma, P. Atienzar, H. García, and J.-Y. Chane-Ching, "Hierarchically mesostructured doped  $\text{CeO}_2$  with potential for solar-cell use," *Nature Materials*, vol. 3, no. 6, pp. 394–397, 2004.
- [37] R. C. R. Neto and M. Schmal, "Synthesis of  $\text{CeO}_2$  and  $\text{CeZrO}_2$  mixed oxide nanostructured catalysts for the iso-syntheses reaction," *Applied Catalysis A*, vol. 450, pp. 131–142, 2013.
- [38] S. T. Hussain and A. Siddiq, "Iron and chromium doped titanium dioxide nanotubes for the degradation of environmental and industrial pollutants," *International Journal of Environmental Science and Technology*, vol. 8, no. 2, pp. 351–362, 2011.
- [39] S. Samiee and E. K. Goharshadi, "Effects of different precursors on size and optical properties of ceria nanoparticles prepared by microwave-assisted method," *Materials Research Bulletin*, vol. 47, no. 4, pp. 1089–1095, 2012.
- [40] E. K. Goharshadi, S. Samiee, and P. Nancarrow, "Fabrication of cerium oxide nanoparticles: characterization and optical properties," *Journal of Colloid and Interface Science*, vol. 356, no. 2, pp. 473–480, 2011.
- [41] J.-J. Miao, H. Wang, Y.-R. Li, J.-M. Zhu, and J.-J. Zhu, "Ultrasonic-induced synthesis of  $\text{CeO}_2$  nanotubes," *Journal of Crystal Growth*, vol. 281, no. 2–4, pp. 525–529, 2005.
- [42] C. Huang, K. Zhu, M. Qi, Y. Zhuang, and C. Cheng, "Preparation and photocatalytic activity of bicrystal phase  $\text{TiO}_2$  nanotubes containing  $\text{TiO}_2$ -B and anatase," *Journal of Physics and Chemistry of Solids*, vol. 73, no. 6, pp. 757–761, 2012.
- [43] N. T. Nolan, *Sol-Gel Synthesis and Characterisation of Novel Metal Oxide Nanomaterials for Photocatalytic Applications*, Dublin Institute of Technology, 2010.
- [44] S. W. Bennett and A. A. Keller, "Comparative photoactivity of  $\text{CeO}_2$ ,  $\gamma\text{-Fe}_2\text{O}_3$ ,  $\text{TiO}_2$  and  $\text{ZnO}$  in various aqueous systems," *Applied Catalysis B*, vol. 102, no. 3–4, pp. 600–607, 2011.